

Optical read-out and manipulation of
the Néel vector in the metallic
collinear antiferromagnet Mn_2Au

Dissertation

zur Erlangung des Grades

Doktor der Naturwissenschaften (Dr. rer. nat.)

am Fachbereich Physik, Mathematik und Informatik

der Johannes Gutenberg-Universität Mainz

von:

Vladimir Grigorev

geboren in Sankt-Petersburg (USSR)

Mainz, 2021



Vladimir Grigorev

Optical read-out and manipulation of the Néel vector in the metallic collinear antiferromagnet

Mn₂Au

Datum der mündlichen Prüfung: 17. Dezember, 2021

Gutachter: Aus Datenschutzgründen entfernt

/ Removed due to data privacy

Kommission: Aus Datenschutzgründen entfernt

/ Removed due to data privacy

Johannes Gutenberg Universität Mainz

AG Demsar

Institut für Physik

Staudingerweg 7

55128, Mainz

Eidesstattliche Erklärung

Hiermit erkläre ich an Eides statt, dass ich meine Dissertation selbständig und ohne fremde Hilfe verfasst und keine anderen als die von mir angegebenen Quellen und Hilfsmittel zur Erstellung meiner Dissertation verwendet habe. Die Arbeit ist in vorliegender oder ähnlicher Form bei keiner anderen Prüfungsbehörde zur Erlangung eines Doktorgrades eingereicht worden.

Mainz, den

Vladimir Grigorev

Abstract

The rapidly growing field of spintronics benefits from replacing electron charge with the electron spin as an information carrier. Particularly promising is antiferromagnetic spintronics, where the information can be encoded in the staggered magnetisation, the so-called Néel vector. The advantages of employing antiferromagnetic materials, in contrast to ferromagnets, which are widely used for data storage, stem from their unique properties. Firstly, the spin dynamics of antiferromagnets is in the range of THz, while it is limited to GHz in ferromagnets. This, in turn, promises a substantial increase in writing speed. Moreover, the absence of net magnetisation in antiferromagnets makes the information stored in these materials robust against the external magnetic field. Furthermore, antiferromagnets do not produce stray fields, which are the limiting factor for writing density in the case of ferromagnets.

On the other hand, zero net magnetisation makes it challenging to apply the same approaches to control and detect the Néel vector orientation that are commonly used for ferromagnets. Thus, the search for new reliable approaches for manipulating and detecting the Néel vector is the key task of modern research. Optical effects appear especially promising, being also compatible with time-resolved techniques, which would enable studying their dynamics on the intrinsic picosecond timescale.

One of the promising materials for such approach is Mn_2Au , which is a metallic collinear antiferromagnet with the Néel temperature of 1500 K and strong spin-orbit coupling. These properties render Mn_2Au a suitable candidate for applications in spintronics and are of interest for this work.

In this thesis we explore optical methods for detection and manipulation of the Néel vector in Mn_2Au , approaching, also the dynamical study. First of all, we performed a systematic study of reflectivity anisotropy which is found to be susceptible to the orientation of the Néel vector. We demonstrate the magnetic linear dichroism of 0.6 %, which can be used as an efficient tool for read-out of the Néel vector in Mn_2Au .

By direct imaging of the antiferromagnetic domain structure of Mn_2Au , we further demonstrate the possibility of optical switching of the Néel vector. In this case, the application of mechanical strain makes one of the directions of the Néel vector energetically preferable, while ultrashort laser pulses activate the domain wall motion. By irradiation of the sample under external strain, we are able to locally orient the Néel vector along one of the two orthogonal directions, i.e. to record “zero” and “one” states on a single film, thus, realising an efficient and potentially fast memory device.

In addition, using photoemission electron microscopy ([PEEM](#)) imaging we find that uncompensated spins at the surface of the Mn_2Au film generate sizeable x-ray magnetic circular dichroism contrast. This effect allows us to resolve the domains with antiparallel alignment of the Néel, which opens up new opportunities for studying antiferromagnetic domain walls.

Finally, we perform a pilot time-resolved study of Mn_2Au and propose an experiment for the detection of the domain wall motion.

Kurzfassung

Das schnell wachsende Feld der Spintronik profitiert vom Ersetzen der Ladung von Elektronen mit deren Spin als Informationsträger. Besonders vielversprechend ist die antiferromagnetische Spintronik, bei der die Informationen in der gestaffelten Magnetisierung, dem so genannten Néelvektor, gespeichert werden. Verglichen mit bereits etablierten Speicher- methoden, welche auf Ferromagnetismus beruhen, bieten die speziellen Eigenschaften des Antiferromagnetismus diverse Vorteile.

Diese Beginnen bei den im THz-Bereich liegenden Dynamiken beim Antiferromagnetismus, welche, verglichen mit den GHz-Dynamiken von Ferromagneten, eine wesentlich höhere Schreibgeschwindigkeit ermöglichen. Ein weiterer Vorteil liegt in der nicht existenten Gesamtmagnetisierung. Es werden also keine Streufelder erzeugt, diese limitieren beim ferromagnetischen Pendant maßgeblich die Speicherdichte. Umgekehrt sind gespeicherte Daten nun auch weniger anfällig für externe Magnetfelder.

Allerdings verlangt eine fehlende Gesamtmagnetisierung nach innovativen Techniken, die Orientierung des Néelvektors zu detektieren, denn die Lösungen aus ferromagnetischen Anwendungen versagen ohne Gesamtmagnetisierung. Daher steht die Suche nach zuverlässigen Techniken zum Manipulieren und Messen des Néelvektors im Zentrum der gegenwärtigen Forschung. Optische Effekte sind hier besonders vielversprechend, da sie ebenfalls zeitaufgelöste Techniken erlauben. Damit kann man in Dynamiken auf intrinsischer Pikosekunden-Zeitskala eintauchen.

Ein dafür gut geeignetes Material ist Mn_2Au , ein metallisch kollinearer Antiferromagnet

mit einer Néeltemperatur von 1500K und starker Spin-Bahnkopplung. Diese Eigenschaften machen Mn_2Au zu einem möglichen Kandidaten für Anwendungen auf dem Feld der Spintronik und sind daher für diese Doktorarbeit interessant.

In dieser Dissertation beleuchten wir optische Methoden der Detektion und Manipulation des Néelvektors in Mn_2Au . Dies beinhaltet auch Untersuchungen der Dynamiken. Wir haben zunächst eine systematische Studie der Reflexionsanisotropie durchgeführt, welche sensitiv für die Orientierung des Néelvektors ist. Wir zeigen einen magnetischen linearen Dichroismus von 0.6 %, welcher effizient zum Auslesen des Néelvektors in Mn_2Au verwendet werden kann.

Durch direkte Abbildung der antiferromagnetischen Struktur von Mn_2Au demonstrieren wir weiterhin die Möglichkeit des optischen Umschaltens des Néelvektors. In diesem Fall sorgt eine gezielte mechanische Belastung für eine energetisch favorisierte Richtung des Néelvektors, während ultrakurze Laserpulse für eine Aktivierung der Domänengrenzbewegung sorgen. Durch dieses Bestrahlen der Probe unter externer Belastung sind wir in der Lage den Néelvektor lokal entlang einer der beiden orthogonalen Richtungen auszurichten, also “Null” und “Eins” Zustände auf einem Einzelfilm zu speichern. Somit wurde ein effizientes und potentiell schnelles Speichermedium realisiert.

Unter Verwendung von [PEEM](#) können wir beobachten, wie unkompensierte Spins an der Oberfläche des Mn_2Au -Films für deutlichen zirkularen magnetischen Röntgendichroismus Kontrast sorgen. Dieser Effekt ermöglicht eine Betrachtung der Domänen mit antiparalleler Ausrichtung des Néelvektors. Dies stellt eine neue Möglichkeit zur Untersuchung antiferromagnetischer Domänengrenzen dar. Abschließend führen wir eine Pilotstudie an Mn_2Au durch und schlagen ein Experiment zur Detektion der Domänengrenzbewegung vor.

Contents

Eidesstattliche Erklärung	i
Abstract	iii
Kurzfassung	v
Contents	vii
List of acronyms	xi
Introduction	1
1 Studying dynamics in magnetic materials	5
1.1 Time-resolved experiments	6
1.1.1 Pump-probe technique	8
1.1.2 Pump-probe reflectivity/transmission	10
1.1.3 An example of the time-resolved study	15
1.2 Dynamics in magnetic materials	17
1.2.1 Magnetic materials	18
1.2.2 Magnetic domains	20
1.2.3 Ferro- and ferrimagnets	21
1.2.4 All-optical switching of ferro- and ferrimagnets	24

1.2.5	Antiferromagnets	26
1.2.6	Mn ₂ Au thin films	28
2	Magneto-optical effects and read-out of the Néel vector in Mn₂Au	31
2.1	Magneto-optical effects	31
2.1.1	Phenomenological description of the linear magneto-optical effects . .	31
2.1.2	Faraday effect	33
2.1.3	Voigt/Couton-Mouton effect and magnetic linear dichroism	33
2.1.4	Kerr effect	35
2.1.5	Isotropic and anisotropic contributions to the quadratic MO effects in a collinear antiferromagnet	36
2.1.6	What to measure?	38
2.2	Magnetic linear dichroism in Mn ₂ Au	39
2.2.1	Experimental approach	39
2.2.2	AFM domain structure in aligned Mn ₂ Au films	42
2.2.3	Experimental setup for optical dichroism	42
2.2.4	General symmetry considerations	44
2.2.5	Disentangling MLD and structural dichroism	45
2.2.6	Results	46
2.2.7	The possible origins of structural dichroism	48
2.3	Conclusion	50
3	Optical manipulation of the Néel vector in Mn₂Au	53
3.1	XMLD-PEEM	53
3.1.1	Synchrotron radiation	54
3.1.2	Photo Emission Electron Microscopy	56
3.1.3	XMCD and XMLD	58

3.1.4 XMCD contrast in Mn_2Au	60
3.2 Manipulation of a collinear metallic antiferromagnet with femtosecond optical pulses and external strain	64
3.2.1 Strain as a driving force of the Néel vector alignment	65
3.2.2 Experimental approach	66
3.2.3 Results	68
3.2.4 Estimates of laser heating effects	70
3.2.5 Free energy landscape in a strained easy-plane AFM	72
3.2.6 Coherent switching of the AFM domains	74
3.2.7 Thermally activated domain wall motion	75
3.2.8 Conclusion	78
4 Pump-probe study of the metallic collinear AFM Mn_2Au	81
4.1 Time-resolved MLD in Mn_2Au	81
4.2 Towards the dynamics of strain-induced domain wall motion	86
5 Author contributions	93
Bibliography	95
List of Figures	104
Curriculum Vitae	107
Publications list	109

List of acronyms

AOS all-optical switching	MLB magnetic linear birefringence
AMR anisotropic magnetoresistance	MLD magnetic linear dichroism
AFM antiferromagnetic	MO magneto-optical
CDW charge density wave	NIR near infra-red
DFT density functional theory	NSOT Néel spin-orbit torque
DOS density of states	PEM photo-elastic modulator
DW domain wall	PEEM photoemission electron microscopy
EBL electron beam lithography	RKKY Ruderman-Kittel-Kasuya-Yosida
EOM electro-optical modulator	SOC spin-orbit coupling
FM ferromagnetic	XMCD X-ray magnetic circular dichroism
IFE inverse Faraday effect	XMLD X-ray magnetic linear dichroism
IT information technology	XRD X-ray diffraction

Introduction

Starting with the invention of a transistor, information technology (IT) has been rapidly growing in the last 70 years, giving birth to such perspective novel fields as Artificial Intelligence, Machine Learning, Data Science etc. Due to this, a problem of energy consumption arises. The energy consumption of the IT sector is expected to grow up to 51% of the global electricity by 2030.

The rapidly growing IT industry requires new hardware elements to increase the speed and energy efficiency of storing and transmitting data. One of the possible substitutions of conventional semiconductor elements, which have already approached their fundamental limits [1, 2] is offered by spintronics [3]. Spintronics is based on the concept that the information carrier is the electron's spin instead of the electron's charge. This newly emerging field has drawn a lot of attention to magnetic materials, where the individual magnetic moments of electrons act collectively to produce macroscopic fields which can be detected and used for storing data and computing.

While for a general user, ferromagnetic data storage devices like floppy discs were substituted by semiconductor storage devices a long time ago, magnetic tape memory devices are still widely used for long-term memory and big data sets, being the best option in terms of stability and storage density. In ferromagnets, the net magnetisation produced by the ordered spins makes it easy to read and write information with e.g. a magnetic field sensor [4]. On the other hand, the same fact limits ferromagnetic devices in writing density and the speed of writing. To overcome this barrier antiferromagnetic (AFM) materials can

be used [5, 6]. This class of materials has two (or more) ferromagnetic sublattices aligned such to compensate the magnetic moments of each other, hence they exhibit no net magnetisation. Due to this, there is no fundamental limit of the writing density. Moreover, the dynamics of antiferromagnets is expected to be several orders of magnitude faster than in ferromagnets, which can increase the writing speed dramatically.

On the other hand, the absence of the net magnetisation makes it difficult to read the data stored in an AFM with the conventional techniques used in ferromagnetic devices. Thereby, one of the main challenges in antiferromagnetic spintronics is to find an efficient way to detect the magnetic order of the AFMs. While the robustness to the magnetic field is an advantage of AFMs from the point of view of storing data, it becomes a problem in terms of writing the data. Again, one cannot use a magnetic field directly to efficiently manipulate the magnetic order in AFMs as it is used in ferromagnets. Hence, the second main challenge for antiferromagnetic spintronics is to find an efficient method to manipulate the magnetic order of the AFMs.

Another bottleneck of the IT industry is signal conversion. All data processing happens in electrical circuits, where the data is represented by electrical signals. Microprocessors, being an array of transistors, perform logical operations with these electrical signal. Since, big data sets are stored in magnetic memories, there is a need of additional devices to convert magnetic data into electrical signals. Furthermore, after the data processing, the signal should be transmitted to another device and, in most cases, the information signals need to travel across large distances. Clearly, for transferring data, the most efficient tool is light. Thereby, an electrical signal should be converted to an optical pulse, which can travel through a massive net of optical fibers, eventually being converted to an electrical signal again. Since data can not be transmitted faster than the speed of light, the optical data transfer can not be substituted, while the other elements of this system potentially can. Thus, optimizing optical techniques for reading data from the memory devices can exclude

several steps of signal conversion, which, in turn, will reduce the energy consumption of the IT industry.

Thereby, studies of the interaction of light with magnetic materials is an essential part of the modern research. Moreover, the presence of advanced light sources, which can generate ultra-short pulses, makes it possible to study the dynamics of magnetic systems, giving an idea of the potentially achievable writing speeds. In addition, the laser pulses can be as short as a few femtoseconds and can drastically increase the operational speed, breaking the limit of the working frequencies of electrical circuits (GHz).

This thesis is focused on the study of the possible techniques of manipulation and detection of the magnetic order in AFMs with light, which paves a way towards the time-resolved study of the dynamics in AFMs. Of interest for this work is Mn_2Au , which is a very promising material for applications, due to its several unique properties. It is a metallic, collinear antiferromagnet with the Néel temperature of about 1500 K, ensuring its stability at room temperature. The metallicity of this material renders it perspective for compatibility with the conventional devices based on electrical signals. The magnetic field required for the re-orientation of the Néel vector, i.e. the magnetic order parameter, is approximately 30 T [7], which is extremely hard to achieve, thus, preventing undesired erasing of the stored data.

The discussion in this thesis is organised in four chapters as follows:

In chapter 1, I introduce the general idea of time-resolved experiments in order to address the requirements for the dynamical study and introduce the state-of-the-art results on the dynamics of magnetic materials. The chapter finishes with the introduction of the Mn_2Au .

In chapter 2, I give an overview of the magneto-optical effects and present the experimental results of the static optical study of the Mn_2Au thin films, presenting the optical read-out scheme to detect the Néel vector.

In chapter 3, starting with an overview of the experimental techniques for the visualisation of the magnetic order in Mn_2Au , the manipulation of the Néel vector with ultra-short laser

pulses and external strain is presented.

In chapter 4, the results of a first dynamical study of Mn_2Au is presented. The experiments aimed on the time-resolved study of the switching, presented in chapter 3, are proposed.

Studying dynamics in magnetic materials

Why did Fahrenheit come up with Temperature? – To measure it later with equipment.

Mister Maloy

This chapter starts with an introduction to time-resolved spectroscopy. General concept of pump-probe experiments are discussed in order to define the necessary requirements to study the dynamics of any system. The discussion is followed by the basics of the technique from the point of view of the experimental setup. Several basic approaches to increase the signal to noise ratio are explained in order to give the reader an idea of how to build a pump-probe setup. Thus, in the end of the first part, the reader will be acquainted with the specifics of the experimental observation of dynamics in the studied system.

The second part of this chapter is focused on exemplary time-resolved experiments per-

formed on magnetic materials. Starting by briefly introducing the properties of magnetic materials, the chapter discusses the fundamental differences between ferro- ferri- and antiferromagnets in terms of the optical effects, which allow one to study such systems. A short overview of the most relevant studies of the dynamics and switching processes in magnetic materials is followed by the description of Mn_2Au - the material of interest for this thesis. Finally, the chapter is concluded by the discussion of the experimental challenges which appeared while approaching the time-resolved experiment on Mn_2Au .

1.1 TIME-RESOLVED EXPERIMENTS

Over the years, the main idea of experimental physics has been to minimize fluctuations of the system under investigation and get as stable state as possible to measure a certain parameter. By doing so, one can obtain more and more averages leading to more and more accurate result. It is well known that in the past, the best data sets were measured at night, when the tram traffic was off. Indeed, that was the only way to minimize external perturbations and characterize the system in a reproducible way. Such an approach was logically developed from the root of any experiment - observation.

Making sure, the measurement system is sufficiently stable, the next step to improve the accuracy is to integrate the measurement over time: the more time we spend measuring, the more accurate is the result we get.¹

Thanks to the technical progress, even the root of experiment - observation - has changed. Now, no one will believe you without a video of your observation, which, in fact, is not only

¹Here comes the paradox: we can only detect something if it is stable during the time of observation, meaning the system is in some local equilibrium state (steady state). On the other hand, when the experiment is over we are trying to embrace the results using words and the main words are verbs. Intuitively, we are talking of some motion/dynamics/... We can not stop the time, something will happen in any case, that's why even for a static picture we use verbs (time related words) for we do not have any alternative in our language. And this is exactly what we want to know: What/How happens if...? The main word is "happens".

a proof of the observation but also a tool to make a single experiment reproducible. Once we can record the video, we can control the time in our experiment. Moreover, one can increase the frame rate and, thus, slow the time down to observe even faster processes. Such a slow motion video is already a time-resolved experiment. In other words, having a fast enough measurement tool, one can apply this concept to any experimental technique.

The rule of thumb is the following: if the integration time of one measurement event is much smaller than the characteristic time of the process (i.e. the frequency of the measurement tool is much higher than the characteristic frequency of the process), one can perform a time-resolved measurement. For example, to record a simple video the exposure time should be less than 1/24 of a second, to record a guitar string motion, the shutter frequency of the camera should be much higher than the string frequency, and so on.

Unfortunately, just increasing the frequency is not enough to resolve ultra-fast processes such as electron or magnetization dynamics in solids. While pushing the frequency to the limit, one will face the problem of sensitivity. There are two ways to overcome this problem. Firstly, one can increase the measurable signal (i.e. more light on the camera). This is only applicable, however, to study macro objects, which are not affected by the measurement tool too much or not prone to radiation damage. In the case of microscopic processes there is a bottleneck: how not to disturb the system too much with the measurement process.

The second way can be averaging. In order to average a dynamic signal, however, the measured dynamics should be reversible/reproducible, since everything different will be averaged out. The only way to have reversible/reproducible dynamics is to induce the dynamics synchronously with the measurement process.

Finally, when all components are in place, i.e. the induced reoccurring dynamics is synchronized with the measurement event, a pump-probe experiment can be performed.

It is worth noting, that this technique is quasi-static, i.e. it does not record a video of the process, it rather records the dynamics, which is repeatedly observed infinite number

of times. The usual example used to demonstrate the concept of a pump-probe technique is the famous Eadweard Muybridge's experiment, which he performed in order to answer the question: Do all four hooves ever leave the ground at the same time, while the horse is galloping? An array of photo cameras was located along the way of a galloping horse and synchronised with the horse motion making a video of the process. If the horse were a microscopic object as an electron, one would have to use averaging and the resulting data would show the movement of a spherical horse in vacuum. A more appropriate example in our case, though, is a video of a flying helicopter while its propeller seems to be static. This happens due to the so-called stroboscopic effect which occurs when the shutter of a camera is synchronized with the frequency of the propeller.

1.1.1 PUMP-PROBE TECHNIQUE

As mentioned above, the pump-probe technique can be applied to any kind of measurement as long as the event of excitation of the system is perfectly synchronized with the measurement/detection/control event. In an ideal case, the excitation and detection are based the same source. No wonder, this technique is mostly associated with optics. Indeed, optical (laser) pulses are a universal tool for excitation and measurements and, importantly, the same pulse can play both roles. The ways to realize it is to split the pulse train into two with a certain ratio: the first one will excite the system/sample and the second will detect the induced changes in the system after a certain delay. The delay between the pump and the probe pulses is conditioned by the difference of their optical paths. The distance traveled by the optical pulse is controlled by a mechanical stage, often called a delay stage. Thus, scanning the delay between the pump and the probe, real-time dynamics of the system is recorded. A typical setup for pump-probe measurements is schematically depicted in Fig. 1.1. The precision of the time control offered by this implementation can be straightforwardly estimated knowing the speed of light and the accuracy of the delay stage: thus, for the simplest modern stage with the accuracy of $5 \mu\text{m}$, we get 30 fs. Although, as we will discuss

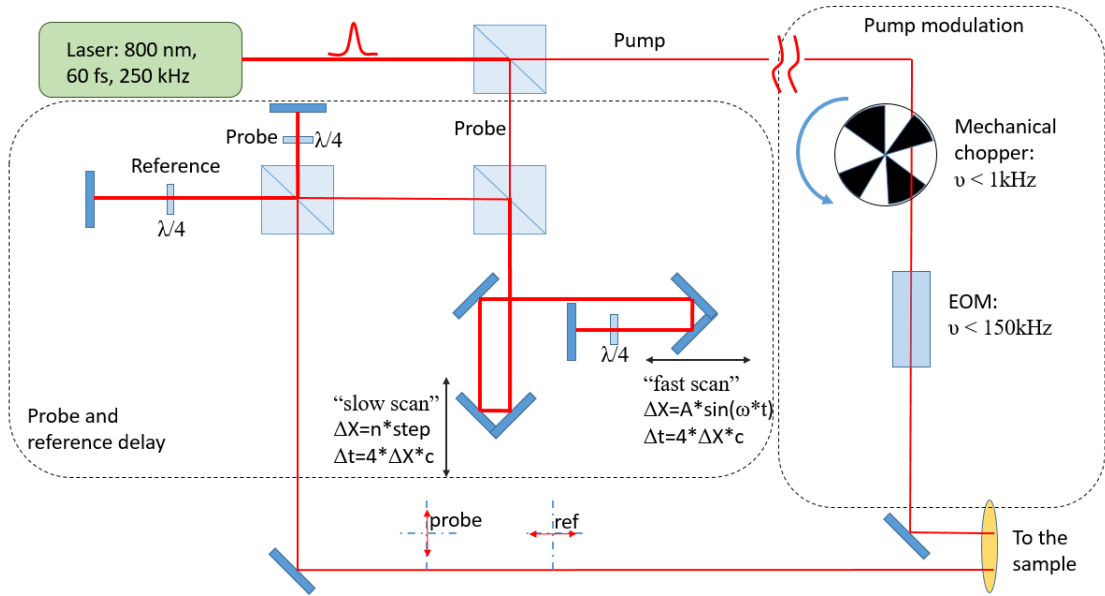


Figure 1.1: Schematic of a pump-probe setup. Pump modulation part consists of two standard options of modulation: a mechanical chopper and electro-optical modulator. Probe delay part consists of both options of delay control: “slow scan” and “fast scan”. Red lines indicate the beam paths, thicker line shows the part where the beam travels twice: back and forth. $\frac{\lambda}{4}$ plate acts as $\frac{\lambda}{2}$ (rotates the polarization of the beam by 90°), when the beam passes twice through it.

later, this is not the only limit of the time precision and definitely not the most crucial one.

Once we have a tool for the delay time control, we can play with the laser pulses in different ways. Everything that can be generated or triggered using light, can be used for time-resolved experiment. Such techniques as X-ray diffraction [8], electron diffraction [9], second harmonic generation [10], photoemission [11] etc, already have a prefix “TR” for time-resolved. Since this thesis focuses only on general optical experiments, we will describe an all-optical experiment in greater detail, while for an overview of the other time-resolved techniques the reader is referred to the aforementioned comprehensive reviews.

Another important aspect to think about for the experiments is the time resolution,

which should be defined by the processes that are going to be measured. In astronomy, for example, the characteristic time-scale of the observable processes is in the range from day/month/year to the lifetime of the universe. Hence, there is no need for fast measurement devices, but there is barely a possibility to average the signal over many cycles. That is why the main focus there is sensitivity. In the case of condensed matter physics, the typical time constants are from several fs, as in the case of the dynamics of electronic system, up to ns for magnetic processes [12]. It is one further argument why the discussed technique is intimately related with lasers, which can generate short enough and reproducible pulses. Modern laser technology provides experimentalists with pulse duration down to 50 attoseconds [13], which is sufficient to study processes happening in a nucleus, while for our purposes even 60-100 fs pulses suffice. And, luckily for the solid state experimentalists, there is a huge variety of fs laser system on the market.

1.1.2 PUMP-PROBE REFLECTIVITY/TRANSMISSION

Here, we continue with the description of the simplest pump-probe setup. However, there is no limits for possible modifications aimed on the performance, and some of them will be presented here. Everything starts in the heart of the lab - a fs laser system. The laser generates light pulses with a repetition rate of 250 kHz (in our case). The pulse travels through space towards the setup, where it splits into two pulses (see Fig. 1.1). One unnamed laser pulse and a beam splitter give birth to two pulses, naming them a pump and a probe. These two take different paths with the same distance to meet each other again on/in the sample. The pump travels directly to the sample, just making a detour for the sake of path-equality, while the probe goes through a delay stage and arrives at the sample at the same time as the pump \pm the time window of interest. The probe pulse reflects off/transmits through the sample to be caught by a photodiode, an electrical signal from which is recorded into the memory of a measurement PC. The same happens for thousands/millions/billions pulses. Then the delay stage moves, and the next time point is recorded. Seems to be

working, but it is not enough.

First of all, the photodiode will react to any light, so the noise will be high. In order to filter out all external noise, one can read values from the detector just when they are caused by the pump. Here, we come to the first/main modification - Lock-in detection scheme. For that to work, the pump pulses should be modulated. The simplest tool is a mechanical chopper with a working modulation frequency up to 1 kHz. More advanced option is an electro-optical modulator (EOM), which can work even at half the frequency of the laser repetition rate. In this thesis we will regard the processes happening inside the lock-in as electronic magic, of which, however, the interested reader can learn in e.g. Ref. [14]. Important for us is that as a result, we obtain differential values, i.e. pump-on minus pump-off, or in Fourier space, the lock-in filters out the signal at all frequencies other than that of the pump modulation. However, the highest signal at the pump modulation frequency is the pump itself, hence it is very important to prevent any scattered pump light on the photo-diode.

Since laser is based on quantum effects, even perfectly aligned system has pulse to pulse deviations, which will again increase the noise. The way around it, is to chunk a part of the probe and name it a reference pulse, which will be reflected/transmitted at the sample where there is no pump either in time or in space. Afterwards the probe and the reference will compete against each other in a balance detector (see Fig. 1.2). The recorded signal will not be affected by the long time sample and light source instabilities. One option for reflectivity experiment is to split the probe and the reference by polarization and time. By doing so, one can measure the same point of the sample. Before the balanced detector the beam splits again by a polarizing beam splitter. Such technique, however, should be used very carefully with magnetic materials, since the pump-induced changes of the light polarization will affect the signal.

Before we discussed only a scheme when we go from one time point to another, staying

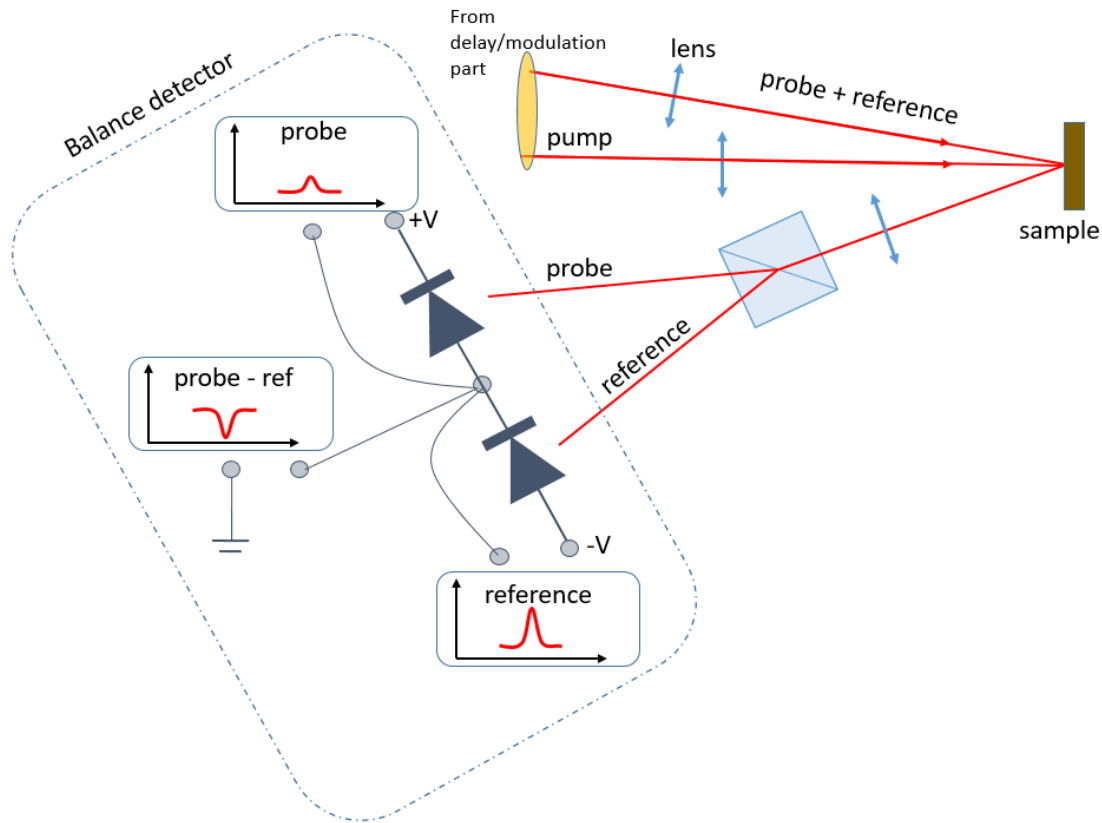


Figure 1.2: Detection scheme of a pump-probe setup using a balance detector and a Wollaston prism as a beam splitter. Reference pulse is separated in time from the probe by the time grater than the measured time window, to ensure that it hits the sample before the pump pulse.

there long enough to get a desirable signal to noise ratio. In the following we will call this scheme as a “slow scan”. Since, the time of one experiment can easily increase to several hours, even astronomic processes and climate change can affect the signal, and definitely system drifts caused by e.g. humidity change. Semantically, the solution will be a “fast scan”. The difference of these two concepts is visualized in Fig. 1.3 comparing the timing of “slow scan” and “fast scan” experiments, which suppresses such long-term drifts.

The concept is easy to understand while being in the Fourier space: by modulating/sweeping the control parameter (time delay) with a certain frequency, all noise at lower frequencies

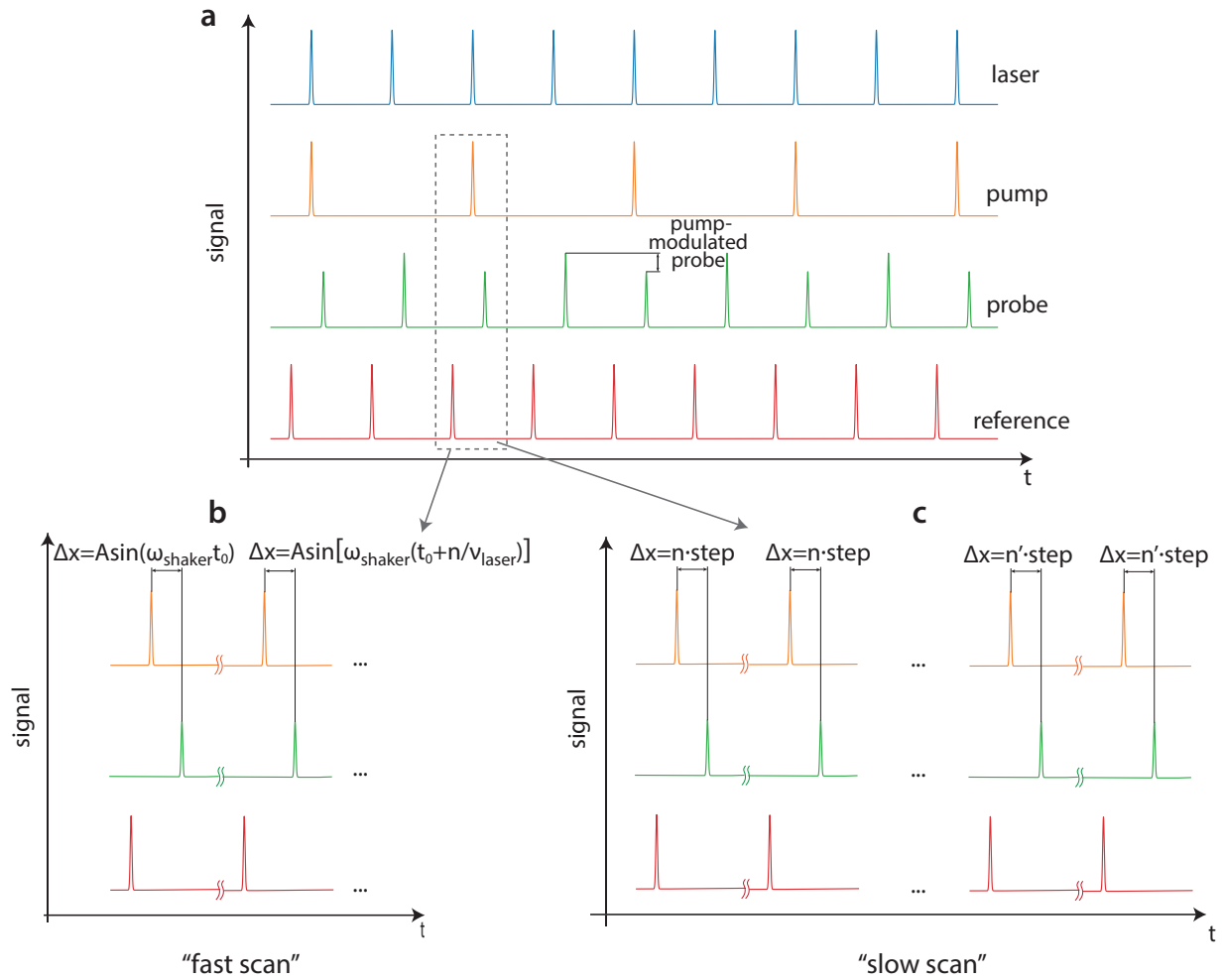


Figure 1.3: (a) General timeline of the light pulses used in the pump-probe experiment. Here the pump is modulated at $\frac{1}{2}$ of the repetition rate to block every second pump pulse. (b) Delay of the probe pulse in "fast scan". (c) Delay of the probe pulse in "slow scan". n indicates the measurement step and $\Delta x = \Delta t \times c$.

will be averaged out. Technically, we need to scan the time delay fast enough to average out low frequency noise, and measure one time delay point by one laser pulse. To do this another device called “shaker” is added to the setup. It shakes the retro-reflector at the frequency up to 50 Hz (not the best value). In addition to the noise reduction, there is another advantage of this method - if the signal is large enough, it can be observed in real time, which is extremely useful for setup optimization and especially when working with new samples. Moreover, during a “fast scan”, an experimentalist can interrupt the measurement at any time without losing any part of the time-delay window. Surely, this approach is also not free of disadvantages: a small time-delay window limited by the shaker amplitude, the need for advanced software being able to synchronize all the systems, just to name a few.

In conclusion, in pursuit of a successful time-resolved experiment, one should be able to answer two important questions:

- The first question is “*what to measure?*”, i.e. what kind of an optical effect can be employed to detect the state of the studied system, how big it is and if it is feasible to observe it in the given material. In order to answer this question one often needs first to perform static measurements.
- The second question is “*how to reproducibly trigger the dynamics with a light pulse?*” As discussed above, the system should recover to the initial state after every excitation. In the case of thermal effects, for example, one needs to make sure that the sample cools down faster than the period between two successive pump pulses, while in the case of magnetic materials it is not so trivial. One needs to find a way to bring the system back to the initial state before every measurement iteration, and this is the main challenge for the time-resolved study of antiferromagnets, as we will see in the following.

1.1.3 AN EXAMPLE OF THE TIME-RESOLVED STUDY

In order to give the reader a feeling of the capabilities of a pump-probe technique, the results of a time-resolved study of BaNi_2As_2 is briefly presented [15]. Without introducing the material, the reflectivity pump-probe data is discussed in order to illustrate how complicated the signal can be and how to disentangle different contributions to the signal in order to understand the dynamical processes measured by the pump-probe technique. The pump-probe transient reflectivity trace recorded at 10 K is shown in Fig. 1.4.

The raw data shows a complicated response which can be decomposed into several contributions as discussed in the following. In the general case, any contribution to the transient signal can be classified as a coherent (oscillating) and incoherent response. The incoherent response represents the integral response of the system (e.g. the decay of photoexcited carrier density). In a simple case, the intense laser pulse rapidly heats up the electronic subsystem, which then thermalizes with the lattice on a certain time-scale. Furthermore, every incoherent response can be attributed to the thermalization of one or another subsystem: electron gas, lattice, phonons, spin system/magnetisation, etc. By comparing the time-scales of the processes and performing systematic temperature and fluency dependent studies, one can distinguish the responses of these different systems. In the first approximation, one can say that the light interacts with the electrons only, heating the subsystem up on the time-scales of the pump pulse duration. Such process can be clearly seen in the presented data in Fig. 1.4 (incoherent): After ultra-fast excitation, the electronic system cools down within a few picoseconds due to the electron-phonon coupling.

The second contribution to the incoherent part of the signal is much slower with the rise time of tens of picoseconds. This could be attributed to the increase of the lattice temperature and the processes linked to the thermalization of the lattice.

After decomposing the incoherent part of the signal, one can analyse the coherent part (green in Fig. 1.4 coherent). If the decomposition is done correctly, only pure oscillatory

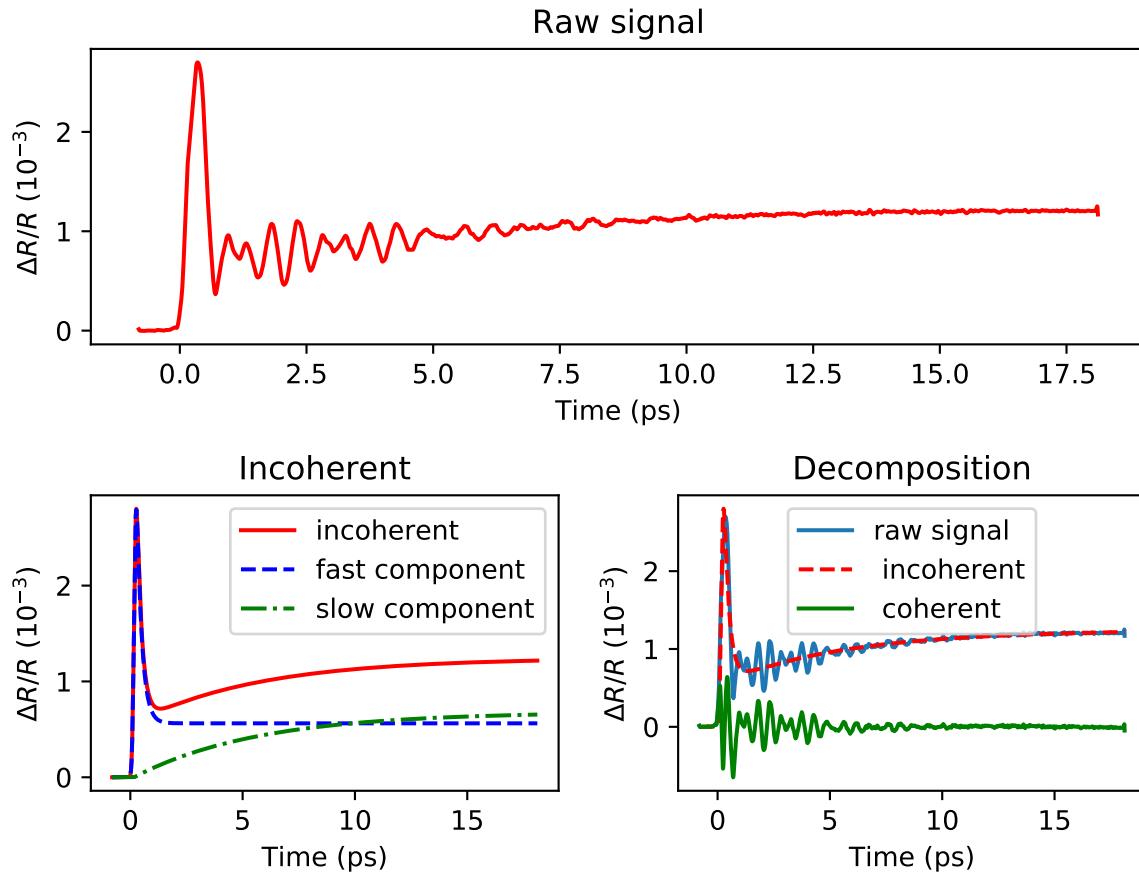


Figure 1.4: Example of the transient reflectivity measured on BaNi_2As_2 at 10 K. Top panel shows a raw signal. Bottom left is the incoherent part of the signal consisting of the “fast” and the “slow” components obtained by fitting the data with double exponential decay function. Bottom right shows a decomposition of the signal into coherent (oscillating) and incoherent components.

signal should remain, representing the collective motion of the system, e.g $q=0$ Raman active optical phonons or charge density wave (CDW) amplitude modes. Here, it is worth to highlight that the detected oscillatory part represents the collective and synchronous processes in the studied system which take place everywhere across the sample covered by the probe light spot. This is the result of the stroboscopic approach of the pump-probe experiment.

In order to attribute the measured dynamics to the correct process in the system, the experimentalist should refer to the question “*Why is the dynamics reproducible?*” The incoherent part of the signal is often responsible for thermal effects. Thermal effects should be insensitive to the pump pulse polarization and any other geometrical parameter. In the case of coherent (oscillatory) dynamics the situation is simpler, the main question is why the light induces the dynamics and what excitations give such contributions to the signal. In the specific case of BaNi_2As_2 , the oscillatory part of the signal is governed by amplitude modes of the charge density wave, as we have shown in [15].

1.2 DYNAMICS IN MAGNETIC MATERIALS

As discussed in the introduction, spintronics is based on the concept that the information carrier is the electron’s spin instead of the electron’s charge. For a spintronic device one needs to have a correlated spin structure, i.e. ordered magnetic material. In the framework of this thesis we limit the discussion of the wide range of magnetic materials to only magnetic crystals, which can be divided in three groups: ferromagnets, ferrimagnets and antiferromagnets. Since this thesis is mostly focused on experimental results, only a brief account for the theory of magnetism is given, necessary to understand the effects which can be used for the experimental study of magnetic materials.

1.2.1 MAGNETIC MATERIALS

The discussion in this section is based on Ref. [12], to which the interested reader is referred for a comprehensive consideration.

In the general case, magnetic crystals represent a class of materials formed by magnetic atoms, i.e. having non-zero magnetic moment. The source of a magnetic moment is an electron, more precisely its intrinsic magnetic moment (spin), μ^{spin} , and orbital magnetic moment, μ^{orb} . Following the Pauli principle and the Hund's rules, one can establish if there is an uncompensated magnetic moment in an atom comprising many electrons. For example, Fe, Co and Ni have not completely filled 3d-sub-shell. In this case, uncompensated spin and orbital magnetic moments of the electrons form a non-zero total magnetic moment of the atom, which can be expressed as follows:

$$\mu^{total} = \mu^{spin} + \mu^{orb} = -\frac{\mu_B}{h}(L + 2S). \quad (1.1)$$

When magnetic atoms form a crystal structure, their magnetic moments interact with each other and can align along one direction, resulting in spontaneous magnetisation. The origin and the strength of this interaction determines the temperature when the spontaneous magnetisation/magnetic order can be observed. Taking into account the dipolar interaction of magnetic dipoles μ_1 and μ_2 separated by a distance r , one can estimate the energy of this interaction as follows:

$$E = \frac{\mu_0}{4\pi r^3}(\mu_1\mu_2 - \frac{3}{r^3}(\mu_1 r)(\mu_2 r)). \quad (1.2)$$

A quick estimation of the energy for two magnetic dipoles of μ_B separated by 1 Å gives the resulting energy of about 10^{-23} J, which corresponds temperature of 1 K. Thus, the dipole interaction is not enough to explain the magnetic order which can be observed up to, e.g., 1388 K in Co [12].

Another mechanism of forming magnetic order in a crystal is the Heisenberg exchange interaction. The quantum mechanical derivation of this model can be wrapped up into the

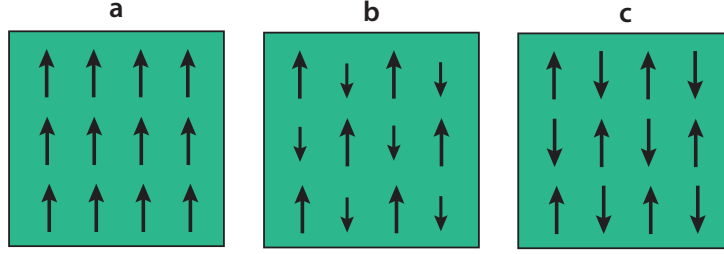


Figure 1.5: Spin configurations of crystalline (a) ferromagnetic ($J > 0$), (b) ferrimagnetic ($J_{n,n+2} > 0, J_{n,n+1} < 0$), (c) antiferromagnetic ($J < 0$) materials.

Hamiltonian of the Heisenberg model:

$$H = - \sum J_{ij} S_i S_j, \quad (1.3)$$

where J_{ij} is the exchange constants between two neighboring spins. The exchange constant is defined by the difference of the energy for singlet and triplet states, i.e. parallel or antiparallel alignment of the spins. The strength of the exchange interaction defines the critical temperature $T_c = \frac{J}{k_B}$ below which the spontaneous magnetisation occurs. The presented Heisenberg model takes into account only nearest neighbor interactions, i.e. the direct exchange, but in some systems the indirect interaction can take place giving rise to additional exchange terms like Ruderman-Kittel-Kasuya-Yosida (RKKY) [12, 16] or Dzyaloshinskii-Moriya [17, 18] interactions, which are described elsewhere.

For further discussion, the value and the sign of the exchange constant play a role. The sign of the exchange constant defines the alignment of the spins, giving rise to the different classes of magnetic crystals: ferromagnets - equal magnetic moments aligned parallel $J > 0, \mu_1 = \mu_2 = \dots = \mu_n$; ferrimagnets - two different types of magnetic moments aligned antiparallel $J_{n,n+2} > 0, J_{n,n+1} < 0, \mu_1 = \mu_3 = \dots = \mu_n \neq \mu_2 = \mu_4 = \dots = \mu_{n+1}$ and antiferromagnets, with equal magnetic moment aligned antiparallel $J < 0, \mu_1 = \mu_2 = \dots = \mu_n$, as illustrated in Fig. 1.5.

1.2.2 MAGNETIC DOMAINS

Before the discussion of experimental studies of the magnetic crystals it is worth to explain the origin of magnetic domains. First, we start with the concept of anisotropy. In a crystal, non-symmetric electron orbitals tend to align in a certain direction, for example, along a crystallographic axis. Due to the spin-orbit coupling (SOC), the energy of the system has a local minimum when the magnetic moments of the atoms align along one axis called the easy axis. In the general case of uniaxial anisotropy, when there is only one easy axis, the anisotropy energy can be written as:

$$E_{anis} = K_1 \sin^2 \Theta + K_2 \sin^4 \Theta + K_3 \sin^6 \Theta + \dots \quad (1.4)$$

where K_i ($i = 1, 2, 3, \dots$) are the anisotropy constants and Θ is the angle between the volume magnetisation M and the anisotropy axis. From the point of view of the magnetisation, any anisotropy axis is even, i.e. the two magnetic orientations, pointing to opposite directions, are energetically equal: magnetic moments aligned at 0° and 180° with respect to the easy axis. Thus, for any magnetic crystal there are at least two options of the equilibrium magnetisation orientation. This fact made magnetic materials widely used as data storage elements.

On the other hand, the presence of energetically equal magnetisation orientations leads to the formation of magnetic domains. Magnetic domains stand for the spatial regions of the crystal within which the magnetic moments point in the same direction. Any concept of the manipulation of magnetic order (writing) in magnetic crystals, in a nutshell, is simply the induction of an external anisotropy, which can break the symmetry of the magnetisation. The easiest way to add anisotropy for the magnetic moments of a crystal is to apply a magnetic field, which perfectly works for ferromagnets, although sometimes can cost a lot of energy. Alternatively, by applying mechanical strain, one can deform the crystalline structure in order to induce additional anisotropy. Moreover, in some systems, electrical currents can impose additional anisotropy and, thus, manipulate the magnetic order [19, 20].

While in the case of ferromagnets, the domain formation can be easily explained by minimisation of the energy due to the macroscopic interaction between the neighboring domains, for antiferromagnetic materials such explanation can be complicated. Here, we refer to a more general explanation which follows from the Curie principle: “the symmetries of the causes are to be found in the effects” [21]. In other words, the symmetry of a crystal should change during the phase transition keeping the symmetry elements common with the symmetry elements of the cause of the phase transition. Since the cause of a magnetic phase transition is temperature change, which is a scalar parameter, the total symmetry of the system should not change. On the other hand, magnetically ordered materials break the symmetry, so that the only way to fulfil the Curie principle globally is to split up the volume of the system into differently aligned magnetic domains, thus keeping the total system magnetically neutral.

Furthermore, the existence of magnetic domains enables keeping the magnetic structure stable for a long time, which makes it possible to use magnetic materials in memory devices. But from the experimental point of view one should find the detection configuration to detect only a single domain. Otherwise, while measuring a multidomain state, any signal related to the magnetic order will be averaged out.

1.2.3 FERRO- AND FERRIMAGNETS

As it was discussed in the first section, in order to perform a dynamic study of a system, an experimentalist should first answer two questions: “*What to measure?*”, “*How to make the dynamics reversible?*”. In the following discussion we will tackle these two questions, starting from the first.

In the case of ferro- and ferrimagnets, the magnetization of a crystal can be easily detected with optics, using magneto optical-effects. While an extensive overview of the magneto-optical (MO) effects will be presented in chapter 2, here, we briefly mention the magneto-optical Kerr and Faraday effects which are often used for probing ferro- and ferrimagnets.

The former is a surface sensitive optical effect, which is widely employed for studying non-transparent magnetic materials, e.g. metals. The Faraday effect is volume sensitive and is used for studying transparent materials, e.g. insulators. The difference is defined by the geometry of observation: measuring the reflected or transmitted light correspondingly. Here, interaction of light with magnetic materials leads to changes in the polarization of light. Fortunately, it is easy to detect the change of the light polarization using a polarization beam splitter (Wollaston prism) and a balance detector. Such a detection scheme is also well integrated within pump-probe experiments especially to study ferromagnets, where large signal can be expected.

Making the dynamics reversible in the case of ferro- and ferrimagnets is also easily achieved by external magnetic fields. In this case, the presence of an external magnetic field will align the magnetisation of the crystal in a certain direction. So even if the magnetisation is altered by the pump pulse the system will return to the initial state on the timescale between two successive pump pulses. The magnetic field required to magnetize a ferromagnet is normally easy to achieve with a small electromagnet. Thus, the second condition is fulfilled. Moreover, by magnetising a ferromagnet with a sufficiently large magnetic field ensures that a single domain state is measured.

The pioneering work of a dynamical study of ferromagnets was done in 1996 by Beaupaire et al. [22]. There, a strong pump pulse was used to demagnetise the system (Ni film) and the time-dependent evolution of the magnetisation was detected via the Kerr effect. As a result of the experiment, it was shown that the demagnetisation of the ferromagnet takes place on the 60 fs time-scale. The main value of this discovery is that the magnetic properties of a crystal can be drastically changed on the ultra-short time-scale. While exact mechanism is still a matter of intense scientific discussion, we discuss here a simple phenomenological model. The three temperature model was suggested in order to explain this effect. It assumes that an intense optical pulse heats up free electrons, which then ther-

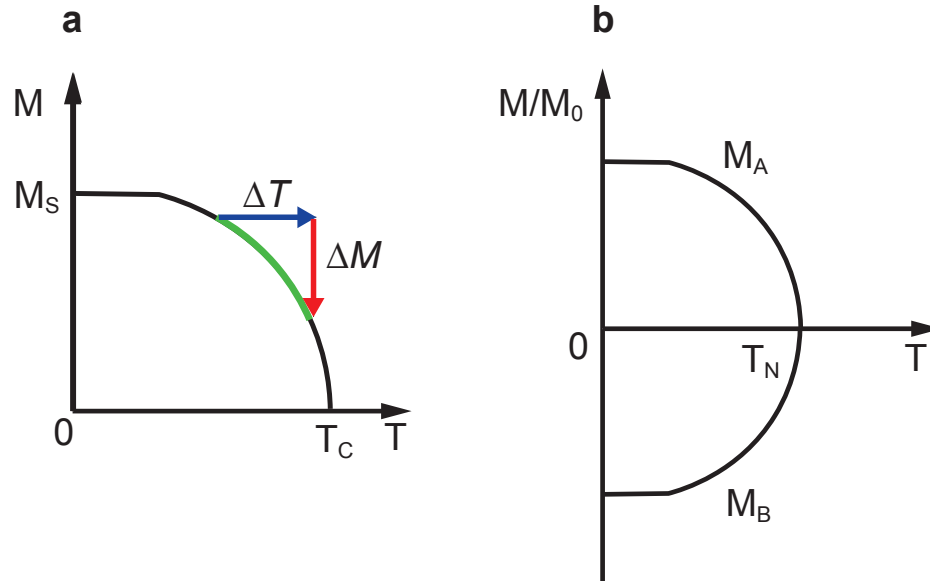


Figure 1.6: Spontaneous magnetisation as a function of temperature (a) typical for a ferromagnetic material with the Curie temperature T_C and (b) of the two sub-lattices M_A and M_B of an antiferromagnet with the Néel temperature T_N .

malize giving energy to the lattice and the spin system reducing the magnetisation of the system as shown in Fig. 1.6. The recovery of the ferromagnetic (FM) order takes place on the subnanosecond time-scale. In the next decade, similar experiments were done on a wide range of ferromagnets [23, 24, 25, 26, 27].

Furthermore, it turned out that an intense optical pulse can also induce a coherent spin (magnetisation) precession in ferromagnets, which can be detected with the Kerr effect [28]. Other studies also demonstrate, that it is possible to use an optical pulse to induce an additional anisotropy and cant the magnetisation of the crystal away of the equilibrium state. As a result the magnetisation starts to precess around this effective anisotropy field [29]. Besides the applicability to study spin dynamics, this effect can be used for characterising coupled system, such as exchange bias systems, consisting of antiferromagnet/ferromagnet multilayers [30].

1.2.4 ALL-OPTICAL SWITCHING OF FERRO- AND FERRIMAGNETS

Another fascinating topic of the interaction of light with magnetic materials is the reverse switching of magnetisation with ultra-short light pulses. By using sub-picosecond light pulses, the writing speed can be increased up to the fundamental limit of the magnetisation switching. All-optical switching was demonstrated for several ferrimagnetic dielectrics [31] and ferrimagnetic metals [32, 33]. In these cases, ultra-short laser pulses were shown to reproducibly switch magnetisation on the time-scale of a few tens of picoseconds. While both the helicity dependent and independent switching were observed, the underlying mechanism of this effect is still not understood, although it is accepted that laser heating plays a significant role in both scenarios.

The first proposed mechanism suggested for reversible spin switching is an inverse Faraday effect (IFE). Indeed, if a magnetic field (magnetisation) changes the polarization of light, the light should also induce some torque on the source of the magnetic field. Said differently, circularly polarized light interacting with electrons inside the sample induces circular currents which, in turn, produce an effective magnetic fields [34]:

$$\vec{M} = \frac{ie\omega_p^2}{16\pi\omega^3 mc} [\vec{E} \times \vec{E}^*], \quad (1.5)$$

where ω_p is the plasma frequency and ω is the light frequency, \vec{M} is a effective magnetic field generated by light and \vec{E} is the electric field of light. The induced magnetic field is parallel to \vec{k} vector of light and its direction is defined by the helicity of the circular polarization. Thus, this method of the magnetisation switching is compatible only with materials with out-of-plane magnetic anisotropy, i.e magnetisation pointing normal to the surface. On the other hand, the resulting magnetic field is expected to be rather small, not strong enough to align the magnetisation of the material at temperatures far below the Curie temperature, where the magnetic state is stable. Moreover, one should also consider the time of the interaction between the spin system and the magnetic field generated by laser pulse, which is limited by the laser pulse duration (100 fs). It is evident that this time is significantly smaller than

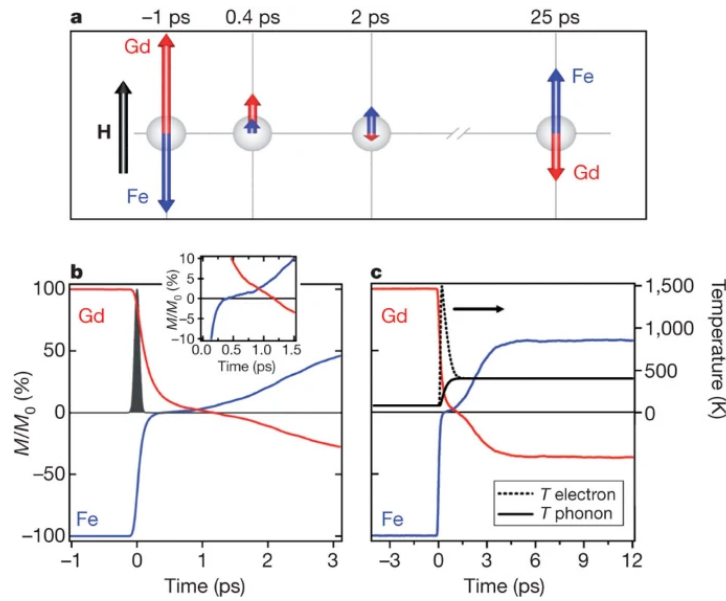


Figure 1.7: Element specific demagnetisation dynamics in $\text{Gd}_{25}\text{Fe}_{65.6}\text{Co}_{9.4}$ illustrating the proposed mechanism of all-optical switching. The dynamics for the first 3 ps (b) and the first 12 ps (c) after laser excitation, showing that the demagnetization of the Fe is much faster than that of the Gd (inset in (b) shows zoomed in region of the switching). For a time of approximately 0.5 ps, a parallel alignment of magnetisation of the sublattices is observed as indicated in (a). Taken from Ref. [33] with permission.

the time needed for the magnetisation reorientation of ferri- or ferromagnets, defined by the fundamental frequency of ferromagnetic resonance (GHz) [12].

On the other hand, rapid thermal demagnetisation of the material can lead to the situation where the light-induced field is applied when the system is already close to the Curie temperature, or is already demagnetised. However, the absence of the helicity dependent switching in most ferromagnets implies a more complicated mechanism.

An alternative mechanism proposed for all-optical switching of ferrimagnets [33] suggests the appearance of a short-term transient ferromagnetic state caused by the difference of the demagnetisation times for the two sublattices. Indeed, the recent element specific pump-

probe experiment shows slightly different demagnetisation times for Fe and Gd magnetic sublattices in $\text{Gd}_{25}\text{Fe}_{65.6}\text{Co}_{9.4}$ [33]. There, sublattice 1 demagnetises faster than sublattice 2 and for a short time couples to sublattice 2 ferromagnetically. Then, sublattice 2 demagnetises and recovers to the antiferromagnetically coupled state, which results in a switched state after cooling. The proposed mechanism is depicted in Fig. 1.7.

In this scenario, the magnetisation of the ferrimagnet switches after every laser pulse, which allows measuring the dynamics of the switching process. By separating the even and odd probe pulses from each other, the even and odd measured data will represent the switching dynamics [35].

For a long time, all-optical switching (AOS) was observed only in ferrimagnets or synthetic ferrimagnetic multilayers [36]. However the recent discovery of all-optical switching in ferromagnets, drew a lot of attention to the AOS mechanisms. It was shown that the helicity dependent AOS is possible in ferromagnet/heavy metal multilayers [37]. Varying the combination of materials and the geometry, AOS with only four pairs of pulses was realized [38].

While unambiguous understanding of the underlying switching mechanism is still elusive, different scenarios are discussed, mainly trying to identify the origin of the helicity-driven torque [39]. The only piece of this puzzle which definitely works is the thermal activation. When a magnetic material rapidly heats up and demagnetises, even a small magnetic torque generated by a laser pulse can be sufficient to initiate the switching.

1.2.5 ANTIFERROMAGNETS

Antiferromagnets (AFMs) is a class of materials which have two (or more) ferromagnetically coupled spin sublattices aligned in a way to compensate the magnetisation of each other. AFMs having two equivalent spin sublattices aligned antiparallel are called collinear. Figure 1.6 (b) shows the net magnetization of the two sublattices, designated “A” and “B”, decreasing as the temperature approaches the Néel temperature above which the antifer-

romagnetic order is destroyed. The order parameter is the so-called Néel vector which, in general, represents the magnetization vector of one of the sublattices. Besides collinear AFMs, there is a large variety of non-collinear AFMs including such an exotic class of frustrated AFMs. In this thesis the discussion is limited to collinear AFMs. Moreover, only a few examples of the non-collinear AFMs are concerned, where it was possible to measure their dynamics.

AFM materials have drawn significant attention of the scientific community in the last decade due to their potential application in data storage and spintronic devices [3, 5, 6, 40, 41]. The conventional ferromagnetic memory devices have reached their fundamental limits in the recording speed, defined by the frequency of the ferromagnetic resonance (GHz), while the AFM resonance is expected to be in the THz range [12], thus, promising a substantial increase in the data recording speed. Moreover, the absence of the net magnetisation makes such materials robust against external magnetic fields as well as allows for a significant increase of the recorded data density. On the other hand, the same fact makes it extremely challenging to manipulate and detect/read-out the Néel vector which encodes the state of an AFM.

Thereby, the main challenge in spintronics community is to find a way to efficiently manipulate and detect the Néel vector. It is worth to highlight the double-side problem: it is hard to study the switching process, while there are limited ways of detection, and vice versa, how can one test the detection scheme when it is hard to manipulate the order parameter. Luckily, the situation is not so bad. In the presence of high enough magnetic field (spin-flop field) the two orientations of the Néel vector become energetically unequal and the spins orient perpendicular to the applied magnetic field. For example in Mn_2Au , the AFM of interest in this thesis, the spin-flop field is around 30 T, which can be achieved only in pulsed regime at a high magnetic field facility. This, in turn, hampers the use of such fields as a manipulating tool in combination with a table-top detection technique.

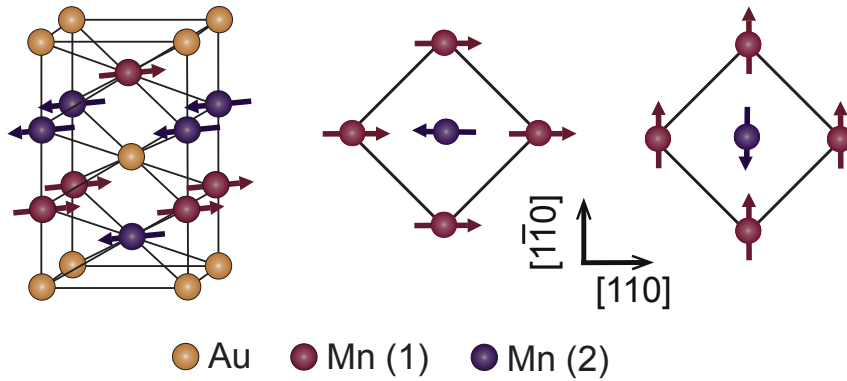


Figure 1.8: The structure of Mn_2Au showing the spin orientations in adjacent layers. The spin orientations in adjacent layers are presented by arrows, with the Néel vector pointing along the easy $[110]$ or $[\bar{1}\bar{1}0]$ directions.

Clearly, the absence of an accessible way to reproducibly align the Néel vector makes it challenging to measure the order parameter dynamics as in ferro-/ferrimagnets. Even if we focus the probe beam onto one domain, we will never know in which direction it will be oriented before each excitation. On the other hand, if one can measure some optical property of the crystal which is proportional to the order parameter and is independent of the exact direction of the Néel vector, the order parameter dynamics can be measured.

Coherent spin dynamics can be detected by the MO effects as long as it can be induced. It was detected in a collinear AFM NiO [42], by inducing the dynamics through the IFE and the inverse Cotton-Mouton effect. The latter is a similar effect to the IFE but in the geometry of an AFM. Measurements in the transmission geometry enabled accumulation of the E-field rotation in the entire depth of the sample. In addition, it was reported that a single domain state was probed during the measurement.

1.2.6 Mn_2Au THIN FILMS

The AFM Mn_2Au which is of interest not only for this thesis but also for applications in spintronics provides, several advantages. It is a good metallic conductor and does not

contain toxic components as compared to its competitor CuMnAs [19]. Furthermore, its magnetic ordering temperature is well above 1000 K [43], providing the necessary thermal stability for potential applications. Finally, its specific symmetry and strong SOC enables also manipulation of the Néel vector with current pulses through Néel spin-orbit torque (NSOT) [20, 44].

Mn₂Au has a body centered tetragonal crystal structure, whose unit cell is depicted in Fig. 1.8. It is an easy plane AFM, with a strong out-of-plane and a weak in-plane magnetic anisotropy. The spin orientations in adjacent layers are presented by arrows, with the Néel vector pointing along the easy [110] or [1 $\bar{1}$ 0] directions [43, 45, 46].

The *c*-axis (001) oriented epitaxial Mn₂Au thin films used in this thesis were grown on r-cut (1 $\bar{1}$ 02) Al₂O₃ substrate, with the lateral size of 10×10 mm² and thickness of 530 μm by the radio-frequency magnetron sputtering at 600 °C, following the recipes described elsewhere, see Ref. [46] for details. To ensure epitaxial growth a (001) Ta buffer layer was used. To protect the surface, a 2 nm Al layer was also deposited on Mn₂Au, forming an aluminum-oxide capping layer. Mn₂Au grows epitaxially with [110] and [1 $\bar{1}$ 0] axes parallel to the substrate edges, which are along the [010]_s and [211]_s directions of r-cut Al₂O₃.

Important for the following discussion is that the *c*-axis of the Mn₂Au films grown on (1 $\bar{1}$ 02) Al₂O₃ is tilted with respect to the surface normal by about 2-3° [44, 47] (the tilt shows small variation from sample to sample). The *c*-axis of the film tilts towards the [010]_s axis of the substrate.

As previously demonstrated [7, 20, 48, 49], the application of a magnetic field, exceeding 30-50 T results in the Néel vector being aligned along one of the easy axes, perpendicular to the direction of the applied field [7]. Note, however, that such a “polarization” of the film may be incomplete, i.e. there is still a small fraction of orthogonally polarized domains [7, 20, 49].

Magneto-optical effects and read-out of the Néel vector in Mn_2Au

This chapter includes an overview of the magneto-optical effects studied in this thesis. Basic relations of the light-matter interaction are described. The influence of the magnetic order on the optical properties of solids is phenomenologically explained. Built on this background is the discussion of the first experimental result of this thesis, namely the observation of magnetic linear dichroism in Mn_2Au .

2.1 MAGNETO-OPTICAL EFFECTS

In this section, we follow the discussion in Refs. [50, 51].

2.1.1 PHENOMENOLOGICAL DESCRIPTION OF THE LINEAR MAGNETO-OPTICAL EFFECTS

Interaction of light with crystals can be described by the permittivity ϵ_{ik} and permeability μ_{ik} tensors, which define the relation between the magnetic and electric field vectors

$$\vec{E}_i = \epsilon_{ik}(\omega)\vec{D}_k; \vec{B}_i = \mu_{ik}(\omega)\vec{H}_k \quad (2.1)$$

In the absence of a magnetic field or magnetic order in the crystal, the symmetry of these tensors reflects its crystal symmetry. In other cases, ϵ_{ik} and μ_{ik} become asymmetric. If both tensors are functions of the external field \vec{H} or magnetization \vec{M} , the following equations can be written for the transparent crystals (for simplicity we will consider magnetic insulators, but the approach can be generalized for conducting materials):

$$\epsilon_{ik}(\vec{M}) = \epsilon_{ki}(-\vec{M}), \quad \mu_{ik}(\vec{M}) = \mu_{ki}(-\vec{M}), \quad (2.2)$$

thus it follows for diagonal components:

$$\epsilon_{ii}(\vec{M}) = \epsilon_{ii}(-\vec{M}), \quad \mu_{ii}(\vec{M}) = \mu_{ii}(-\vec{M}), \quad (2.3)$$

i.e. the diagonal components are even functions of the magnetic field. Off-diagonal components of the tensor are odd functions of the magnetic field and give rise to gyrotropic components.

The absence of the absorption suggests that the ϵ and μ are Hermitian tensors:

$$\epsilon_{ik}^* = \epsilon_{ik}, \mu_{ik}^* = \mu_{ik}. \quad (2.4)$$

Here we obtain that the diagonal components of the dielectric tensor are real and off-diagonal are imaginary. If the magnetic field or the magnetization are pointing along the z axis we can write ϵ_{ik} (μ_{ik} in the same way) as follows:

$$\epsilon_{ij} = \begin{pmatrix} \epsilon_{xx} & i\epsilon_{xy} & 0 \\ -i\epsilon_{xy} & \epsilon_{yy} & 0 \\ 0 & 0 & \epsilon_{zz} \end{pmatrix} \quad (2.5)$$

where $\epsilon_{xx} = \epsilon_{yy} \neq \epsilon_{zz}$ are real.

2.1.2 FARADAY EFFECT

Here, we consider the basic MO effects which differ by the geometry of the observation i.e. relative orientation of the light and the magnetic field or magnetization. If linearly polarized light propagates through the crystal along the high symmetry axis and the magnetization (magnetic field) is pointing in the same direction (see Fig. 2.1 (a)), the axial symmetry around the magnetization leads to the existence of the two electromagnetic eigen-waves propagating through the crystal: left- and right- circularly polarized. These two waves interact with the crystal differently, hence, acquiring different phase velocities. As a result, the sum of these two waves upon exiting gives the crystal again linearly polarized light, the polarization plane of which has changed relative to the incoming light. The rotation angle ϕ of light polarization normalized to the crystal length can be expressed as

$$\phi/l = -\pi\epsilon_{xy}(\epsilon_{xx})^{-1/2}\lambda^{-1}, \quad (2.6)$$

where λ is a wavelength of light in vacuum. Such a rotation of the light polarization propagating through a magnetic crystal is called the Faraday effect. This effect is linear in magnetic field, i.e. the effect changes sign when the orientation of the magnetic field/magnetisation is reversed. Absorption of light by the media, i.e. the dielectric tensor having imaginary part written as

$$\epsilon_{ik} = \epsilon'_{ik} + i\epsilon''_{ik}, \quad (2.7)$$

gives rise to the difference in the decay of the two circularly polarized waves. In turn, the difference in the absorption between the right- and left-circularly polarized light is called magnetic circular dichroism (MCD).

2.1.3 VOIGT/COULTON-MOUTON EFFECT AND MAGNETIC LINEAR DICHROISM

If the light propagates perpendicular to the magnetic field/magnetization, the two special directions appear for \vec{E} parallel and perpendicular to the magnetic field (see Fig. 2.1 (b)). In

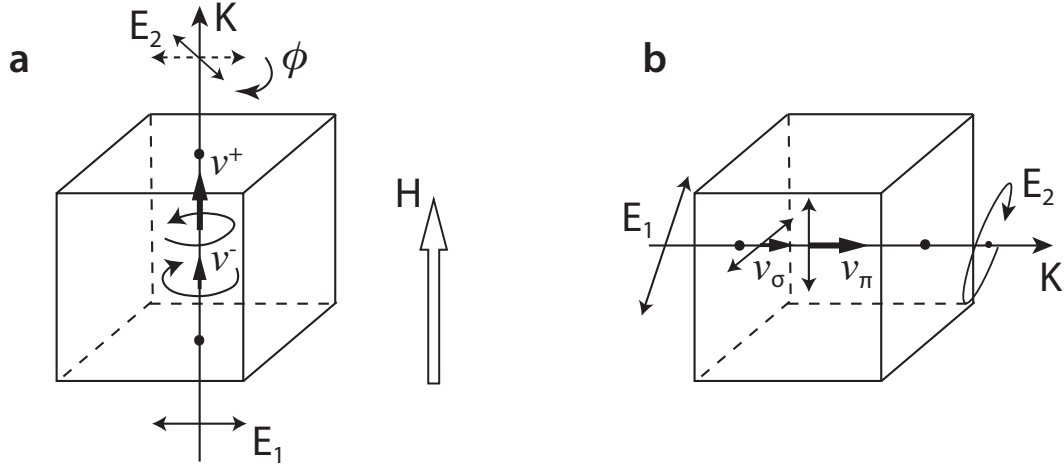


Figure 2.1: Geometry of the observation of the MO effects. (a) Faraday effect (linear), (b) Voigt or Couton-Mouton effect (quadratic).

the crystal, the two waves propagate with different phase velocities according to the effective dielectric constants

$$\epsilon_\pi = \epsilon_{zz} \quad \text{for} \quad \vec{E} \parallel \vec{M} \text{ (or } \vec{H}), \quad (2.8)$$

$$\epsilon_\sigma = \epsilon_{xx} - \epsilon_{xy}^2 / \epsilon_{xx} \quad \text{for} \quad \vec{E} \perp \vec{M} \text{ (or } \vec{H}).$$

Thus, the light polarized in arbitrary direction acquires an elliptical polarization proportional to \vec{M}^2 . The sign of the effect is independent of the magnetisation direction. This effect is called the Voigt or Couton-Mouton effect. Similarly to the case of the Faraday effect, the absorption coefficient will be different for the two orthogonal polarizations of light giving rise to magnetic linear dichroism (MLD).

Above the two extreme cases are described, when the light propagates parallel or perpendicular to the magnetization direction. In the general cases, when the light propagates at an angle to the magnetization, changes of the light polarization are defined by both effects and, as a result, two elliptical waves propagate through the crystal.

2.1.4 KERR EFFECT

Magneto-optical effects in **FM** materials can be also observed in a reflection geometry and in this case are referred to as the Kerr effects. Depending on the observation geometry, there are 3 types of Kerr effects: polar, longitudinal and transverse, all depicted in Fig. 2.2. In the general case, linearly polarized light becomes elliptically polarized after reflecting off a magnetized sample.

Polar Kerr effect appears when the magnetic field or the magnetization is perpendicular to the reflecting surface. In this case, the maximum effect can be observed when the incoming light is at normal incidence, i.e. the observation of the effect is in the same geometry as the Faraday effect but using the reflected light. For this geometry, a simple relation between the gyrotropic components of the dielectric tensor and the measured rotation angle ϕ and the ellipticity ξ of the reflected light reads:

$$\phi = -Im \frac{\epsilon_{xy}}{n(\epsilon_{xx} - 1)}, \quad \xi = -Re \frac{\epsilon_{xy}}{n(\epsilon_{xx} - 1)}, \quad (2.9)$$

where n is the refractive index. Thus, the polarization rotation of the reflected light is related to the imaginary part and the ellipticity is related to the real part of the off-diagonal elements of the dielectric tensor. In materials without absorption, the imaginary part of the off-diagonal elements of the dielectric tensor equals to zero, thus, for such materials, rotation of the polarization of the reflected light will not be observed. Again, polar Kerr effect is linear with respect to the magnetic field and changes sign when the sample is magnetised in the opposite direction.

In the case of the longitudinal Kerr effect, the magnetic field (the magnetization) lie in the incident plane and both polarizations of light interact with the magnetization. This effect is widely used for imaging of the magnetic domain structure of materials with an in-plane magnetization. The same way as in case of the polar Kerr effect, there is a projection of the magnetization on the \vec{k} vector of light. The polar and longitudinal Kerr effects together with the Faraday effect could be classified as longitudinal **MO** effects.

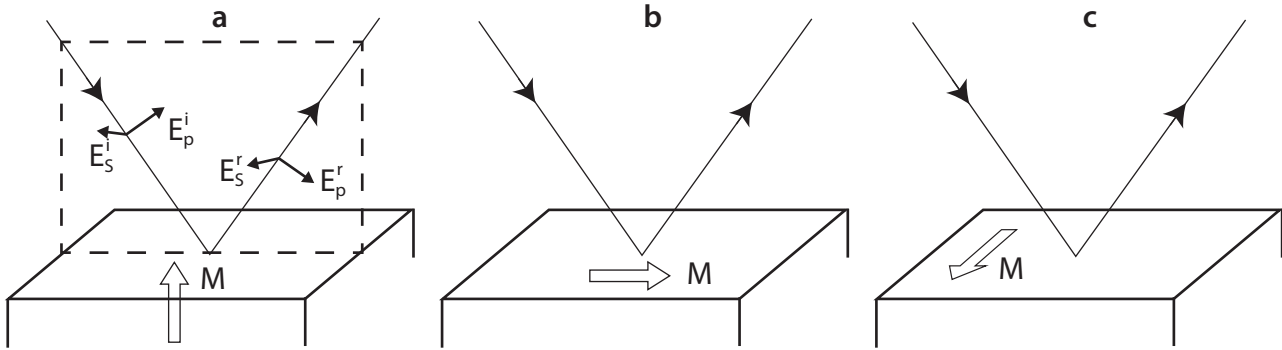


Figure 2.2: Three configurations in which the magneto-optical Kerr or Faraday effects can be observed: (a) polar, (b) longitudinal and (c) transverse.

In the case of the transverse Kerr effect, the magnetization is perpendicular to the incident plane and parallel to the surface of the sample. There is no interaction between the magnetization and the linearly polarized light parallel to the magnetization. The effect is observed only for the light polarized perpendicular to the magnetization. In terms of geometry it is the same as quadratic MO effects. However, the transverse Kerr effect is the first order MO effect and leads to changes of the reflectivity of the sample by several percent upon the magnetization reversal. Linear in the magnetic field transverse Kerr effect is observed only for absorbing materials, i.e. for non-zero imaginary parts of ϵ_{ik} . For the real part of the dielectric tensor and the light polarized in the incidence plane, only quadratic MO effect can be observed.

2.1.5 ISOTROPIC AND ANISOTROPIC CONTRIBUTIONS TO THE QUADRATIC MO EFFECTS IN A COLLINEAR ANTIFERROMAGNET

Contributions to the dielectric tensor related to the magnetic order can be phenomenologically described without making any assumption about the mechanism of the effect and using only symmetry considerations. The components of the dielectric tensor can be derived from the electromagnetic energy density expression, taking into account only the lower order

terms (quadratic) in the energy expansion of the AFM order parameter (Néel vector). For a tetragonal crystal, where z axis corresponds to the four-fold symmetry axis and x, y axes are along two two-fold symmetry axes, the energy density ε can be written as follows [50]:

$$\begin{aligned} \varepsilon = & \frac{1}{8\pi} [\epsilon_0 \vec{E}^2 + \lambda_1 E_z \vec{I}^2 + \lambda_2 (E_x^2 + E_y^2) \vec{I}^2 \\ & + \lambda_3 E_z^2 I_z^2 + \lambda_4 (E_x^2 + E_y^2) I_z^2 + \lambda_5 E_z I_z (E_x I_x + E_y I_y) \\ & + \lambda_6 E_z I_z (E_x I_y + E_y I_x) + \lambda_7 E_x E_y I_x I_y + \lambda_8 (E_x^2 - E_y^2) (I_x^2 - I_y^2)], \end{aligned} \quad (2.10)$$

where E_i are the components of the electric field, I_i are the components of the Néel vector ($\vec{I} = (\vec{M}_1 - \vec{M}_2)/2M_0$) and λ_i are the phenomenological constants. In Eq. 2.10, we assume that the MO effects are governed by the vector of antiferromagnetism (the Néel vector), since in collinear AFMs two magnetic sublattices are fully compensated. Differentiating ε with respect to E_i and E_k , the dielectric tensor is obtained

$$\epsilon_{ij} = \begin{pmatrix} \epsilon_{\perp}^0 + \lambda_2 \vec{I}^2 + \lambda_4 I_z^2 + \lambda_8 (I_x^2 - I_y^2) & \lambda_7 I_x I_y & \lambda_5 I_z I_x + \lambda_6 I_z I_y \\ \lambda_7 I_x I_y & \epsilon_{\perp}^0 + \lambda_2 \vec{I}^2 + \lambda_4 I_z^2 - \lambda_8 (I_x^2 - I_y^2) & \lambda_5 I_z I_y + \lambda_6 I_z I_x \\ \lambda_5 I_z I_x + \lambda_6 I_z I_y & \lambda_5 I_z I_y + \lambda_6 I_z I_x & \epsilon_{\parallel}^0 + \lambda_1 \vec{I}^2 + \lambda_3 I_z^2 \end{pmatrix} \quad (2.11)$$

Here, ϵ_{\perp}^0 and ϵ_{\parallel}^0 are the principle dielectric constants of a uniaxial crystal in the paramagnetic state. One can see that in every diagonal element of the tensor, a term proportional to \vec{I}^2 appears. This term does not depend on the orientation of the Néel vector with respect to the crystalline axis, i.e. it is isotropic with respect to the orientation of the Néel vector, which leads to changes of the refraction indexes of the material in the antiferromagnetic state. The relationship between λ_1 and λ_2 is governed by the crystal symmetry and, in cubic crystals, will be the same. Thus, the isotropic term does not change the number of the optical axes in the crystal - cubic crystal will stay optically isotropic, uniaxial crystal will stay uniaxial and so on. However the refractive index will change upon cooling through T_N . Thus, the isotropic magnetic birefringence for a uniaxial system is proportional to I^2 , such that

$$\Delta n_{iso} = \frac{I^2}{2} \left(\frac{\lambda_1}{n_{\parallel}} - \frac{\lambda_2}{n_{\perp}} \right), \quad (2.12)$$

where $n_{\parallel} = \sqrt{\epsilon_{\parallel}}$ and $n_{\perp} = \sqrt{\epsilon_{\perp}}$.

On the other hand, anisotropic terms with respect to the Néel vector also enter the dielectric tensor. Let us consider that $I_z = 0$, such that the Néel vector lies in the (001) plane. Therefore, the anisotropic terms of the diagonal components of the dielectric tensor will not be equal to zero, having opposite signs for ϵ_{xx} and ϵ_{yy} . This will lead to magnetic linear birefringence (MLB). Thus, in the case of transparent materials, linearly polarized light becomes elliptically polarized upon propagating through the crystal along the z axis. If the Néel vector is oriented along $[110]$ direction, the anisotropic terms of the diagonal components ϵ_{xx} and ϵ_{yy} equal to zero. Thus, the refraction indexes n_x and n_y are the same. However, in the coordinate system where x is along $[110]$ axis and y is along $[\bar{1}\bar{1}0]$, the refraction indexes are different. Thus, the isotropic MLB leads to the difference of the refraction indexes for linearly polarized light parallel and perpendicular to the Néel vector:

$$\Delta n = \frac{\lambda_8(I_x^2 - I_y^2)}{n_{\perp}}. \quad (2.13)$$

In reflectivity geometry, the reflection coefficient for the linearly polarized light along the Néel vector differs from the reflectivity coefficient for orthogonally polarized light. Hence, it results in the rotation of the light polarization if the polarization is canted from the Néel vector direction. Moreover, the material with non-zero off-diagonal components of the dielectric tensor gives rise to the Kerr effect, so in the general case, the reflected light is again elliptical.

2.1.6 WHAT TO MEASURE?

The discussion above brings us one step closer to the realization of a time-resolved experiment on AFM as it allows us to answer the first question “*What to measure?*”. In the case of AFMs, it is obvious to use magnetic linear dichroism as a tool for the detection of the magnetic order. However, the absence of the way to control the magnetic order makes the study of the MO effects challenging. This is further complicated by the likelihood of the

side effects, related to the geometry of the sample and imperfection of the optical elements, during an optical experiment, which can lead to misinterpretation of the experimental results. This is especially the case for Mn_2Au , where T_N can not be reached. Thus, in order to accurately characterise the MO effect in Mn_2Au thin films, the measurements carried out using a referenced scheme are discussed in the following section.

2.2 MAGNETIC LINEAR DICHHROISM IN Mn_2Au

The discussion below is based on Ref. [52].

2.2.1 EXPERIMENTAL APPROACH

The goal of the experiment is to determine the anisotropic magnetic contribution to dichroism, given by $\epsilon_{xx} - \epsilon_{yy}$, which depends on the (in-plane) Néel vector orientation. Such a MLD is expected to be in the range of 10^{-3} and could be overshadowed by extrinsic non-magnetic effects such as epitaxial strain. In particular, in the case of an additional lattice distortion in the ab -plane due to strain, ϵ_{\perp} (and λ_1 as well) would be different for the x and y directions, leading to reflectivity anisotropy in the ab -plane unrelated to the magnetic order. Furthermore, such extrinsic contributions may vary from sample to sample due to slight variation of substrate properties such as miscut. Thus, to unambiguously determine the MLD, measurements on different magnetically aligned parts of the same film are performed.

The Mn_2Au films were mounted such that their easy axes were along the horizontal/vertical directions, which corresponded to x and y directions of ϵ_{ij} . The light reflected from the sample was focused onto a photodiode and the AC signal was recorded using a digital oscilloscope. Measurements at multiple positions on each of the three measured samples were performed (the laser spot diameter on the sample was about $500 \mu m$) and averaged to minimize systematic errors.

In order to detect and characterise the [MLD](#) in Mn_2Au thin film one needs to consider several experimental problems. The main problem is that there is no easy way to control the Néel vector orientation which would enable measurements of relative changes of the optical properties. The way to align the Néel vector in Mn_2Au thin film is by application of an extremely high magnetic field (60 T) [[7](#), [20](#), [49](#)]. Such fields can be obtained only in a special pulsed magnets, which makes the *in-situ* optical measurements challenging. The second problem is the polarization dependent optical effects taking place at any optical element of the setup, mainly polarization dependent reflection at any surface. Thus, simple variation of the light polarization will accumulate a systematic error and may overshadow the possible effect. An alternative way is to rotate a magnetically polarized sample, but, as we will see later, the geometrical imperfections of the sample can cause a comparable effect. To circumvent these problems, the following requirements are proposed:

1. minimum number of optical components;
2. referenced measurement of the reflectivity asymmetry of two orthogonal polarizations;
3. measurement of the same film in different magnetic configuration.

To carry out a systematic measurement of the [MLD](#) in Mn_2Au , the as-grown sample is cut into 5×5 mm² pieces. The three pieces investigated are labeled as *A-C* (see Fig. [2.3](#)). Sample *A* is in the as-prepared state, i.e. in a multidomain configuration, and is used as a reference. Samples *B* and *C* are Néel vector aligned [[7](#), [20](#), [49](#)] in the pulsed magnetic field of 60 T along the different, yet crystallographically equivalent $\{110\}$ directions, as shown in the middle panel of Fig. [2.3](#). Here and throughout this chapter, the default film orientation is such that $x \parallel [010]_s$ and $y \parallel [211]_s$.

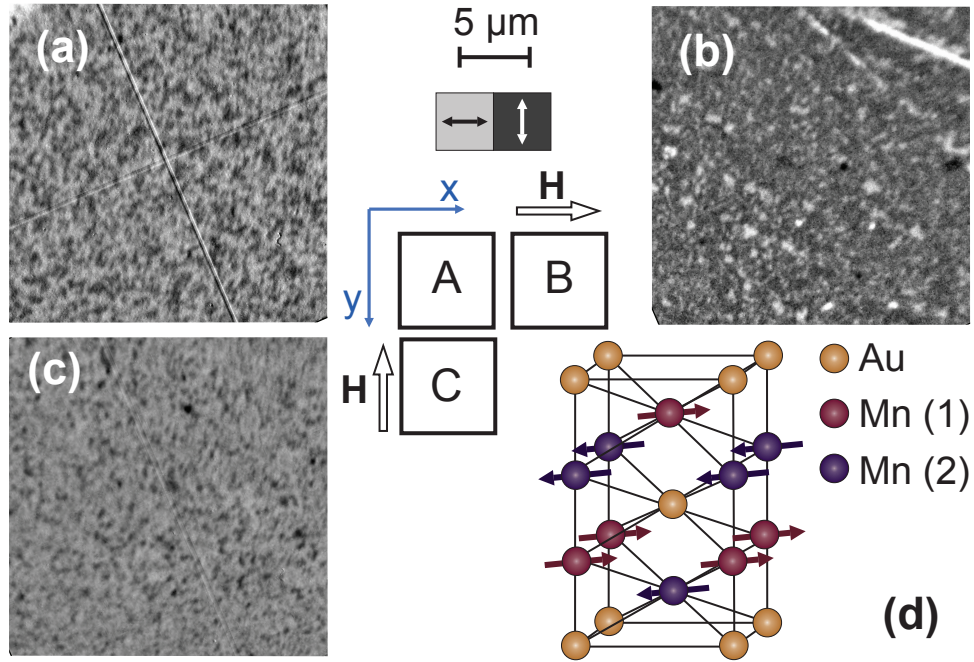


Figure 2.3: The layout (center of the figure) and the images of samples *A-C*, shown in panels (a)-(c), respectively. Sample *A* is in as grown state, while samples *B* and *C* are orthogonally polarized in the 60 T pulsed magnetic field. The directions of the applied magnetic field and the corresponding Néel vector directions are shown in the center, together with the scale of the XMLD-PEEM images. The XMLD contrast shows the two types of magnetic domains with the Néel vector along the two orthogonal easy axes: $[110]$ and $[1\bar{1}0]$. In the as-prepared sample *A*, roughly equal distribution of both types of domains is observed, while the aligned samples *B* and *C* display mostly one type of the domains. Adapted from Ref. [52] with permission.

2.2.2 AFM DOMAIN STRUCTURE IN ALIGNED Mn_2Au FILMS

Prior to optical studies one needs to confirm the different magnetic states of the samples. For this, we briefly discuss the AFM domain configuration of all of our samples, imaged by X-ray magnetic linear dichroism (XMLD)-PEEM. The principle of this technique is discussed in details in chapter 3. We just note here that bright/white areas correspond to the domains with the Néel vector aligned along $[110]$ direction and black areas correspond to domains with the Néel vector aligned along $[1\bar{1}0]$ direction.

As seen in Fig. 2.3, the AFM domain structure of the samples confirms that samples B and C have orthogonal orientation of the Néel vectors. Specifically, each of the polarized samples has mostly one type of AFM domains, with narrow worm-like domains of the other type, similarly to earlier reports [7, 48]. On the other hand, sample A has about equal distribution of the domains of both types, which is expected for a Mn_2Au film in the as-grown state. Hence, sample A is used as a reference in the following optical dichroism measurements.

2.2.3 EXPERIMENTAL SETUP FOR OPTICAL DICHROISM

The experimental setup is sketched in Fig. 2.4 (a). For the non-cubic material, the experimental reflectivity anisotropy can be a result of a finite angle of incidence. For the same reason, i.e. the difference in reflectivity between the p - and s -polarized light, any dielectric mirrors need to be avoided in the beam path. Therefore, it is not possible to use normal incidence and to separate the reflected light using a semi-transparent dielectric mirror. To minimize these effects, minimal angle of incidence of $\alpha/2 \approx 0.34^\circ$ is used. Moreover, we use a minimal number of the optical elements with the only reflecting surface being the surface of the sample as shown in Fig. 2.4 (a).

We use the 852 nm laser diode and a photo-elastic modulator (PEM) from Hinds Instruments, which operates at the frequency of 50 kHz. The PEM is set to $\lambda/2$ retardation mode

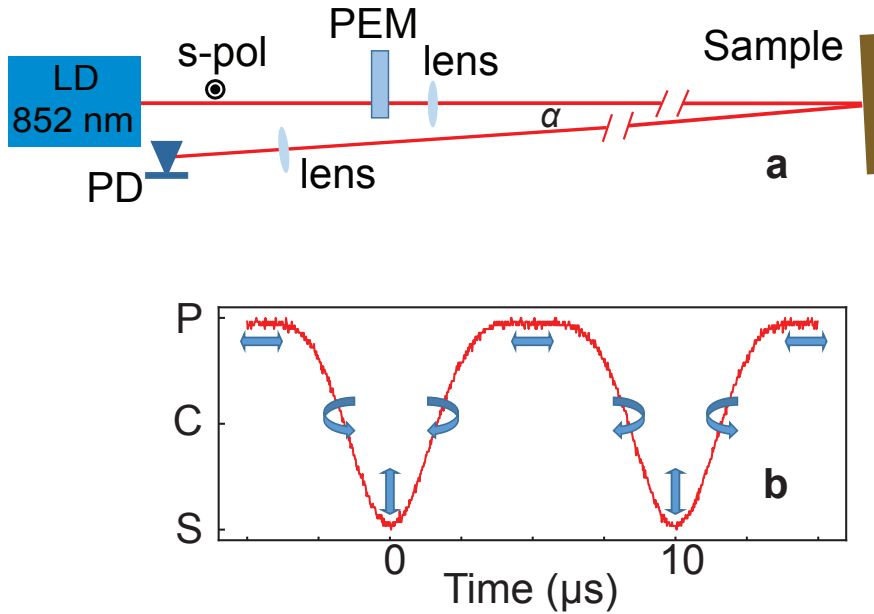


Figure 2.4: (a) Schematic of the experimental setup. The laser diode (LD) is vertically polarized. The polarization is modulated by the PEM operating at 50 kHz. (b) Polarization calibration curve measure, when polarizer inserted before the photo-diode (PD). Reproduced from Ref. [52] with permission.

for 852 nm, resulting in a modulation of light polarization between *s*-polarized (vertical) and *p*-polarized (horizontal) at 100 kHz, the second harmonic of the PEM (see Fig. 2.4(b)).

The distance between the laser diode and the sample is about 2.5 m, while the photodiode (PD) is mounted about 3 cm from the laser output, giving the aforementioned incidence angle of $\approx 0.34^\circ$. To calibrate the light polarization, time evolution of the intensity on the photodiode is measured when a polarizer is placed in front of the photo-diode, thereby selecting the horizontal (*p*-polarized) signal (the modulation period is 10 μs) as shown in Fig. 2.4 (b). The blue arrows represent the polarization state of the incoming light at given times, varying between vertical (*s*) and horizontal (*p*) polarizations that are along the $[110]/[1\bar{1}0]$ crystalline axes of Mn_2Au .

2.2.4 GENERAL SYMMETRY CONSIDERATIONS

As discussed above, in a tetragonal easy-plane system such as Mn_2Au , a symmetry-based phenomenological model of the quadratic MO effect generally implies two possible contributions to the MLD: an isotropic and an anisotropic one [50]. The isotropic contribution is independent of the direction of the Néel vector within the plane, and could be pronounced when the light propagates along a two-fold symmetry axis of the crystal (here, we consider the crystal symmetry only). On the contrary, the anisotropic MLD depends on the direction of the Néel vector [51] and is present when the light propagates along the four-fold symmetry axis (along the direction of the film normal). Therefore, to determine the Néel vector orientation in Mn_2Au , the anisotropic component has to be used.

Given the two possible directions of the Néel vector in Mn_2Au , we choose the z -axis to be along the four-fold [001] axis, while x and y coincide with [110] and $[1\bar{1}0]$ crystallographic axes. Rewriting Eq. 2.11 we obtain the corresponding dielectric tensor components for Mn_2Au with the tetragonal crystal structure and the Néel vector perpendicular to the four-fold symmetry axis (i.e. within the easy $a - b$ plane) [50]:

$$\epsilon_{ij} = \begin{pmatrix} \epsilon_{\perp} + \lambda_1 \vec{I}^2 + \lambda_3 (I_x^2 - I_y^2) & \lambda_4 I_x I_y & 0 \\ \lambda_4 I_x I_y & \epsilon_{\perp} + \lambda_1 \vec{I}^2 - \lambda_3 (I_x^2 - I_y^2) & 0 \\ 0 & 0 & \epsilon_{\parallel} + \lambda_2 \vec{I}^2 \end{pmatrix} \quad (2.14)$$

Here ϵ_{\perp} and ϵ_{\parallel} are the in-plane and out-of-plane dielectric constants in the absence of magnetic order, \vec{I} is the Néel vector and λ_i are the phenomenological coefficients related to the MLD. The difference between $\epsilon_{xx/yy}$ and ϵ_{zz} is governed by $\epsilon_{\perp} - \epsilon_{\parallel}$, yet includes also the component proportional to \vec{I}^2 , i.e. the isotropic component to the MLD. Note that the term proportional to \vec{I}^2 is likely negligible compared to $\epsilon_{\perp} - \epsilon_{\parallel}$. Nevertheless, the difference $\epsilon_{\perp} - \epsilon_{\parallel}$ may lead to the reflectivity anisotropy in non-normal incidence configuration.

2.2.5 DISENTANGLING MLD AND STRUCTURAL DICHOISM

In our experimental geometry, with x/y corresponding to horizontal/vertical light polarizations, the **MLD**, given by $\epsilon_{xx} - \epsilon_{yy}$ in Eq. (2.14), should result in a difference between reflectivities of the s - and p -polarized light. However, the weak modulation of the intensity of the reflected light is also expected due to effects related to the operation of the **PEM**, as well as due to possible structural/strain anisotropy. Thus, the modulation of light intensity on the photo-diode, $\Delta I = \frac{\Delta R}{R}$ (the reflectivity of Mn_2Au at 852 nm is about 0.52), can be expressed as:

$$\Delta I_i(\phi) = D_0 P(\phi) + D_{mag}^i P(\phi) + D_{str}^i P(\phi). \quad (2.15)$$

Here, D_0 is the contribution to the signal modulation related to the **PEM** operation and slight misalignment of optical components (present also when measuring uncoated gold mirror as a reference). D_{mag}^i is the amplitude related to the **MLD** of the sample, where i is the sample index (A, B, C). Finally, D_{str}^i is the amplitude of the dichroism caused by possible structural effects, such as epitaxial strain. Here, we assume that in the first approximation the structural/strain dichroism is decoupled from D_{mag}^i , i.e. the strain does not affect the Néel vector. Thus, we assume D_{str}^i is independent of the Néel vector direction, but depends on the sample orientation. Finally, $P(\phi)$ is a periodic function describing the polarization state of light after passing through the **PEM** (see Fig. 2.4 (a)). Since identical experimental geometry is used for all samples, D_0 is the same in all measurements. Moreover, given the samples A - C were cut from the same film, D_{str}^i should be identical to all samples, when mounted along the same direction with respect to the as-grown sample. Conversely, D_{str}^i should change sign when the sample is rotated by 90° around the C_4 axis, i.e. $D_{str}^i = -D_{str}^{i(90)}$. When considering the **MLD**, $D_{mag}^A \approx 0$, given the multidomain state on the length-scale of the laser spot size of $500 \mu\text{m}$. Finally, taking into account orthogonal directions of the Néel vectors in the two magnetically aligned samples, $D_{mag}^B = -D_{mag}^C$. Under these assumptions the structural and magnetic contribution can be disentangled by the following referenced

measurements:

$$D_{mag}P(\phi)/2 = \Delta I_B - \Delta I_A = \Delta I_A - \Delta I_C \quad (2.16)$$

$$D_{str}P(\phi) = \Delta I_A - \Delta I_A^{(90)} = \Delta I_B - \Delta I_C^{(90)} \quad (2.17)$$

2.2.6 RESULTS

Figure 2.5 presents the results of dichroism measurements, performed in sequence, under identical conditions. The dashed black line, representing the evolution of the polarization state of light (see Fig. 2.4) is added to all panels as a guide to the eye. Panel (a) presents the raw data, $\Delta I_i(\phi)$, taken on samples A , B and C . The complicated shape of the raw signal is largely a result of the optical elements of the setup, mainly the PEM. The PEM acts as a $\lambda \cdot \delta$ wave plate, where δ is modulated between $-1/2$ and $1/2$. This results in a sequence of polarization states s - p - s - p - s within one modulation period of the PEM ($20 \mu s$). Note that between the two linear polarizations, the light attains circular/elliptical polarizations. Due to imperfections and especially the asymmetry between the optical properties of the squeezed and elongated PEM crystal a modulation of the signal at 50 kHz is also observed. The zero level of every curve corresponds to the time averaged value of the signal.

To obtain the MLD component we first subtract the signal of the reference sample (as-prepared, A) from signals obtained on the magnetically polarized samples B and C , following Eq. 2.16. Moreover, as the MLD should give rise to a periodic modulation in reflectivity at the second harmonic of the PEM frequency, we fold the data recorded over two periods into the $10 \mu s$ time window. The resulting variations are shown in Fig. 2.5 (b). The differential signals do not have a complicated shape of the raw data as in Fig. 2.5 (a), demonstrating that reference subtraction efficiently cancels out all system related modulations. Indeed, the shape of the differential signal follows the shape of the reference curve (dashed line in Fig. 2.5 (b)). Furthermore, the absence of modulation of the differential signal at 50 kHz PEM frequency clearly confirms the absence of circular dichroism.

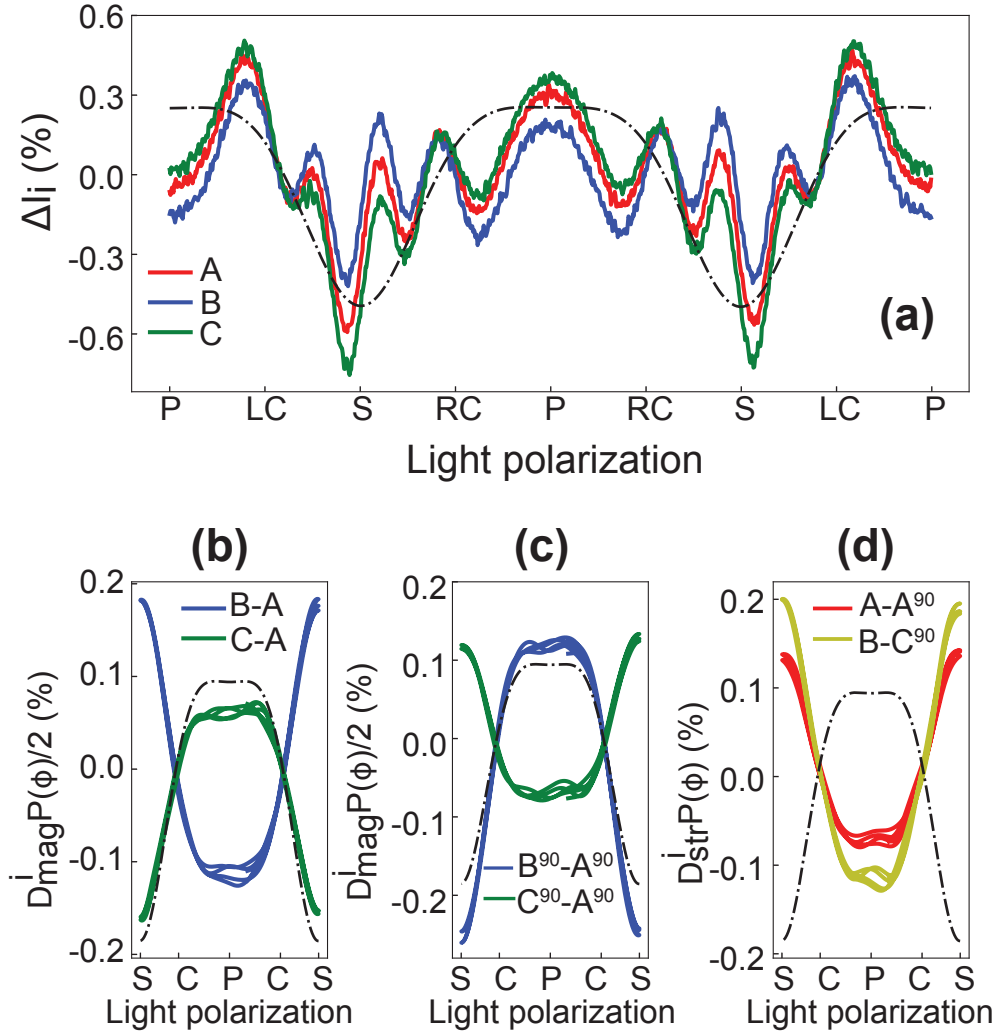


Figure 2.5: Results of reflectivity anisotropy studies on magnetically ordered Mn_2Au . (a) The raw reflectivity modulation signals from all three samples, oriented in the same growth direction (raw data obtained on samples rotated by 90° around the C_4 axis is not shown). Here S, P, LC and RC stand for the s-polarized, p-polarized, and left and right circularly polarized light, respectively. The time window here is $20 \mu s$. Panels (b)-(d) present the differential signals, disentangling the **MLD** and structural contributions to reflectivity variation according to Eqs. 2.16 and 2.17. Here the traces recorded over $40 \mu s$ have been folded into the $10 \mu s$ time window to emphasize the lack of any circular dichroism, which should have a 50 kHz component. The modulation in (b) and (c) is a result of the **MLD**, while the modulation in (d) reflects the structural component to dichroism. Reproduced from Ref. [52] with permission.

Figure 2.5 (c) presents the result obtained by the same approach, but for samples rotated by 90° around the C_4 axis. The fact that the differential signals $\Delta I_B^{(90)}(\phi) - \Delta I_A^{(90)}$ and $\Delta I_C^{(90)}(\phi) - \Delta I_A^{(90)}$ in panel (c) are phase-shifted by π underscores the MLD nature of the differential signals. Note that the MLD-induced change in reflectivity is $\approx 0.6\%$, given that $\approx 0.3\%$ effect shown in Fig. 2.5 (b) and (c) is relative to the reference unpolarized sample A. It is also important to note that the reflectivity is higher for the light polarized parallel to the staggered magnetization.

Finally, Fig. 2.6 (d) presents the results of measurements of structural component. Following Eq. 2.17, for differences $\Delta I_A(\phi) - \Delta I_A^{(90)}(\phi)$ and $\Delta I_B(\phi) - \Delta I_C^{(90)}$ the signal due to the MLD should cancel out and the remaining variation of reflectivity is due to structural/strain effects. From the observed D_{str} it follows that the reflectivity is larger for light polarized perpendicular to the direction of the c -axis tilt, discussed in the following section. Since $\Delta I_A(\phi) - \Delta I_A^{(90)}(\phi)$ captures the full contribution to the structural dichroism, it follows that for these samples the structural dichroism is about twice smaller than the MLD.

We note that the signals in panels (b)-(d) of Fig. 2.5 display slightly different amplitudes. This may suggest some correlation between the microstructural strain and the magnetic order. In other words, the underlying strain may give rise to an asymmetry between the volume fractions of orthogonally oriented domains in the field-polarized samples, as well as in the as grown sample.

2.2.7 THE POSSIBLE ORIGINS OF STRUCTURAL DICHROISM

While our data clearly demonstrate the presence of a substantial MLD in Mn_2Au , there are two possible origins giving rise to the structural component of the measured reflectivity anisotropy observed in Fig. 2.5 (d). To address these, we first need to consider the specifics of the epitaxial film growth on r -cut sapphire using the Ta (001) buffer layer [45, 46].

As mentioned in section 1.2.6 and elaborated elsewhere [44, 47], the c -axis of the Mn_2Au films grown on $(1\bar{1}02)$ Al_2O_3 is tilted with respect to the surface normal by about $2-3^\circ$ (the

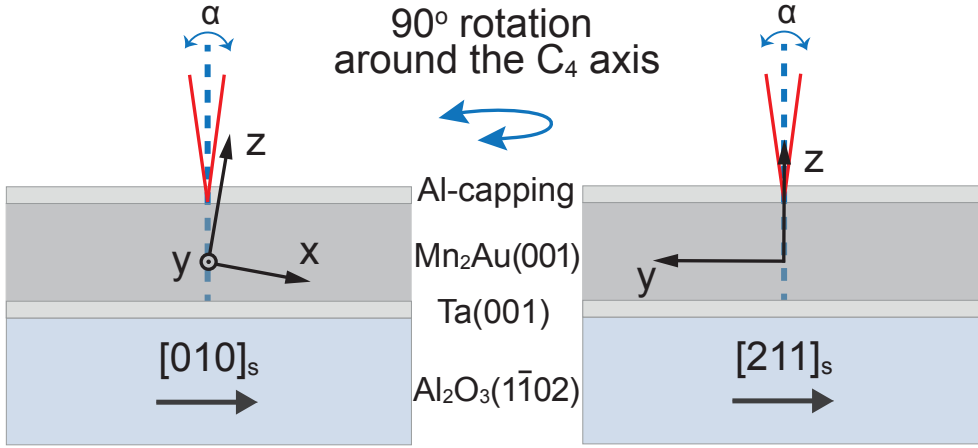


Figure 2.6: Schematic of the sample layout in dichroism measurements for the two different orientations of the sample (left and right) with respect to the laser beam directions (red lines). Here x and y correspond to $[110]$ and $[\bar{1}\bar{1}0]$ directions of Mn_2Au , while z is parallel to the c -axis, $[001]$. The tilt of the c -axis is highly exaggerated. Reproduced from Ref. [52] with permission.

tilt shows small variation from sample to sample). It turns out that the c -axis of the film tilts towards the $[010]_s$ axis of the substrate.

Given the tilted growth, the observed structural dichroism could be a result of the experimental geometry as illustrated in Fig. 2.6. Namely, due to the tilt of the film's c -axis with respect to the surface normal, the rotation of sample by 90° (or equivalently by rotating the light polarization) changes the projection of the \vec{k} vector of light onto the c -axis. The difference between ϵ_\perp and ϵ_\parallel can thus give rise to reflectivity modulation. Unfortunately, due to the lack of data on (anisotropic) optical properties of Mn_2Au , this contribution cannot be estimated.

On the other hand, the observed dichroism can arise due to the underlying strain as a result of the anisotropic thermal expansion of sapphire [53, 54]; such an effect can not be neglected on the low-symmetry cut of the Al_2O_3 . Indeed, investigations of sample morphology using atomic force microscopy suggest breaking of the four-fold symmetry [46]. Considering

the underlying strain to be responsible for the non-magnetic components of dichroism, its amplitude could roughly be estimated from D_{str} . Assuming a linear relation between D_{str} and the relative difference in the $[110]/[1\bar{1}0]$ lattice spacings, the latter should be of the order of 0.1 %. Using the X-ray diffraction (XRD) measurements we are, however, unable to resolve such a weak asymmetry between the $[110]$ and $[1\bar{1}0]$ lattice spacing parameters, because of the rather large mosaicity of $\approx 0.5^\circ$ [45, 46].

From Fig. 2.5 (b) and (c) it follows that the MLD is larger for sample *B*, the sample that is field-polarized along the direction of the *c*-axis tilt (parallel to the $[010]_s$ axis of the substrate). At face value, this may suggest the underlying microstructural strain to favor this orientation of the Néel vector. Indeed, study using scanning electron microscopy with polarization analysis seems to support this observation [55].

2.3 CONCLUSION

In conclusion, in this chapter we demonstrate a pronounced magnetic linear dichroism in near infra-red (NIR) range in a collinear metallic antiferromagnet Mn_2Au , which enables optical read-out of the direction of the staggered magnetization (Néel vector). The observed MLD of 0.6% exceeds the value of anisotropic magnetoresistance (AMR) in Mn_2Au [20] by about a factor of four. Recent broadband terahertz study of several ferromagnets demonstrated AMR signals up to 30 THz [56], with the effect slowly decreasing with increasing frequency. However, the large difference between the observed MLD in the near-infrared and the AMR in Mn_2Au [20] implies the MLD in the NIR to be a result of the polarization dependent interband absorption. Indeed, the recent angular-resolved photoemission spectroscopy study does show that the Néel vector orientation leads to a pronounced valence band asymmetry up to binding energies of several eV [49]. Further systematic studies of MLD as a function of photon energy may reveal spectral ranges with even higher MLD.

Furthermore, as a simple table-top experiment, the presented approach can be extended

to imaging mode, enabling detection of Néel vector orientation with micrometer spatial resolution. Finally, in view of potential applications of Mn_2Au , e.g. as a spintronic memory device, utilizing sequences of femtosecond optical pulses can provide read-out speeds matching the expected ultra-fast switching times in [AFM](#) memory devices.

Optical manipulation of the Néel vector in Mn_2Au

In this chapter, we demonstrate the optical control of the magnetic order of a collinear [AFM](#) Mn_2Au . The switching of the Néel vector, as confirmed by direct [XMLD-PEEM](#) imaging of the [AFM](#) domain configuration, is discussed. Thus, to understand the results, we first consider the basics of synchrotron radiation followed by the description of the mechanism of [XMLD](#), which is widely used for studying magnetic properties of [AFM](#) materials. The second part presents the experimental results showing the way how to reproducibly and selectively control the orientation of the Néel vector by optical activation of strain-induced domain wall motion.

3.1 XMLD-PEEM

Magneto-optical effects can provide a lot of information about integral characteristics of a magnetic material on the length-scale of the beam spot size, which is limited by the wavelength. Combined with a time-resolved approach, these can be used to detect the dynamics

of the magnetic order, but only if this dynamics is reversible. However, the resolution of optical microscopy based on the MO effects is limited by the wavelength, which may not be sufficient for the such micrometer size magnetic domains. Thus, a more advanced imaging technique for studying microscopic magnetic structures and their manipulation is required. The technique of choice for this is the X-ray photo emission electron microscopy (PEEM) in combination with X-ray magnetic linear dichroism (XMLD) effect. For such an experiment, a tunable source of X-rays is needed. A suitable source of light, which can be tuned over a broad range of energies and polarizations is a synchrotron. Therefore, in this section, we start by introducing the principles of synchrotron radiation, then the concept of an electron microscope is described and finally the microscopic mechanism of the XMLD effect is explained.

3.1.1 SYNCHROTRON RADIATION

As it follows from electrodynamics, any charge accelerating should radiate and lose energy. There is a rumor that once all atoms in the universe almost collapsed due to this fact. We are lucky though that this is not the case for the atoms. Nevertheless, one can use this fact to generate radiation. In the simplest case, accelerated electrons collide with a metal and rapidly lose their kinetic energy. As a result, X-rays are generated. This radiation is called *Bremsstrahlung*. In order to use this radiation for precise measurements, a stable source of the accelerated electrons is needed. For this purpose a synchrotron is commonly used.

As schematically illustrated in Fig. 3.1, after emission from an electron source, electrons first accelerate in a linear accelerator, then enter a booster ring to reach sub light velocity/energy of 1-3 GeV. Afterwards, bunches of electrons travel around a storage ring. The storage ring consists of straight segments forming a polygon. In the linear part, the electrons are propelled forward by a microwave field, produced by rf-cavities. In the rf-cavities, an oscillating electric field is generated, forming a so called rf-bucket for the moving electrons. The electrons which fit into this bucket, in turn, form an electron bunch with the length

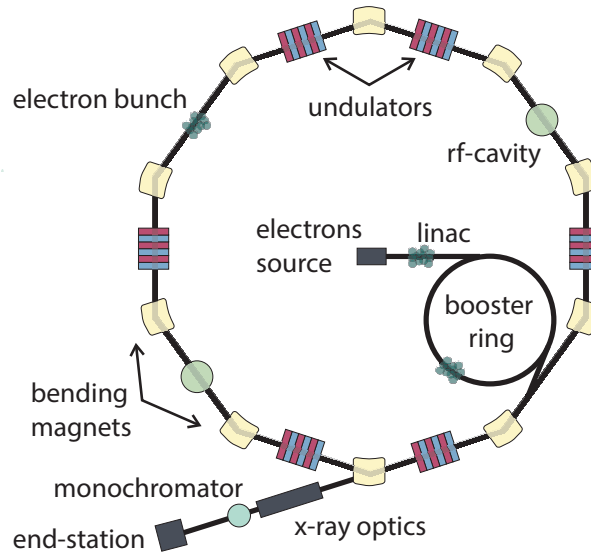


Figure 3.1: Sketch of a synchrotron light source with the relevant components indicated.

$l = 10$ mm, in the stationary frame of an observer. This length corresponds to a pulse length $\tau = l/\beta c = 30$ ps. One electron bunch consists of approximately 10^{10} electrons.

Between two neighboring straight sections one needs to turn the electron bunches. For this reason, dipole magnets (bending magnets) are used. Here, the trajectories of the electron bunches bend due to the Lorentz force, when electrons are traveling through the vertical magnetic field lines. Here, the electrons accelerate, thus emitting X-ray radiation. In general, this radiation can already be used for experiments.

In the new generation of synchrotrons, another part is used for X-ray generation - undulators, which consist of an array of antiparallely configured magnets, producing an oscillating magnetic field for the moving electrons. As a result, the electrons deflect periodically and due to the constructive interference of the radiation from different parts of the trajectory a coherent X-ray pulse is generated. After passing through an undulator, the electron bunch continues to travel along the same linear trajectory as before. Using different undulator configurations, i.e. different trajectory of the electrons, one can get either linearly or circularly polarized X-ray light. Then, the X-ray pulse enters a beamline, where along the way passing

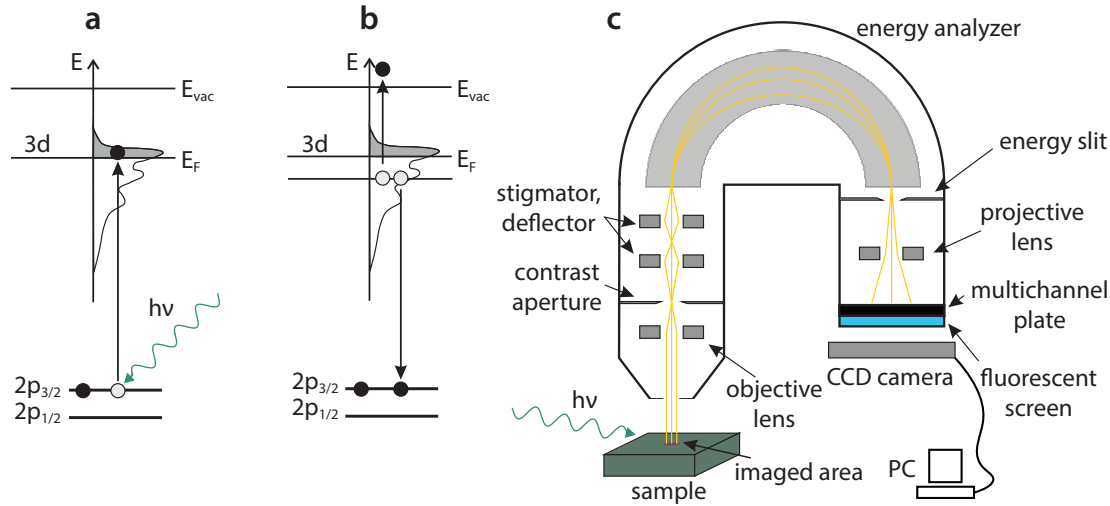


Figure 3.2: Sketch of the photoexcitation process leading to the generation of the secondary electrons in PEEM. (a) Absorption of an energetic X-ray photon leads to the transition of a core electron to the Fermi level, leaving behind a core hole. (b) An electron from the Fermi level recombines with the core hole causing a cascade of Auger and secondary electrons which may escape to the vacuum and can then be detected by PEEM. (c) Schematic of a PEEM setup.

through a monochromator acquires a precise energy with high narrow bandwidth.

A large variety of experiments can be performed using synchrotron radiation, limited only by the imagination of the experimentalists and their budgets. In the next section only one technique, which was used in this work, is described - Photo Emission Electron Microscopy (PEEM).

3.1.2 PHOTO EMISSION ELECTRON MICROSCOPY

Once X-ray light is generated, we can use it to study materials, in this case magnetic materials. An X-ray photon with a certain energy interacts with the core level electron of a magnetic atoms, exciting it to the Fermi level, thus generating a hole at the core level. By recombination of this hole, secondary electrons are generated as shown in Fig. 3.2 (a,b).

Due to the Auger processes and inelastic scattering of secondary electrons, a cascade of the electrons is generated, having the energy in a wide range between the photon energy of the initial X-ray pulse and the work function of the material. Thus, some of the electrons have enough energy to escape the material into vacuum. These electrons can be used to make an image of the surface of the material. For this, the electrons are first accelerated by 10-20 kV voltage applied between the sample and the objective of the microscope. Then, they enter a series of electron optics to be projected on a multichannel plate and then on a phosphorus screen. The image is digitized by a CCD camera and can be observed with a video rate (see Fig. 3.2 (c)).

The image is amplified and has a spatial resolution of $\simeq 20$ nm [57], in the case of maximum amplification (and close to an ideal sample surface), which is limited by the electron optics of the microscope and X-ray bandwidth. The optical column of the microscope has an energy analyzer which is a semi-sphere with an electric field applied perpendicularly to the velocity vector of the electrons. Thus, only the electrons with a certain kinetic energy can pass through. The energy resolution can be increased by inserting an energy aperture in the electrons path.

By itself, PEEM enables imaging of the surface of a sample, being sensitive to the elements, whose core levels correspond to the energy of the X-ray photons. But, in general case, a PEEM image does not contain any information about the magnetic structure of the sample. However, utilizing magnetic effects like X-ray magnetic circular dichroism (XMCD) for ferromagnets or X-ray magnetic linear dichroism (XMLD) for antiferromagnetic materials, the magnetic contrast can be generated. It requires comparing two images obtained either using different polarizations of X-rays or different X-ray energies. The mechanisms of the XMLD and XMCD effects are described in the next section.

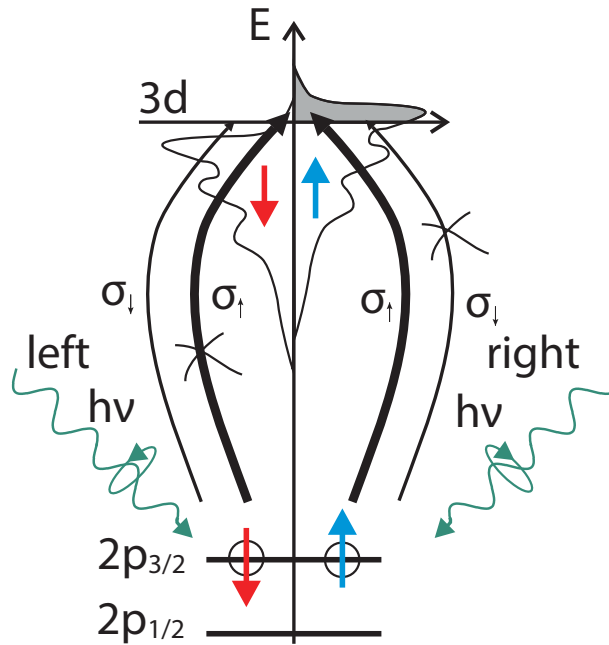


Figure 3.3: Schematic illustration of the mechanism of the [XMCD](#) effect. Electronic states for a transition metal, where the valence band is represented by the spin-up and spin-down d sub-bands and the L_3 transition is indicated. Spin-up photoelectrons are more readily excited from the $2p_{3/2}$ level with right-handed circularly polarized light to the partially unfilled $3d$ valence spin-up band because the dipole operator does not allow spin-flips during excitation.

3.1.3 XMCD AND XMLD

In order to obtain a magnetic contrast, i.e. to be able to image magnetic domains, one needs to find the dependence of the intensity on the microscope screen on the spin orientation of magnetic atoms. In fact, the intensity on the microscope is given by the number of electrons, excited from the material. The number of the excited electrons is, in turn, proportional to the absorbed energy. That is why imaging is usually done using a photon energy at the maximum of the absorption. Thus, the question of the intensity is transformed into the question of the X-ray absorption. Luckily, the latter depends on the orientation of the spins with respect to the X-ray light polarization.

Following the discussion in Ref. [16], absorption of X-ray photons depends on the concentration of the core level electrons and the number of the unoccupied states at the Fermi level, as schematically illustrated in Fig. 3.3. In the case of $3d$ metallic ferromagnets, the d -band is asymmetric for spin-up and spin-down. Thus, the density of the available states at the Fermi level is different for the electrons with different spins. It is possible to selectively excite either spin-up or spin-down electrons from the spin-orbit split core levels with right- or left- circularly polarized photons, due to the dipole selection rules. According to these rules, the transition is only possible when the following requirements are fulfilled: $\Delta m_l = \pm 1$ and $\Delta m_s = 0$, where m_l is the orbital moment quantum number and m_s is the spin quantum number. Following these rules the absorption of right and left circular X-rays is different for one particularly oriented domain of a ferromagnet. The magnetic contrast, in this case, can be generated by subtracting two images obtained with right- and left- circularly polarized X-rays.

This method does not work for antiferromagnets since the spins are oriented antiparallel and do not lead to the necessary energy band asymmetry at the Fermi level. However, in the presence of SOC one can imagine that the antiparallel arrangement of the spins modifies the electronic state such that it breaks the symmetry of the charge distribution. To illustrate this, the XMLD effect in NiO is often considered [16]. There, in a paramagnetic state, the charge distribution of the d -electron is spherical and the absorption of linearly polarized X-rays does not depend on the orientation of the light polarization. Once the magnetic order appears, the charge distribution becomes distorted along the spins orientation.

In the classical approximation, the efficiency of the interaction of an oscillating electric field with a charge depends on the projection of the charge distribution onto the polarization plane. In the exaggerated case, when the charge distribution is infinitely elongated, forming a delta function, the absorption of X-rays is maximal when light is polarized along the charge distribution and equals to zero when the polarization is perpendicular to the charge distri-

bution. In the case of NiO, the elliptical distortion of the d -electron charge distribution leads to a slight asymmetry of the absorption for the X-ray polarized parallel and perpendicular to the Néel vector. In other words, absorption of the linearly polarized X-rays depends on the mutual orientation of the light polarization and the Néel vector.

The **XMLD** effect is widely used for imaging **AFM** domains [7, 58, 59]. In an ideal case, the magnetic contrast is generated by subtracting images obtained with two orthogonal polarizations of the X-ray light, parallel and perpendicular to the Néel vector. In a real experiment, however, one should consider the geometry of the setup. In the setup which was used in this thesis, the incidence angle of the X-rays is approximately 74° . In this geometry, s -polarized X-rays probe the in-plane electronic structure, while p -polarized light probes both the out-of-plane electronic structure as well as in-plane. Nevertheless, the magnetic contrast is contained in any image obtained with X-rays linearly polarized along one of the easy axes of the Néel vector. To extract it, one needs to first normalize the image to make the magnetic contrast visible by subtracting the morphology image. This will work with two orthogonal polarizations. Alternatively, magnetic contrast can be generated by subtracting two images obtained at two X-ray photon energies, which correspond to minimum and maximum of the **XMLD** signal.

It is sufficient, if the **XMLD** signal is higher than the sensitivity which corresponds to several digits of a CCD camera. One pixel of a CCD camera is usually encoded in 8 bit, so that maximum intensity corresponds to 256. Let us assume that in order to resolve the magnetic contrast one needs to have an intensity distribution in the range of about 10 digits. Thus, the requirements for **XMLD** to be observed can be calculated as

$$\delta I_{XMLD} = \frac{I_{\perp} - I_{\parallel}}{2I} = \frac{10}{256} = 4\%.$$

3.1.4 XMCD CONTRAST IN MN_2AU

It turned out that in Mn_2Au , it is also possible to acquire magnetic contrast in the **XMCD** configuration. While the mechanism of the effect is not completely clear, the results can be

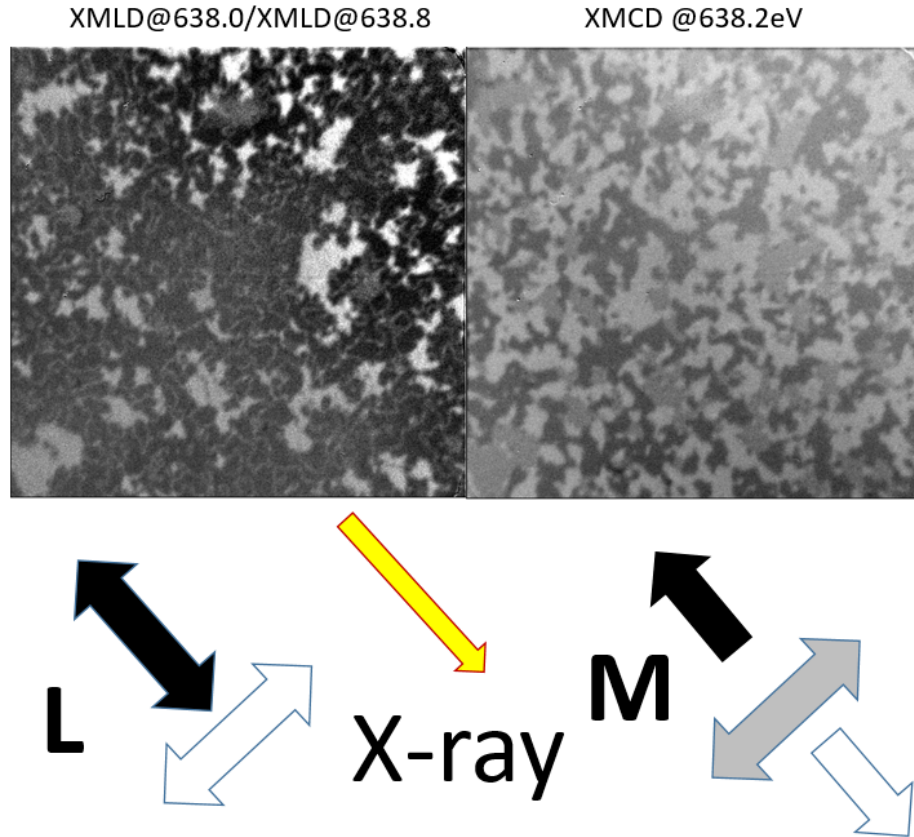


Figure 3.4: XMLD- (left) and XMCD- (right) PEEM images of Mn_2Au . The gray color code represents the orientation of the Néel vector (\vec{L}) and the magnetization (\vec{M}) relative to the X-ray propagation direction.

used for further discussion. Figure 3.4 shows the XMCD contrast obtained as a difference of the images acquired with left and right circularly polarized X-rays. Unlike usual XMCD in ferromagnets, the maximum of the XMCD contrast is observed at the X-ray energy of 638.2 eV, which does not correspond to the absorption maximum of Mn.

As clearly seen in Fig. 3.4, the XMCD contrast gives three colors in the PEEM image. By careful examination, we conclude that the black and white areas in XMCD correspond to domains with the Néel vector aligned antiparallel to each other and laying in the plane of incidence of X-ray beam. These domains have the same color in the XMLD image. Gray

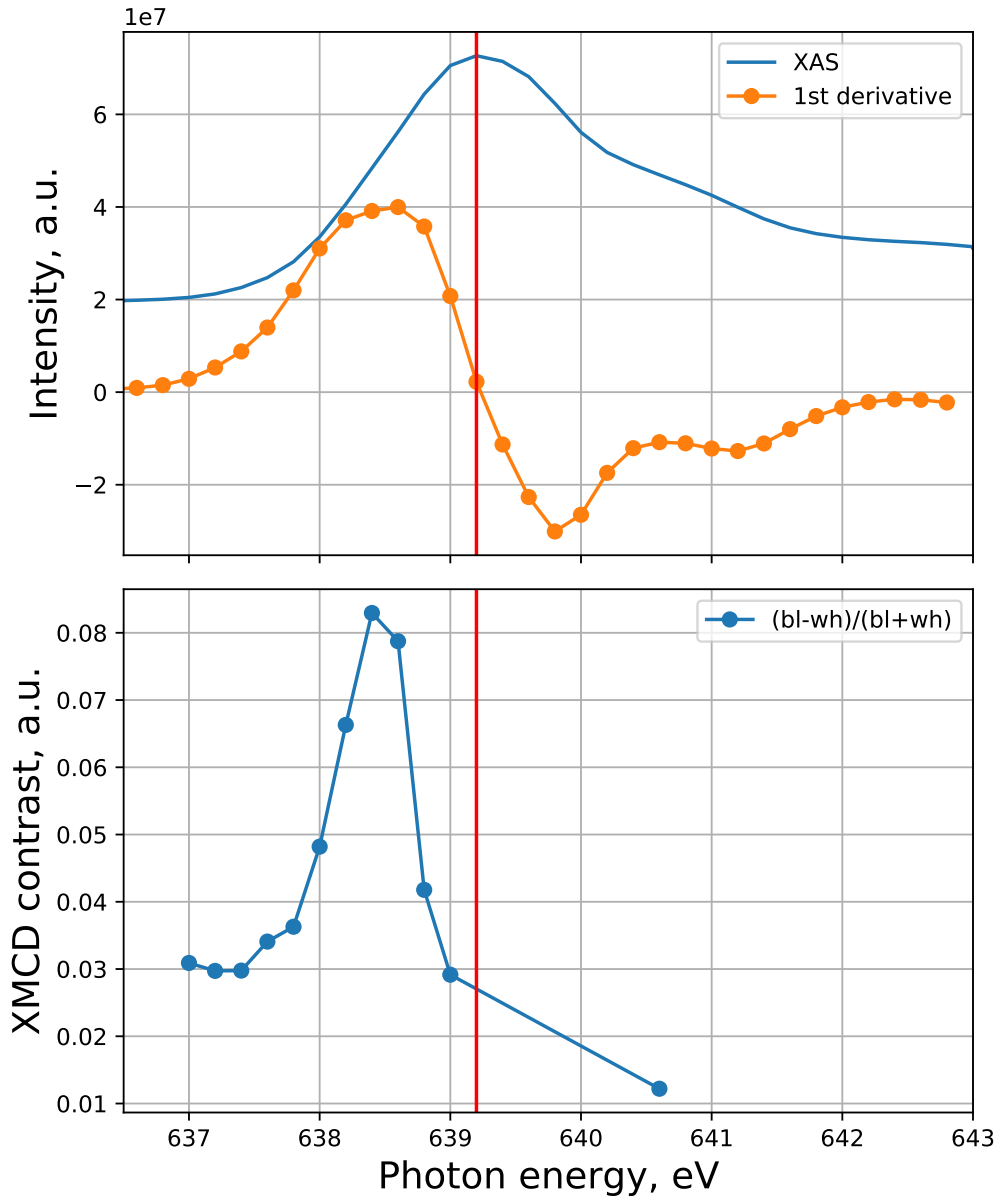


Figure 3.5: X-ray absorption spectrum (blue in the top panel) and the XMCD contrast (bottom) plotted as a function of the X-ray energy. In the top panel, the orange curve represents the first derivative of the intensity with respect to the photon energy. The red vertical line indicates the maximum of Mn L_3 absorption edge.

areas in XMCD correspond to domains with the Néel vector pointing perpendicular to the X-ray propagation. However, the exact direction in which the Néel vector is pointing within these domains is impossible to resolve due to the geometry of the XMCD effect. This could be distinguished by rotating the sample by 90° . Thus, comparing two magnetic contrasts in Fig. 3.4, one can conclude that the narrow worm-like domains in the XMLD image correspond to the border between two domains with the oppositely oriented Néel vectors. Hence, these worm-like domains are actually the 180° degree domain walls.

The discussion about a possible mechanism of the observed XMCD contrast in Mn_2Au can be wrapped in one question: “*Is it a bulk or a surface effect?*”? To answer this, one needs to carry out additional experiments aimed at modification of the samples surface. Given that XMLD is a bulk effect, by destroying the surface one can expect to detect the inconsistency of the XMLD and XMCD, which will confirm the surface origin of the XMCD signal. In this case, the mechanism will be simply the surface ferromagnetism. Meaning that the top Mn layer of Mn_2Au behaves as an uncompensated ferromagnet making the density of states (DOS) at the Fermi level asymmetric. Since the probing depth of PEEM is limited to a few nm, unequal contribution to the signal intensity from the top layer and the next layers can be assumed, which leads to the asymmetry of the photoemission.

On the other hand, the maximum of the XMCD contrast is observed at the X-ray energy, which does not correspond to the Mn L_3 absorption edge. Rather, it corresponds to the maximum of the derivative of the absorption spectrum as seen in Fig. 3.5. This is unusual for ferromagnets. Alternative version of the origin of the XMCD contrast could be the quadruple contribution to the DOS asymmetry [60]. In this case, the effect is expected to have a bulk origin and can be applied to other collinear AFMs. As mentioned above, this requires further investigations.

However, our recent data (see Fig. 3.6), obtained by PEEM imaging of the same area recorded over extended period of time (recording images on sequence), present preliminary

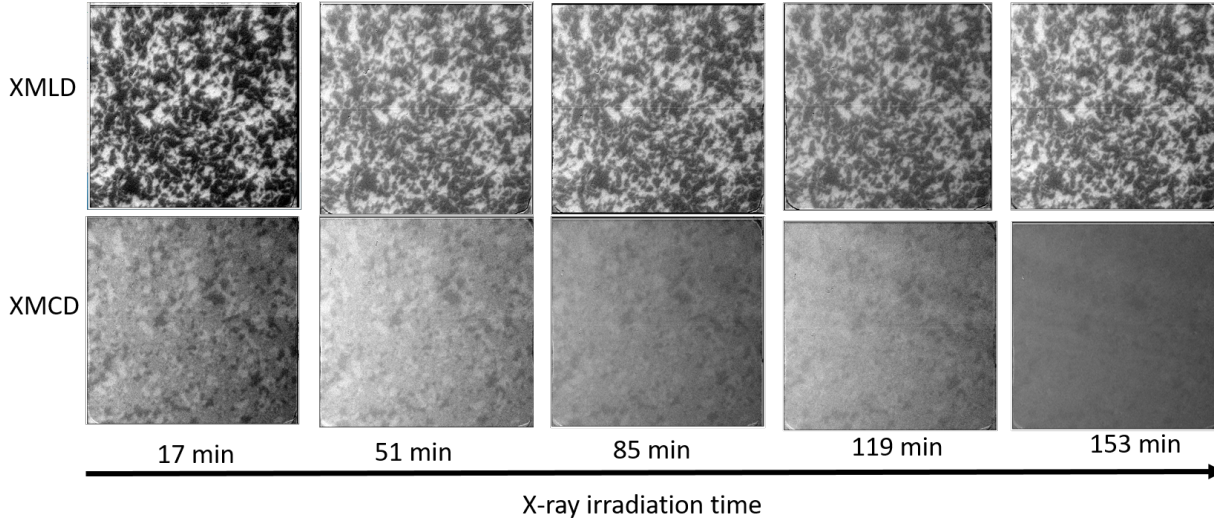


Figure 3.6: Comparison of the [XMLD](#) and [XMCD](#) contrast as a function of X-ray irradiation time.

experimental evidence towards the surface origin of the [XMCD](#). One can see that the [XMCD](#) contrast degrades with the time of X-ray irradiation, while [XMLD](#) contrast stays approximately the same. We speculate, that the intense X-ray beam irradiation leads to degradation of the surface [61] or, for example, carbon contamination [62], hence reducing the contribution of the surface uncompensated ferromagnetism to the [XMCD](#) effect.

3.2 MANIPULATION OF A COLLINEAR METALLIC ANTIFERROMAGNET WITH FEMTOSECOND OPTICAL PULSES AND EXTERNAL STRAIN

As discussed before, there is no easy way to reproducibly control the Néel vector in a collinear [AFM](#). A strong magnetic field allows to align the entire sample [7] and the current-induced switching requires specially designed microstructures [20]. Moreover, during the electrical switching only a small fraction of the domains can be switched. The lack of such techniques,

therefore, limits the study of the collinear AFMs especially from the point of view of dynamic studies. Thereby, the methods of a selective control of the Néel vector (writing) will not only be useful for storing the data but will also open new horizons for fundamental research.

While the study of an optical switching of ferro- and ferrimagnets does not give a clear answer to the underlying mechanism of the switching, one can use the similar approach to find ways for reliable switching. Namely, there are two major components of the switching: torque (induced anisotropy) and thermal activation.

Here, ultra-short laser pulses can be a source of thermal activation enabling a selective switching of the Néel vector with a spatial resolution limited by the optics. The missing part of the puzzle is the source of the magnetic torque.

3.2.1 STRAIN AS A DRIVING FORCE OF THE NÉEL VECTOR ALIGNMENT

Sometimes it happens that some small inconsistency of experimental data with the theory can give rise to a new idea for a breakthrough even in the simplest experiment. Taking a closer look at the experimental data, presented in chapter 2, one can notice that there is a slight asymmetry in the dichroism signal for magnetically aligned samples in comparison with the signal from the as-prepared sample. One of the possible explanations of this asymmetry is a partial alignment of the as-prepared sample (i.e. there are more domains with the Néel vector along $[110]$ than along $[1\bar{1}0]$). Indeed this fact is confirmed by another experimental technique reported in Ref. [55]. This slight polarization of the as-prepared sample can be explained by a built-in epitaxial strain generated, due to the particular growth conditions using r-cut Al_2O_3 substrate. It turns out that this built-in strain is too small to be detected with the XRD technique but large enough to induce a slight polarization of the as-prepared film. Thus, this indicates that the mechanical strain can be used for an efficient mechanism for the manipulation of the Néel vector orientation.

Following the general symmetry considerations, mechanical strain applied along one of the easy axes can break the four-fold symmetry of the Néel vector making one direction

energetically preferable. It was shown that the mechanical strain can modify the magnetic order of an AFM but the switching of the Néel vector was never achieved (i.e. once the stress was released, the system returned to the same state), meaning that the applied strain was not large enough to switch the Néel vector [48]. The applied strain is limited by the flexural strength of the substrate.

However, combining mechanical strain with thermal activation can be an efficient way to selectively manipulate the Néel vector in the collinear AFM Mn_2Au .

3.2.2 EXPERIMENTAL APPROACH

In order to test this hypothesis, the following experiment was performed: Several areas of the Mn_2Au thin film were irradiated with ultra-short laser pulses at different strain condition, varying the irradiation fluence. Afterwards, the magnetic order of the irradiated areas was examined with XMLD-PEEM imaging, described in the previous section. A 45 nm thick Mn_2Au film was grown following the recipe described in section 1.2.6 [45]. An array of gold markers was fabricated on top of the film with electron beam lithography (EBL) in order to enable navigation through the sample, both during the irradiation and imaging. As a result, 15 marked areas with a size of the $100 \times 100 \mu m$ where on the same film. The first five areas were irradiated without applying external mechanical strain. The second row of the areas was irradiated with the external mechanical tensile strain along the [110] crystallographic direction. The last 5 areas were irradiated under the tensile strain along the $[1\bar{1}0]$ direction.

The mechanical strain was generated by a special device similarly as in Ref. [48]. There, the sides of the sample are fixed and the eccentric axis is pushing the center of the substrate up, generating a tensile strain of the order of 10^{-3} . In our case we estimate strain to be $\simeq 6 \times 10^{-4}$.

Finally, 800 nm 60 fs pulsed laser beam was focused on the sample with the 50 mm lens, resulting in a beam spot of $22.5 \mu m$. For every strain condition, the sample was irradiated with 5 different fluences: 3.5, 5.3, 7.1, 8.9, 10.6 mJ/cm². Every area was irradiated for a

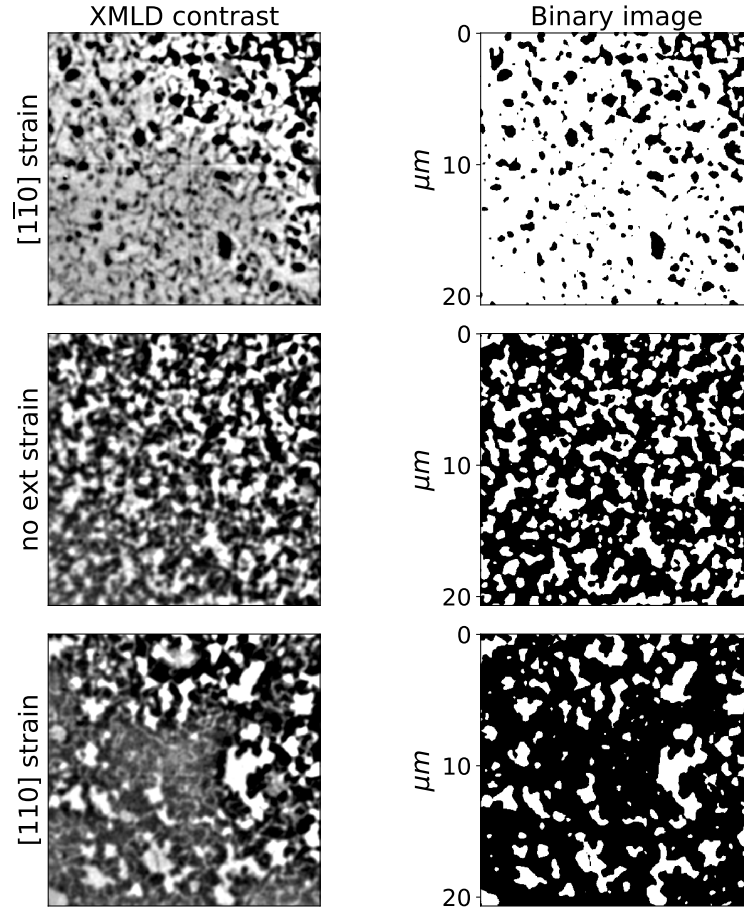


Figure 3.7: [XMLD-PEEM](#) images of the imaged areas and the corresponding processed binary images obtained by applying Otsu threshold. The images in the central row were obtained on the irradiated areas without external strain. The top and the bottom row show the areas irradiated with the strain along the $[1\bar{1}0]$ and $[110]$ directions, respectively.

few seconds while scanning the beam within a few tens of micrometers. Afterwards, the irradiated areas were imaged using [XMLD-PEEM](#) technique. Additionally, a few non-irradiated areas were imaged in order to calibrate the initial state of the sample. Examples of the recorded [XMLD-PEEM](#) images are shown in Fig. 3.7.

In order to quantify the degree of magnetic alignment, the [XMLD-PEEM](#) images were binarised using Otsu threshold [63]. The fraction of the white areas (areas where the Néel

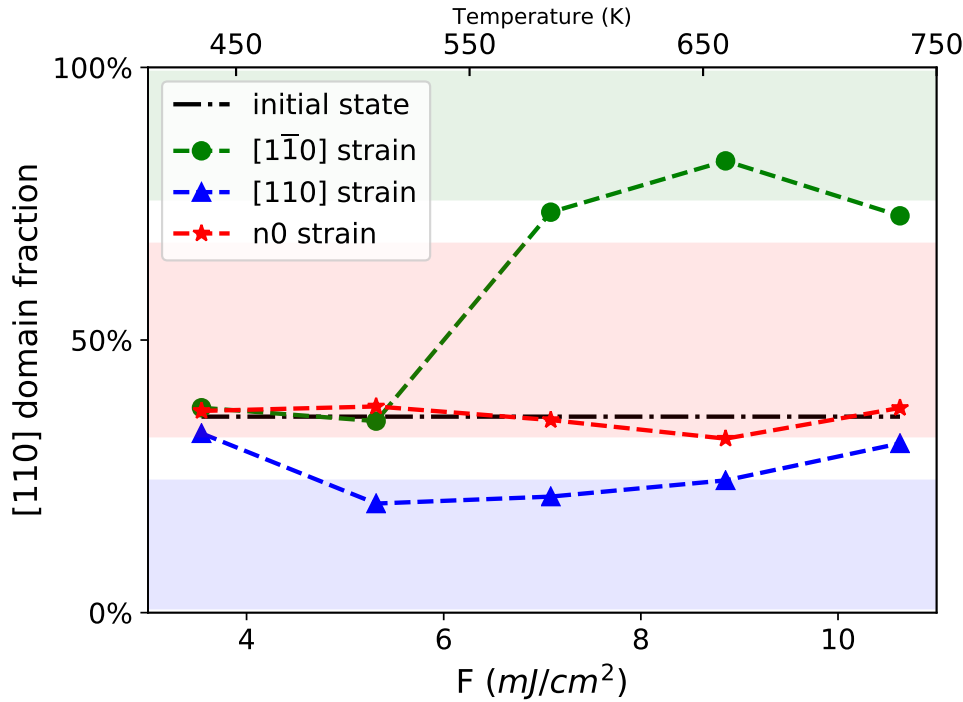


Figure 3.8: Dependence of the degree of polarization on the excitation fluence and strain along $[110]$ (green circles) and $[1\bar{1}0]$ (blue triangles) easy axes. Red stars show the evolution of the domain distribution within the areas irradiated without external strain. The black dashed line shows the initial state extracted from the images of the non-irradiated areas.

vector is aligned along the $[110]$ direction) is considered as the fraction of one type of AFM domains.

3.2.3 RESULTS

The final magnetic states of the irradiated areas are shown in Fig. 3.8 as a function of the irradiation fluence for the three different strain conditions. In the presence of the external strain, the polarization of Mn_2Au changes dramatically after a certain fluence. The switched regions consist of mostly one type of the domains, similar to the B-field aligned samples presented in chapter 2. Furthermore, the threshold fluence appears to be different for the

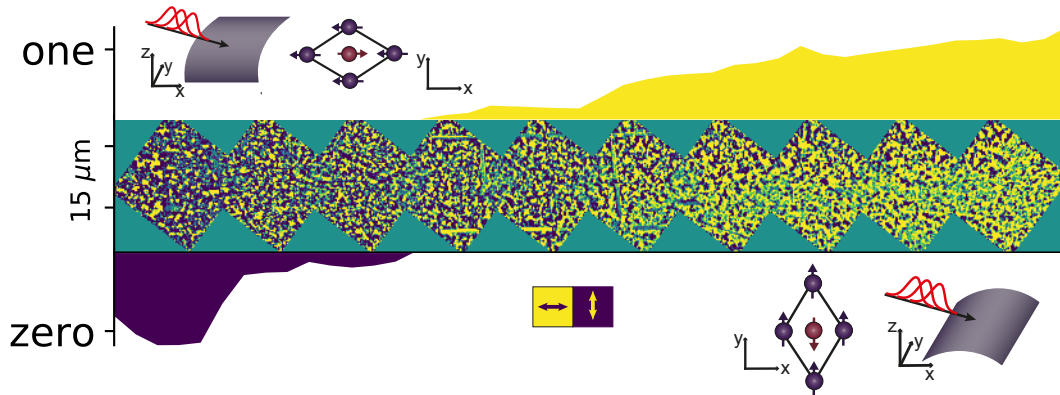


Figure 3.9: XMLD contrast variation along the sample from irradiated area with strain along $[110]$ to another areas with strain $[1\bar{1}0]$. On the left side is the area irradiated with the external strain along $[110]$, while the right side was irradiated with external strain along $[1\bar{1}0]$. The top and the bottom colored graphs indicate the domain distribution averaged along the vertical direction for the stripe $5 \mu\text{m}$ wide. The domain distribution shows the “zero” and “one” states recorded this way on one film.

two orthogonal directions of the external strain. In the case of the external strain applied along the $[1\bar{1}0]$ direction, the switching is observed already at $5.3 \text{ mJ}/\text{cm}^2$, while in the opposite case, the switching is detected only at $7.1 \text{ mJ}/\text{cm}^2$. Such a difference can be explained by taking into account the built-in epitaxial strain. Indeed, the original state has less than 50% of $[110]$ domains. Thus, the built-in strain should be added to the external strain applied the $[110]$ direction and subtracted from the strain along $[1\bar{1}0]$ to calculate the total strain.

Figure 3.9 shows a set of XMLD-PEEM images successively acquired with a lateral offset of $15 \mu\text{m}$, thus, covering two neighbouring areas irradiated with the same fluence but the opposite strain directions. The orientation of the strain and the induced deformations of the crystal lattice are also schematically illustrated. On the left hand side, the domain structure exhibits preferentially dark domains, while the rightmost images have clearly more bright

domains. In between, one can see a continuous variation in the AFM domain structure from the area irradiated with the strain applied along the $[110]$ direction (left hand side), towards the area irradiated with the strain along the $[1\bar{1}0]$ direction (right hand side). A substantial area between the irradiated areas was not irradiated.

To qualitatively illustrate the observed variation, we plot the XMLD contrast, averaged over a vertical stripe with $5 \mu\text{m}$ width as the colored filled graphs. Indeed, there is an unambiguous trend from the state with one preferred orientation of the Néel vector (state “zero”) towards the orthogonal Néel vector orientation (state “one”).

3.2.4 ESTIMATES OF LASER HEATING EFFECTS

When irradiating the sample with a femtosecond laser beam there are several heating effects to be considered. The first is the continuous sample heating, which is proportional to the average irradiation intensity. The continuous laser heating in a thin film is governed by the absorbed light intensity and the thermal properties of the substrate. The temperature increase of the illuminated region can be estimated using a simple steady-state heat diffusion model [64, 65]. Using the reflectivity of 0.52 and the thermal conductivity, κ , of sapphire at room temperature of 35 W/mK [66] we estimate the steady state heating to be $< 6 \text{ K}$ over the entire range of fluences used in this experiment. Thus, the continuous laser heating effects can be neglected.

To estimate transient laser heating in a metallic sample, two effects can be considered. On a femtosecond timescale, the rapid electron-electron thermalization leads to a rapid thermalization of the electron gas. Here, assuming no heat transfer to the lattice, the resulting electronic temperature can be estimated considering the absorbed energy per pulse and the electronic specific heat. Considering the calculated electronic density of states in Mn_2Au [20] and the Sommerfeld model for the specific heat we obtain the resulting electronic temperatures between 3800 and 6700 K for excitation densities between 4.2 and 12.6 mJ/cm^2 . While the optical penetration depth of Mn_2Au is estimated to be approximately 30 nm , we

assume that the hot electron transport results in a homogeneous electronic temperature throughout the film/buffer layer thickness.

On the timescale of a few picoseconds, the electrons thermalize with the lattice, resulting in a temperature that is governed by the total specific heat of the metallic layer [67]. Under these assumptions, the temperature increase, ΔT , is estimated from the absorbed energy density:

$$\Delta T = \frac{F(1 - R - T)}{C_p^{Mn_2Au} * d_{Mn_2Au} + C_p^{Ta} * d_{Ta}}.$$

Here, $R \approx 0.52$ is the reflectivity [52], $T \approx 0.03$ is the transmission, d_{Mn_2Au} , d_{Ta} are the thicknesses and $C_p^{Mn_2Au}$, C_p^{Ta} are the total specific heats of the corresponding metallic layers. As at temperatures above 300 K the lattice specific heat dominates, we use the Dulong-Petit limit. The resulting temperatures as a function of irradiation fluence F are presented in Fig. 3.8. Note that the subsequent cooling of the excited sample volume is governed by the heat diffusion into the substrate, governed by the substrate's thermal conductivity, κ . To estimate the evolution of temperature we use a simple heat diffusion model for a semi-infinite solid [65]:

$$\begin{aligned} \Delta T(\vec{r}, t) = & \frac{P_0 \alpha (1 - R)}{4\pi \rho_s c} e^{-\alpha z} \\ & \times \int_{-\infty}^t dt' \frac{\exp\left(-\frac{2t'^2}{\tau^2} + \alpha^2 d_i (t - t') - \frac{x^2}{4(t-t')d_i + d^2} - \frac{y^2}{4(t-t')d_i + d^2}\right)}{\sqrt{4(t-t')d_i + d^2} + \sqrt{4(t-t')d_i}} \\ & \times \left[1 + \operatorname{erf}\left(\frac{2z - 4\alpha d_i (t - t')}{4\sqrt{(t-t')d_i}}\right) + e^{2\alpha z} \left(1 - \operatorname{erf}\left(\frac{2z + 4\alpha d_i (t - t')}{4\sqrt{(t-t')d_i}}\right)\right)\right], \end{aligned} \quad (3.1)$$

Here $d_i = \kappa/\rho_s c$ is the thermal diffusivity, ρ_s is the density of sapphire, α is the absorption coefficient and $\operatorname{erf}(x) = \int_0^x \exp(-t^2) dt$.

It follows from Fig. 3.10 that the characteristic time, at which ΔT drops to one half of its peak value is of the order of 100 ps.

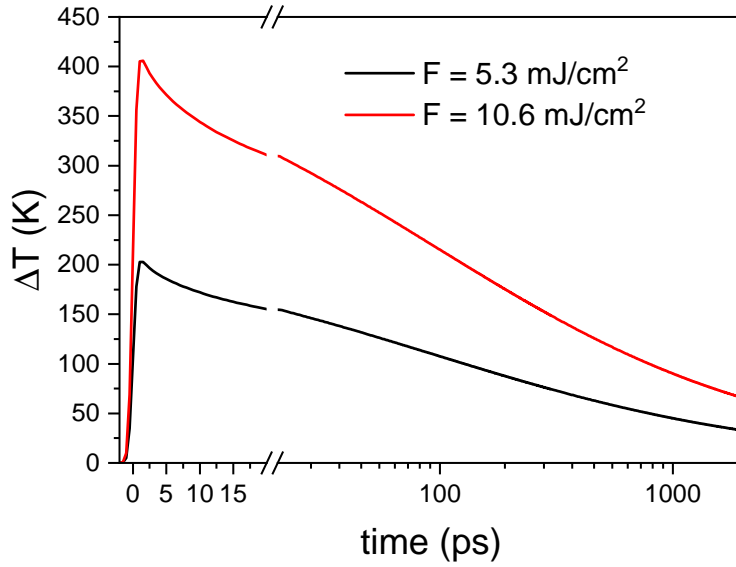


Figure 3.10: Simulated temporal evolution of temperature of the irradiated spot for two characteristic excitation fluences. Time evolution of the temperature change of the film is calculated for two characteristic excitation fluences using a simple heat diffusion model [65], given by Eq. 3.1. Note there is an axis break at 20 ps, accompanied by the change in scale from linear to semi-logarithmic.

3.2.5 FREE ENERGY LANDSCAPE IN A STRAINED EASY-PLANE AFM

The relevant components of the free energy functional are the magneto-crystalline anisotropy energy, E_{anis} , and the magnetostriction, E_{ms} , and could be written as follows:

$$E = E_{anis} + E_{ms}. \quad (3.2)$$

For a tetragonal material, the anisotropy energy is given by:

$$E_{anis} = K_{2\perp} \cos^2(\Theta) + K_{4\perp} \cos^4(\Theta) + K_{4\parallel} \sin^4(\Theta) \cos(4\phi), \quad (3.3)$$

where Θ and ϕ are the axial and polar angles of the corresponding spin, $K_{2\perp}$ and $K_{4\perp}$ are out-of-plane and $K_{4\parallel}$ in-plane magnetocrystalline anisotropy constants. For the case of an

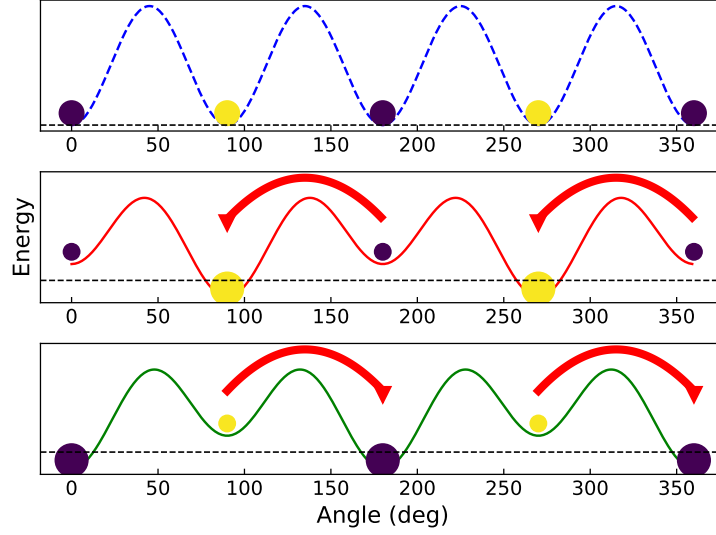


Figure 3.11: The top panel shows the equilibrium energy landscape, indicating the four-fold symmetry for the Néel vector. Dots of the same size indicate the equal distribution of the two type of AFM domains with the Néel vector along the $[110]$ or $[1\bar{1}0]$ directions. The center panel shows the energy landscape modified by the applied strain. The bottom panel shows the energy landscape modified by the strain applied along the $[110]$ direction. If one would consider coherent domain switching mechanism of Ref. [68] the effect of thermally activated switching would be represented by red arrows in the bottom panel.

easy plane AFM, E_{anis} reduces to:

$$E_{anis} = K_{4||} \sin^4(\Theta) \cos(4\phi). \quad (3.4)$$

For Mn_2Au , $K_{4||}$ was measured to be $1.8 \mu\text{eV}$ per formula unit [55].

The magnetostriction energy E_{ms} is given by

$$E_{ms} = B_{ij} \epsilon_{ij} \beta_i \beta_j, \quad (3.5)$$

where β_{ij} are the directional cosines. In case of unidirectional strain, the strain tensor has only one component, ϵ_{xx} . Thus,

$$E_{ms} = B \epsilon_{xx} \cos^2(\phi). \quad (3.6)$$

In the absence of strain, the free energy exhibits a four-fold symmetry, which should result in equal distribution of the $[110]$ and $[1\bar{1}0]$ domains. As illustrated in Fig. 3.11, under the external unidirectional strain, the free energy landscape is modified such, that the local minima for the $[110]$ and $[1\bar{1}0]$ domains become non-degenerate. Using DFT calculations we estimate $B = 1.3$ meV per formula unit, resulting in $B\epsilon_{xx} = 0.8$ μ eV per formula unit, which is comparable to $K_{4||}$. Moreover, given the weak in-plane anisotropy in Mn_2Au , even a weak growth-induced strain can lead to an imbalance between the volume fractions of the two types of domain in the as-grown sample, as experimentally observed.

3.2.6 COHERENT SWITCHING OF THE AFM DOMAINS

For the discussion of possible switching mechanisms we start with an overview of the macroscopic model presented in Ref. [68], developed for the description of the role of thermal activation in current induced switching of Mn_2Au . The model considers the coherent switching of the AFM domains within the framework of the Arrhenius model. The switching probability for an AFM domain is given by the Poisson distribution $P_{SW}(\delta t) = 1 - \exp\left(-\frac{\delta t}{\tau}\right)$, where δt is the time during which the sample is hot. The switching rate $1/\tau$ is given by the Néel-Arrhenius equation:

$$\frac{1}{\tau} = f_0 \exp\left(-\frac{E_b}{k_b T}\right). \quad (3.7)$$

Here, k_b is a Boltzmann constant and the attempt frequency f_0 is defined by the AFM dynamics, which is expected to be in THz range. E_b is the energy barrier between two local energy minima, which correspond to the two orientation of the Néel vector, and is defined by the anisotropy energy $K_{4||}$ per unit cell. In the presence of the NSOT (considering current induced switching) one of the two Néel vector orientations has a lower energy, making one type of the domains energetically favorable. In our case, mechanical strain plays the same role (Fig. 3.11). In this model, E_b was calculated for the volume of a stable magnetic structure, i.e. domain. Following this scenario, one can assume that the energy barrier

should be defined by the anisotropy energy calculated for one domain. Taking into account the volume of one domain ($20 \text{ nm} \times 20 \text{ nm} \times 20 \text{ nm}$), which was experimentally defined in Ref. [68] based on the grain size of the film and anisotropy energy of $K_{4||} = 1.8 \text{ } \mu\text{eV}$ per formula unit [55] or $3.6 \text{ } \mu\text{eV}$ per u.c., one obtains an energy barrier $E_b = 1.5 \text{ eV}$. Using 1.5 eV the authors got a good agreement of their model simulations with experiment. However, in our case the domain size is approximately $1 \text{ } \mu\text{m} \times 1 \text{ } \mu\text{m} \times 45 \text{ nm}$, so $E_b = 10^4 \text{ eV}$. Since $E_b \gg k_b T$ for all irradiation fluences, the probability of coherent switching of the domain should remain zero. Thus, this model can not be applied to our experimental results.

We note that the fraction of the switched domains, i.e. the amplitude of the switching in the model [68], is defined by the time δt during which the sample stays hot within the duration of the current pulse. This, however, can not be applied to our data, since we irradiated each area with a large number of pulses, hence, δt can be considered infinite. Within this model, even a comparably weak irradiation should slightly change the ratio between the two volume fractions. However, we clearly observe a threshold behaviour for the switching, see Fig. 3.8, which implies that the sample polarizes to the maximum polarization as soon as the transient heating temperature reaches the threshold temperature.

3.2.7 THERMALLY ACTIVATED DOMAIN WALL MOTION

Thinking of the possible scenario of the observed switching one can imagine two cases. Coherent switching of the domains (as discussed in section 3.2.6) or growth of the energetically favorable domains. In the first case, ultra-fast suppression of the order parameter (Néel vector) of Mn_2Au followed by reconstruction of the magnetic state should lead to a new polarized state. Such a scenario requires the transient temperature of the sample to be close to the Néel temperature, for the magnetic order to become unstable. However, the experimentally achieved temperatures are much lower than $T_N \approx 1500 \text{ K}$. On the other hand, the order parameter can be strongly suppressed during optical excitation also due to the large SOC. (However, no estimates on the strength of optical suppression of the order parameter

exist up to date).

In order to clarify the underlying pathway of the switching process, the sample was imaged before and after irradiation. In this experiment, the B-field aligned sample was irradiated without external strain. Hence, the polarized sample has to switch to its new equilibrium magnetic state. Here, the sample was originally aligned in the less favorable direction considering the built-in epitaxial strain. The fluence was at the threshold fluence of switching in this case $F_{th} \approx 11.5 \frac{mJ}{cm^2}$. In the case of coherent domain switching, one expects to see a completely different domain pattern after switching or the same domain structure with some domains being switched. However, it turns out that the domain structure remains quite similar and only some of the domains grow in size. In Fig. 3.12, the magnetic contrast before and after the switching is shown. The regions, where the domain growth is obvious, are marked by circles.

The schematic of the domain wall (DW) is depicted in the right panel in Fig. 3.12. There are in general two types of the DWs: 90° is a DW between two domains with the orthogonally aligned Néel vectors and a 180° DW, which is a border between two domains, where the Néel vectors are aligned antiparallel. In the case of a 90° DW, the external strain will induce the free energy gradient and thus force the DW to move, while a 180° domain wall is stable against strain. The presence of 180° DWs in the polarized areas of the sample implies simultaneous growth of the domains aligned antiparallel, i.e. the domain wall motion mechanism being responsible for alignment of the Néel vector under optical excitation and external strain, because in the case of the coherent switching one would expect to end in a single domain state.

The logical question arises: “*Why is the domain structure stable after applying strain without optical excitation*”? We can imagine that the DWs are pinned at pinning centers, such as crystalline defects, dislocations or disclinations. The threshold temperature should thus be related to the pinning energy of the domain wall. Thus, the laser pulse likely depins

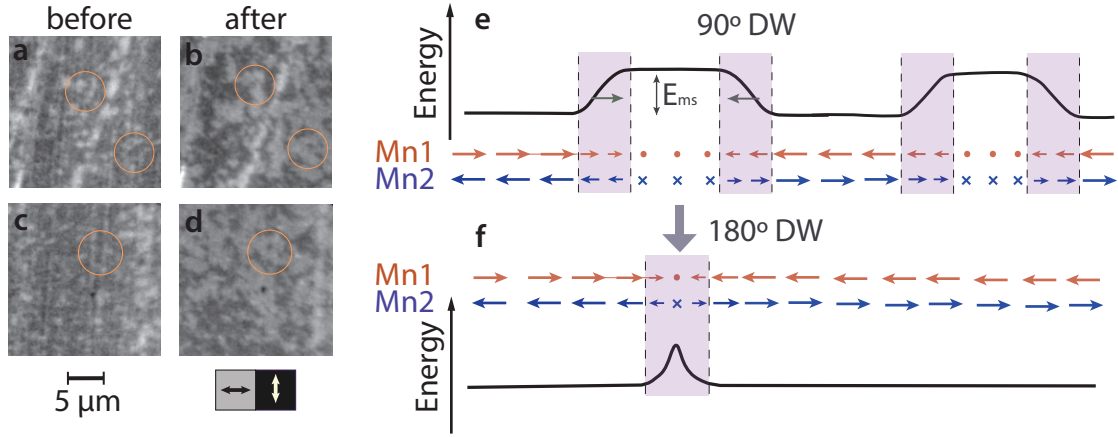


Figure 3.12: XMLD-PEEM images of a Mn₂Au film Néel vector aligned in 60 T magnetic field along the [110] direction recorded before (a) and (c) and after (b) and (d) irradiation by the train of NIR pulses. The sample was irradiated with the excitation fluence of 11.5 mJ/cm² in the absence of external strain. The highlighted regions demonstrate the growth of the domains aligned along the [1̄10] direction, which is the direction preferred by the growth-induced strain. Schematic of the variation of the free energy density under tensile strain, showing the direction of motion of 90° DWs upon light-induced depinning (e), while 180° worm-like domain walls (f) are unaffected.

the DW, which moves in the direction of the free energy gradient (force).

Other indirect evidence of this mechanism are the presence of the large white domains in the “black” areas (Fig. 3.7) and the observation of a trend towards the equal distribution of the domains in the areas irradiated with the highest irradiation fluence in the presence of the external strain along [110] (Fig. 3.8). We note, that the order of the irradiation experiments may play a role. Firstly, the 5 areas were irradiated with the strain applied along [110] direction and after that, another 5 areas were irradiated with the perpendicular strain. In this case, if a 180° DW in the areas irradiated first, are found at an unstable position, i.e. not pinned, the 180° DW could expand into a domain with orthogonal Néel vector orientation

under strain even without thermal activation, as discussed below.

To sketch the idea, we can look at the domains in 1D, as depicted in Fig. 3.12, considering a domain being surrounded by two 90° DWs. Before irradiation both of the DWs are pinned to the pinning centers. Assuming that the pinning centers are different and the pinning energies of the two DWs differ from each other, one can consider two possibilities. If the irradiation fluence is just enough to depin only one DW, it will propagate to the opposite one and form a 180° DW at a stable place (the 180° DW can be viewed as a pair of 90° DWs). In this case, the 180° DW will be pinned at the same pinning center as the 90° DW with a higher pinning energy. For higher irradiation fluence, both DWs become depinned and the resulting 180° DW can be stabilized somewhere in between the original positions of the 90° DWs, potentially at the position where pinning is not so strong. Such a 180° DW may be unstable and eventually expand into a domain as soon as the strain direction is reversed. In this scenario, higher excitation fluence increases the possibility of the formation of lightly pinned 180° DW, thus a magnetically polarized state will be unstable against the strain during further manipulations. We note that such an explanation is purely hypothetical and requires additional experiments to be confirmed or rejected.

3.2.8 CONCLUSION

In this chapter, we present a simple table-top method for efficient manipulation of the Néel vector orientation in an AFM thin film, with the spatial resolution in principle limited by the wavelength of light. Such a method opens up new opportunities in the field of spintronics, especially for testing potential read-out techniques. The presented approach is the first to allow selective/local control of the Néel vector orientation, which in turn, enables reliable generation of AFM DWs for experimental studies of their properties and to optimize their performance for spintronic devices.

Moreover, thermally activated switching mechanism implies that a variety of the heat sources may be used, from high frequency light to local currents, allowing to increase writing

density up to fundamental limits of [AFM](#). While the presented data do not provide clear answers about the speed and energy efficiency of the writing process, Mn_2Au thin films can already be used as a long-term data storage device.

Finally, since the [DW](#) motion can be triggered with optical pulses, the dynamical study could be performed, which is discussed in the next chapter.

Pump-probe study of the metallic collinear AFM Mn_2Au

In this chapter, we combine the knowledge acquired in the previous two chapters. Here, in the first part, the results of optical pump-probe studies are discussed. In the second part, the concept of the experiment to detect the domain wall motion dynamics is proposed.

4.1 TIME-RESOLVED MLD IN Mn_2Au

As shown in chapter 2, the magnetic order (Néel vector) can be detected with optics. In reflection geometry, with a finite angle of incidence, there are two contributions to the MO effect that can be measured in Mn_2Au thin film: isotropic and anisotropic. The anisotropic effect is sensitive to the relative orientation of the light polarization and the Néel vector, while the isotropic is Néel vector orientation independent and appears always, when there is a projection of the light polarization on the four-fold symmetry axis. Naturally, the MLD will result in the rotation of the polarization of the reflected light. Hence, by measuring the evolution of the polarization rotation of the reflected light one may expect two contributions

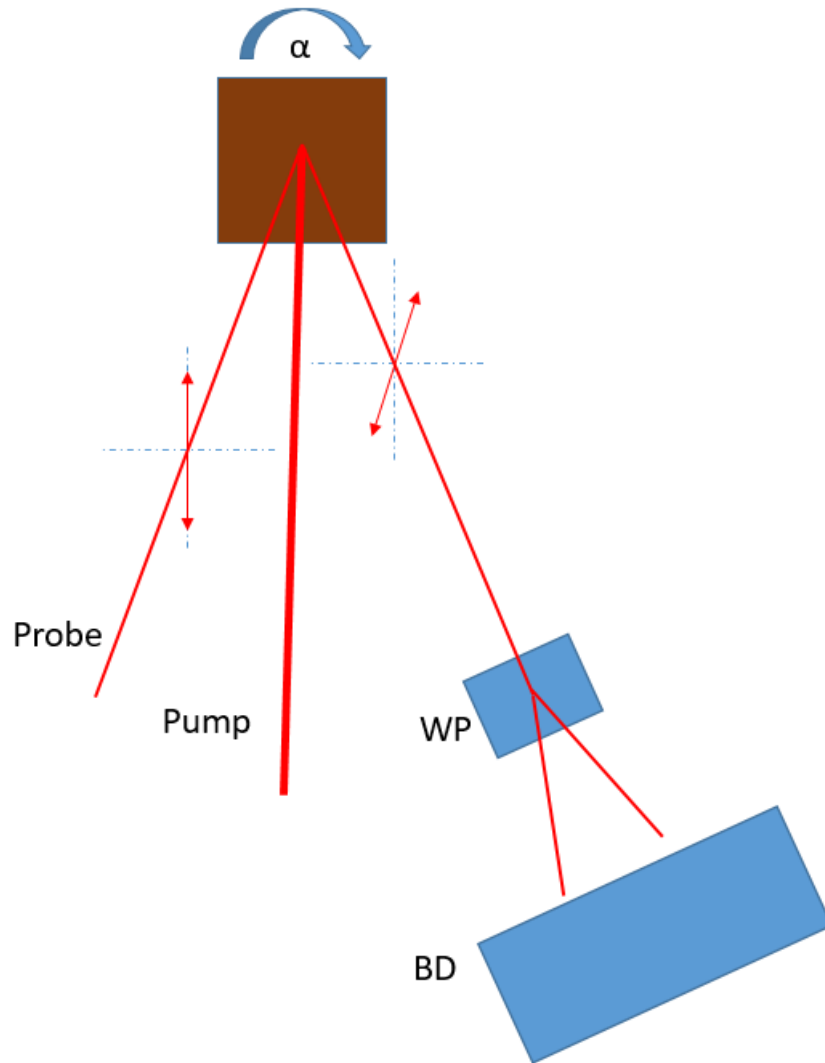


Figure 4.1: Detection scheme of the pump-induced polarization rotation using a balance detector (BD). The reflected beam is split using a Wollaston prism (WP).

to the pump-probe signal, which is measuring changes in the polarization as a function of time after photoexcitation with pump pulse.

In order to distinguish the two contributions, measurements should be performed as a function of the relative orientation between the incoming light polarization and the Néel vector. To do so, a pump-probe experiment was performed by rotating the sample around the c -axis. The experiment was done on a magnetically aligned Mn₂Au thin film, ensuring

that there was only one type of AFM domains in the probed area defined by the probe spot size.

The probe pulse was linearly polarized and after being reflected from the sample, the polarization rotation was detected with a balanced detector as shown in Fig. 4.1. The angular dependence of the pump-induced polarization rotation is shown in Fig. 4.2. During the measurements, the probe beam was focused down to $50 \mu\text{m}$, while the pump pulse was about $70 \mu\text{m}$. The probe fluence was $10 \mu\text{J}/\text{cm}^2$ and the pump fluence was $600 \mu\text{J}/\text{cm}^2$. Both were linearly polarized.

Here, one can attribute the signal, averaged over the relative angle between probe polarization and the Néel vector, to the evolution of the isotropic component of the pump-induced polarization rotation. By subtracting the average signal from the trace measured at each angle, the evolution of the anisotropic component can be obtained. In this case, the light-induced dynamics of the anisotropic component should exhibit a two-fold symmetry, i.e. the signal should be the same for α and $\alpha + 180^\circ$.

Indeed, as shown in Fig. 4.2, the pump-induced polarization rotation signal has an angular dependence with two-fold symmetry and can be attributed to the dynamics of the anisotropic component of the MO effect. The dynamics may be a result of the pump-induced suppression and recovery of the order parameter, i.e. the Néel vector. The average over the angle signal has a rise time of 100 fs and the decay time of a few ps.

While above description may be correct, we note the possible problems with this interpretation. Such fast dynamics should be compared with the simple reflectivity dynamics. To do so, pump-probe reflectivity measurements were simultaneously performed. In Fig. 4.3, normalised transient reflectivity signal and polarization rotation are shown. The transient reflectivity normally indicates the dynamics of the electron-lattice thermalization. The pump-induced polarization rotation perfectly matches the reflectivity dynamics except for the first 100 fs. This observed spike at $t \approx 0$ in the signal is usually attributed to a

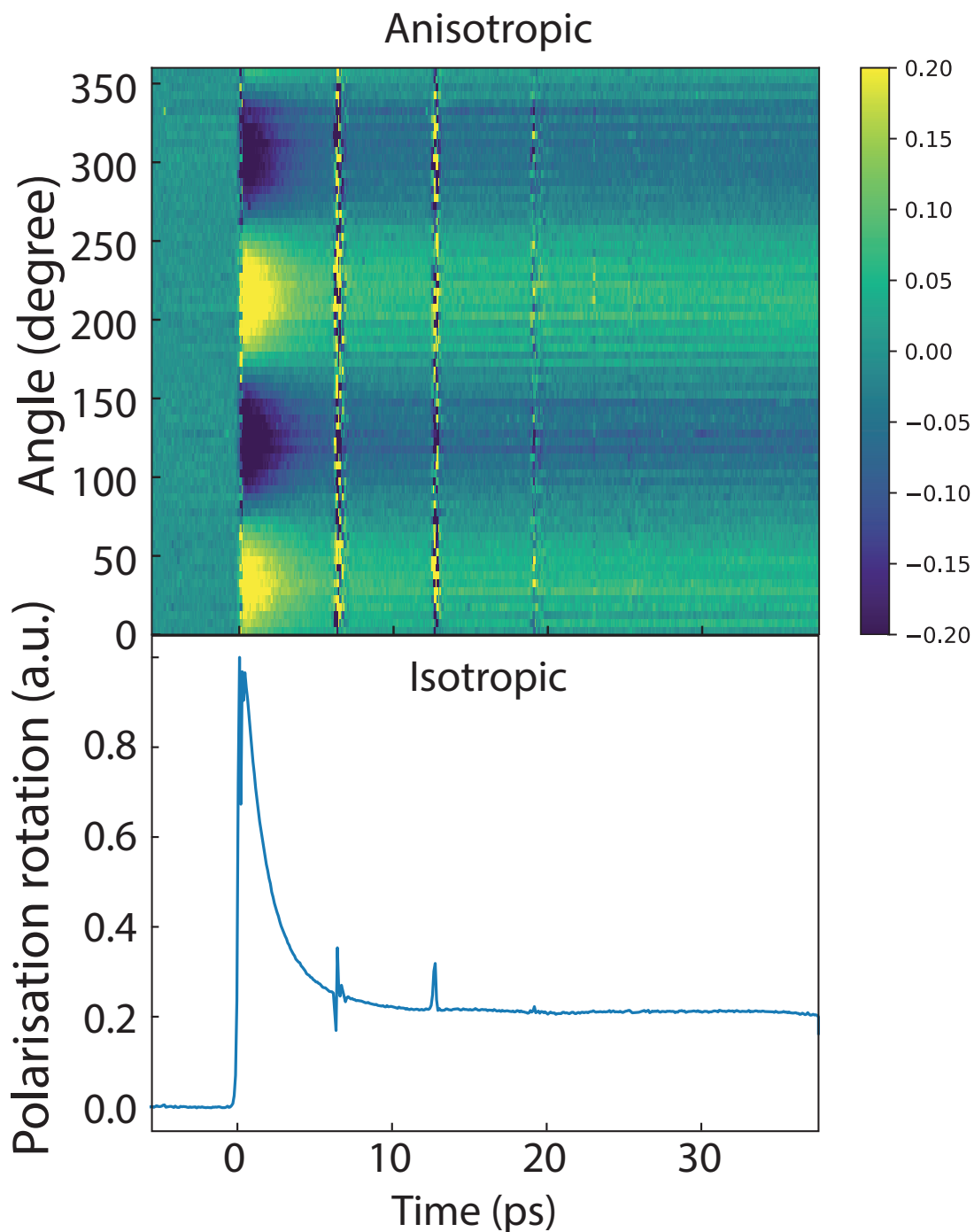


Figure 4.2: Angular dependent (top) and isotropic (bottom) pump-induced polarization rotation of Mn_2Au .

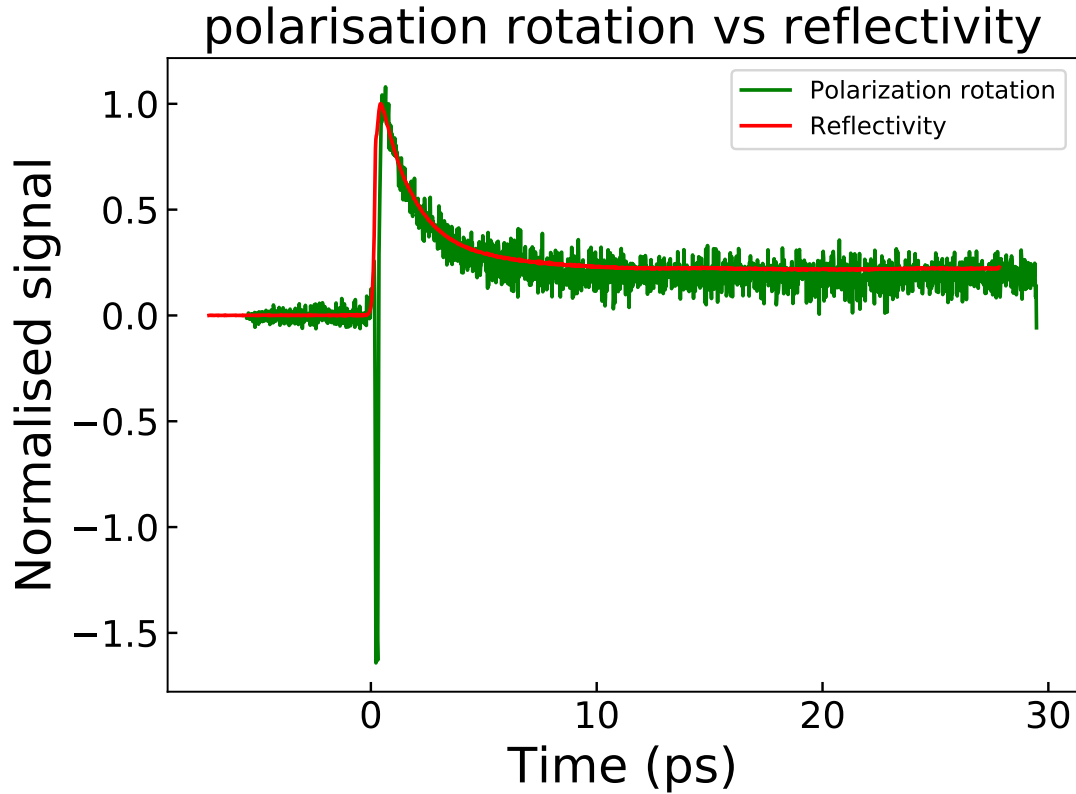


Figure 4.3: Comparison of the pump-induced polarization rotation and transient reflectivity measured for Mn_2Au thin film using the detection scheme in Fig. 4.1.

coherent artefact, due to the overlap of the pump and probe pulses in time. Such artefacts can be observed also on non-magnetic metallic samples while measuring time resolved MO effects [69].

We can speculate that in Mn_2Au , the match of the pump-induced polarization rotation and transient reflectivity indicates a strong coupling of the electronic and the magnetic order, thus resulting in the same dynamics. On the other hand, there are possible effects on the short time-scale like in Ref. [70], that can not be excluded in this case. In order to confirm the Néel vector suppression origin of the observed dynamics one could study the temperature dependence of the pump induced polarization rotation, reaching the Néel temperature, above which all the effects related to the magnetic order should vanish. However, the Néel

temperature of Mn₂Au is too high to be reached ($T_N \approx 1500$ K).

4.2 TOWARDS THE DYNAMICS OF STRAIN-INDUCED DOMAIN WALL MOTION

As discussed in chapter 3, the domain wall motion can be induced with an intense laser pulse in the presence of the mechanical strain. Additionally, the magnetic state of Mn₂Au can be measured using linear dichroism in NIR. Thus, the necessary requirements for the dynamical study are fulfilled. If one can realize a system which will induce mechanical strain in the film periodically, the dynamics of the domain walls motion could be measured in a pump-probe manner.

The idea of such experiment is the following: the mechanical stress should be applied to the sample at half the repetition rate of the laser. In this case, every even pump pulse will arrive at the sample when the tensile strain is applied and every odd pulse will arrive at the sample when the compressive strain is applied (see Fig. 4.4). Thereby, the domain walls will move back and forth leading to reversible changes of the magnetic structure.

To realise this scenario, one can design a mechanical device similar to that used in chapter 3, however it will not be able to operate at the desired frequencies. Moreover, the central region of the sample will move in space, which will have a negative effect on the data quality, due to the shift of the film from the focus of the beams. An alternative way is to generate the eigen-oscillations of the substrate. To do so, one needs to shake fixed edges of the substrate at the mechanical resonance frequencies of the substrate. The resonance frequency of Al₂O₃ substrate with the standard dimensions ($10 \times 10 \times 0.53$ mm³) is approximately 60-70 kHz (Fig. 4.5), which is compatible with the laser system used in this thesis. It can easily operate at the repetition rate of 140 kHz, twice the resonance frequency of the substrate.

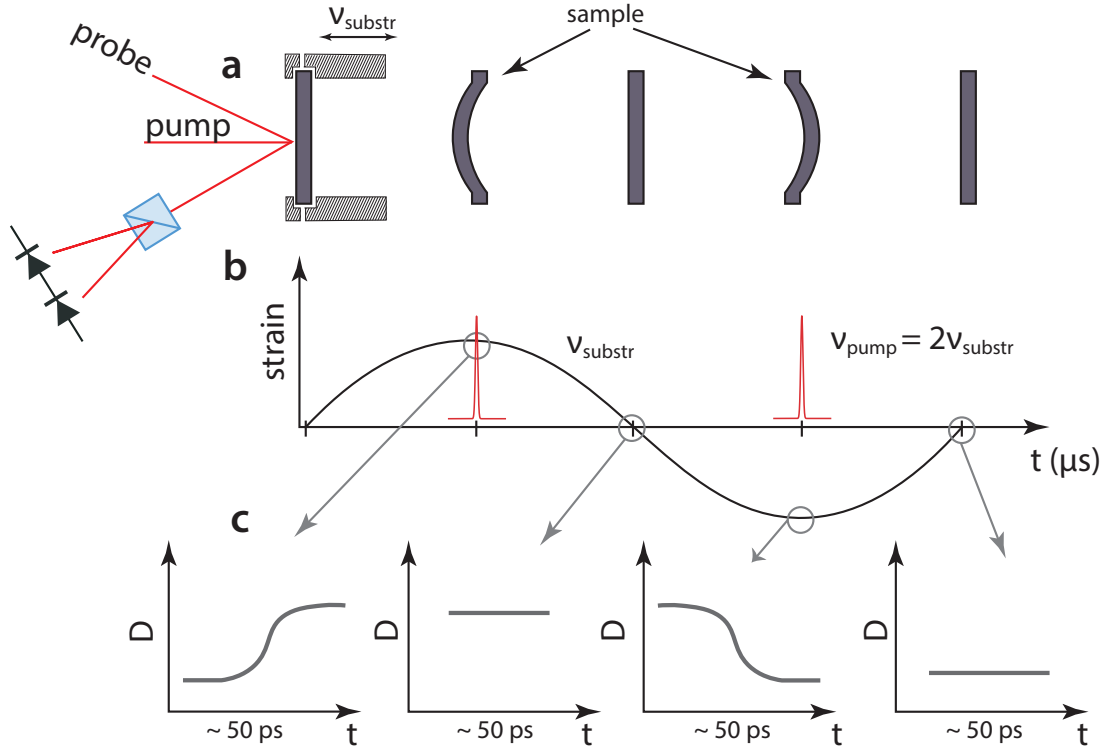


Figure 4.4: The proposed pump-probe experiment with sketched time evolution. (a) Substrate deformation due to the application of mechanical stress at half the frequency of the laser. (b) Every even (odd) pump pulse arrives at the sample when the tensile (compressive) strain is present. (c) The pump-induced switching dynamics/DW motion dynamics can be detected by the evolution of the measured transient polarization rotation.

The layout of the experiment is presented in Fig. 4.4. There, the edges of the substrate are clamped and the holder oscillate at the frequency which corresponds to the 1st eigenmode of the substrate. The first challenge is to find the resonance of the device with the used substrate. It is worth noting that with such an approach, the oscillating strain can be generated while the center of the substrate will not have lateral displacement and the focused laser beam will probe the same spot all the time. The laser must be synchronised with the vibrator and generates pump pulses when the strain has its maximum amplitude,

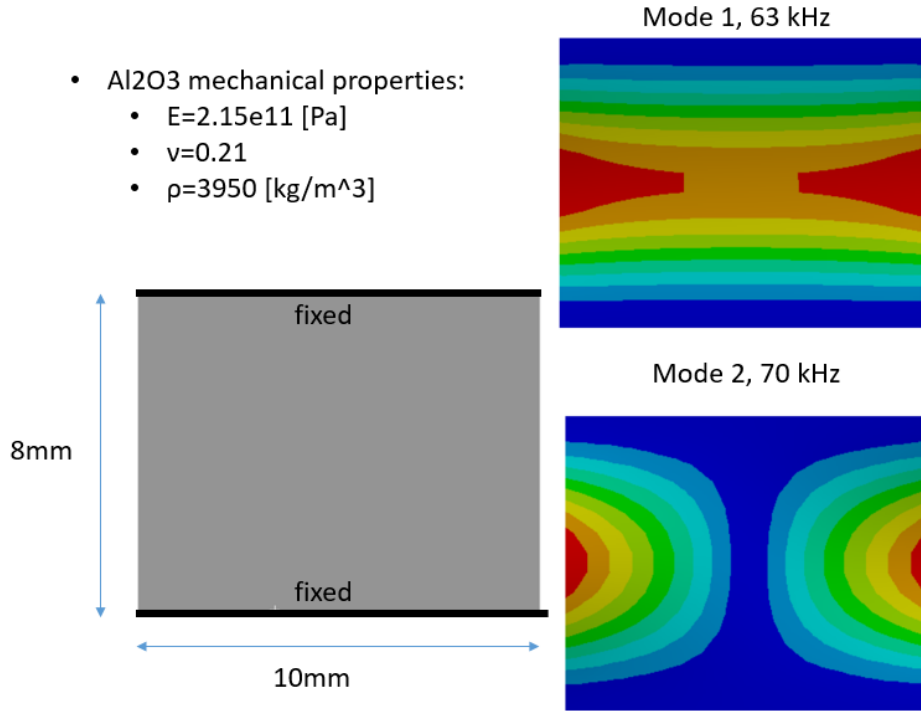


Figure 4.5: Eigen-modes of the sapphire substrate. The calculations is performed for $10 \times 8 \times 0.53$ mm³ Al₂O₃ substrate with fixed edges.

thus working at the double frequency of the mechanical oscillator.

By detecting the probe polarization dependence, one could record the switching dynamics/domain wall motion dynamics as shown in Fig. 4.4 (c). First of all, the changes of the magnetic structure can be detected at the equilibrium state when the strain is zero, in order to minimise geometrical effects(stress itself can affect the measured signal). In this case, the probe pulse should be delayed from the pump by $t = \frac{2}{\nu_{pump}} = 14 \mu s$, which corresponds to 4.2 kilometers of path. Anther way would be to run the laser at the frequency four times higher than the frequency of the substrate and cut out every second pump pulse, which needs more advanced timing electronics.

On the other hand, transient polarization rotation should be mirrored for the opposite strain condition and the switching can be detected directly at the extremum of the applied

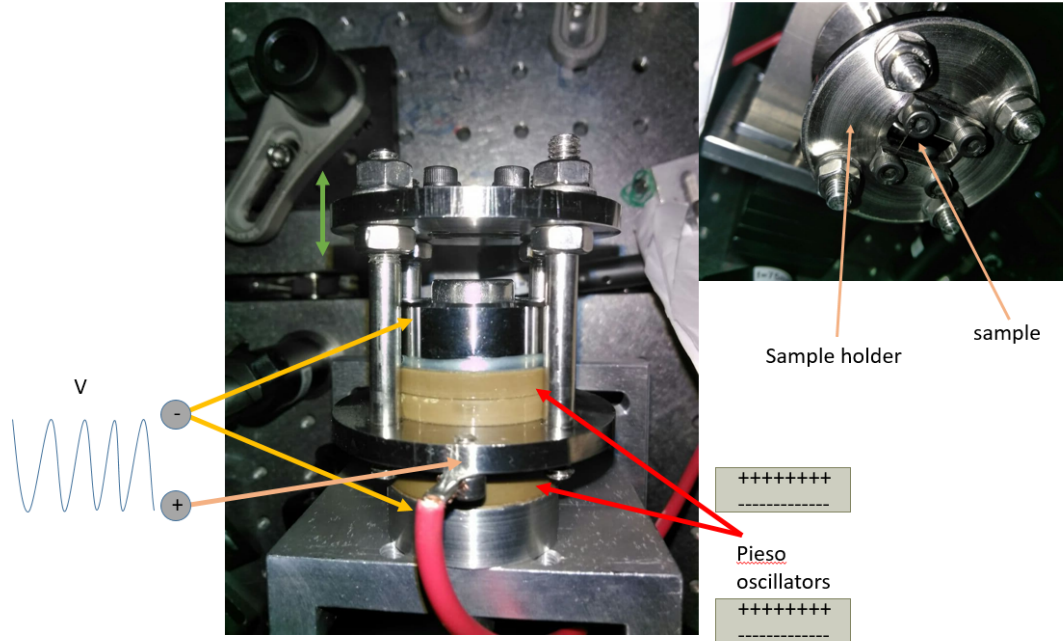


Figure 4.6: Prototype electro-mechanical device for the periodic strain generation.

strain. In this case, the acquired signal could be attributed to the domain wall motion if the rise time of the signal will scale linearly with the fluence, which should correspond to the final degree of polarization. Moreover, varying the phase between the laser pulses and the substrate oscillations, the strain dependence of the switching can be studied.

To perform the pilot test measurements, a mechanical device based on piezoelectric transducers was designed and produced. The photo of the device is shown in Fig. 4.6. There, two piezoelectric crystals clamp the round metallic plate, which is connected to the sample holder via four studs. Polarity of the piezoelectric transducers is inverted, meaning that the round plate between them is the “plus” for one of them and “minus” for the other. Thus, by applying a sinusoidal voltage to the plate, the two transducers will move with a phase shift of 90° degrees, making the plate oscillate.

While the deformation of the substrate was detected at the frequency of 74 kHz, the expected dynamics was not observed. The reason for this most likely stems from too small

amplitude of the device. Quick measurements show that the amplitude of the oscillation is less than 1 μm , hence the generated strain is at least 20 times less than that used in chapter 3, which is definitely not enough to compensate the built-in strain.

In order to perform the proposed experiment one needs to redesign the device with more powerful piezoelectric oscillators, to reach the amplitude of vibration of the order of 10 μm . On the other hand, such schematic can work for Mn_2Au grown on a symmetric substrate like MgO where the built-in strain should be absent. In this case, even a smaller strain modulation is expected to make the laser-induced domain wall motion reversible. This will be the topic of further research.

Conclusion

In this thesis, the interaction of light with metallic collinear AFM Mn₂Au is studied, in order to demonstrate the proof-of-principle optical read-out of the Néel vector and its manipulation with optical pulses.

It is experimentally demonstrated, that the orientation of the Néel vector in Mn₂Au thin films can be detected with a simple optical setup. Based on the referenced measurements, it becomes possible to disentangle the MLD effect from the structural contribution to the reflectivity asymmetry. The resulting MLD related to the orientation of the Néel vector is found to be 0.6% and can be used for detection of the orientation of the Néel vector, i.e. read-out of recorded data. From the asymmetry of the MLD signal for two orthogonal Néel vector orientations in comparison with the as-prepared sample, we concluded that even a slight mechanical strain, caused by the substrate asymmetry, can shift the ratio of the two type of AFM domains in Mn₂Au, due to the presence of magnetoelasticity.

Using direct XMLD-PEEM imaging, the manipulation of the Néel vector with optical pulses and mechanical strain is demonstrated. Using external mechanical strain to break the four-fold symmetry of the Néel vector and ultra-short laser pulses for activation of the switching process, the areas with two orthogonal Néel vector orientations are achieved on the same thin film. Thus, the first method of a selective local orientation of the Néel vector in a continuous Mn₂Au film is demonstrated. Moreover, in the switched areas the degree of polarization is comparable with that obtained by application of strong magnetic fields. Such an approach can be already utilised for an efficient writing on Mn₂Au thin films, making it

a long-term memory device.

By further analysis of the magnetic imaging data, we concluded that the switching process occurs via the growth of energetically favorable domains. The effect of the applied mechanical strain is to modify the free energy landscape, inducing a gradient of the free energy, resulting in a force acting on a 90° DW. However, the without activation magnetic domain structure remains the same, due to the pinning of the DWs at defects. Simultaneous rapid heating of the film with optical pulses unpins the domain walls, thus, making one type of the domains to collapse.

In addition, an XMCD contrast is obtained for the Mn₂Au thin film. It is tentatively attributed to uncompensated surface ferromagnetism of the material. XMCD contrast allows one to resolve the domains with Néel vector aligned antiparallel, which in combination with XMLD contrast opens new opportunities for the study the structure of AFM domains and domain walls.

Finally, a pilot time-resolved study of Mn₂Au was performed. While pump-induced light polarization rotation does not give a clear answer about the timescales of the magnetic order suppression, other time-resolved experiments are proposed. Specifically, by periodically applying mechanical strain to the sample, synchronised with the laser repetition rate, one can detect the switching process. Such an experiment should give information about the domain wall velocity and the dependence of the switching on the applied strain.

Author contributions

Removed in the electronic version of this thesis due to data protection regulations.

In der elektronischen Version entfernt aufgrund datenschutzrechtlicher Bestimmungen.

Bibliography

- [1] G. E. Moore, “Cramming more components onto integrated circuits, reprinted from electronics, volume 38, number 8, april 19, 1965, pp.114 ff.,” *IEEE Solid-State Circuits Society Newsletter*, vol. 11, pp. 33–35, 2006.
- [2] *International Technology Roadmap for Semiconductors 2.0*. ITRS, 2017.
- [3] I. Zutic, J. Fabian, and S. Das Sarma, “Spintronics: Fundamentals and applications,” *Rev. Mod. Phys.*, vol. 76, pp. 323–410, Apr 2004.
- [4] M. T. Alam, M. J. Siddiq, G. H. Bernstein, M. Niemier, W. Porod, and X. S. Hu, “On-chip clocking for nanomagnet logic devices,” *IEEE Transactions on Nanotechnology*, vol. 9, pp. 348–351, 2010.
- [5] E. V. Gomonay and V. M. Loktev, “Spintronics of antiferromagnetic systems (review article),” *Low Temperature Physics*, vol. 40, no. 1, pp. 17–35, 2014.
- [6] T. Jungwirth, X. Marti, P. Wadley, and J. Wunderlich, “Antiferromagnetic spintronics,” *Nature Nanotech*, vol. 11, pp. 231–241, 2016.
- [7] A. Sapozhnik, M. Filianina, S. Y. Bodnar, A. Lamirand, M.-A. Mawass, Y. Skourski, H.-J. Elmers, H. Zabel, M. Kläui, and M. Jourdan, “Direct imaging of antiferromagnetic domains in Mn₂Au manipulated by high magnetic fields,” *Physical Review B*, vol. 97, no. 13, p. 134429, 2018.
- [8] S. Techert, “Current developments in time-resolved x-ray diffraction,” *Crystallography Reviews*, vol. 12, pp. 25–45, 01 2006.

- [9] M. Eichberger, H. Schäfer, M. Krumova, M. Beyer, J. Demsar, H. Berger, G. Moriena, G. Sciaini, and R. J. D. Miller, “Snapshots of cooperative atomic motions in the optical suppression of charge density waves,” *Nature*, vol. 468, no. 7325, pp. 799–802, 2010.
- [10] C. A. Nelson, J. Luo, A. K. Y. Jen, R. B. Laghumavarapu, D. L. Huffaker, and X. Y. Zhu, “Time-, energy-, and phase-resolved second-harmonic generation at semiconductor interfaces,” *The Journal of Physical Chemistry C*, vol. 118, pp. 27981–27988, 12 2014.
- [11] D. Kutnyakhov, R. P. Xian, M. Dendzik, M. Heber, F. Pressacco, S. Y. Agustsson, L. Wenthaus, H. Meyer, S. Gieschen, G. Mercurio, A. Benz, K. Bühlman, S. Däster, R. Gort, D. Curcio, K. Volckaert, M. Bianchi, C. Sanders, J. A. Miwa, S. Ulstrup, A. Oelsner, C. Tusche, Y. J. Chen, D. Vasilyev, K. Medjanik, G. Brenner, S. Dziarzhyski, H. Redlin, B. Manschwetus, S. Dong, J. Hauer, L. Rettig, F. Diekmann, K. Rossnagel, J. Demsar, H. J. Elmers, P. Hofmann, R. Ernstorfer, G. Schönhense, Y. Acremann, and W. Wurth, “Time- and momentum-resolved photoemission studies using time-of-flight momentum microscopy at a free-electron laser,” *Review of Scientific Instruments*, vol. 91, p. 013109, 2021/09/24 2020.
- [12] J. Coey, *Magnetism and magnetic materials*. Cambridge University Press, 2009.
- [13] P. M. Paul, E. S. Toma, P. Breger, G. Mullot, F. Augé, P. Balcou, H. G. Muller, and P. Agostini, “Observation of a train of attosecond pulses from high harmonic generation,” *Science*, vol. 292, no. 5522, pp. 1689–1692, 2001.
- [14] E. Marín and R. Ivanov, “LIA in a nut shell: How can trigonometry help to understand lock-in amplifier operation?,” *Lat. Am. J. Phys. Educ.*, vol. 3, 2009.
- [15] V. Grigorev, A. R. Pokharel, A. Mejas, T. Dong, A. A. Haghighirad, R. Heid, Y. Yao, M. Merz, M. L. Tacon, and J. Demsar, “Dynamics of collective modes in an unconventional charge density wave system BaNi_2As_2 ,” *arXiv*, p. 2102.09926, 2021.
- [16] J. Stöhr and H. C. Siegmann, *Magnetism: From Fundamentals to Nanoscale Dynamics*. Springer-Verlag Berlin Heidelberg, 2006.

- [17] T. Moriya, “Anisotropic superexchange interaction and weak ferromagnetism,” *Physical Review*, vol. 120, pp. 91–98, 1960.
- [18] I. Dzyaloshinsky, “A thermodynamic theory of "weak" ferromagnetism of antiferromagnetics,” *Journal of Physics and Chemistry of Solids*, vol. 4, pp. 241 – 255, 1958.
- [19] P. Wadley, B. Howells, J. Železný, C. Andrews, V. Hills, R. P. Campion, V. Novák, K. Olejník, F. Maccherozzi, S. S. Dhesi, S. Y. Martin, T. Wagner, J. Wunderlich, F. Freimuth, Y. Mokrousov, J. Kuneš, J. S. Chauhan, M. J. Grzybowski, A. W. Rushforth, K. W. Edmonds, B. L. Gallagher, and T. Jungwirth, “Electrical switching of an antiferromagnet,” *Science*, vol. 351, no. 6273, pp. 587–590, 2016.
- [20] S. Y. Bodnar, L. Šmejkal, I. Turek, T. Jungwirth, O. Gomonay, J. Sinova, A. A. Sapozhnik, H. J. Elmers, M. Kläui, and M. Jourdan, “Writing and reading antiferromagnetic Mn_2Au by Néel spin-orbit torques and large anisotropic magnetoresistance,” *Nat. Commun.*, vol. 9, p. 348, 2018.
- [21] Curie, P., “Sur la symétrie dans les phénomènes physiques, symétrie d’un champ électrique et d’un champ magnétique,” *J. Phys. Theor. Appl.*, vol. 3, no. 1, pp. 393–415, 1894.
- [22] E. Beaurepaire, J.-C. Merle, A. Daunois, and J.-Y. Bigot, “Ultrafast spin dynamics in ferromagnetic nickel,” *Phys. Rev. Lett.*, vol. 76, pp. 4250–4253, May 1996.
- [23] J. Hohlfeld, E. Matthias, R. Knorren, and K. H. Bennemann, “Nonequilibrium magnetization dynamics of nickel,” *Phys. Rev. Lett.*, vol. 78, pp. 4861–4864, Jun 1997.
- [24] A. Scholl, L. Baumgarten, R. Jacquemin, and W. Eberhardt, “Ultrafast spin dynamics of ferromagnetic thin films observed by fs spin-resolved two-photon photoemission,” *Phys. Rev. Lett.*, vol. 79, pp. 5146–5149, Dec 1997.
- [25] J. Gütde, U. Conrad, V. Jähnke, J. Hohlfeld, and E. Matthias, “Magnetization dynamics of Ni and Co films on Cu(001) and of bulk nickel surfaces,” *Phys. Rev. B*, vol. 59, pp. R6608–R6611, Mar 1999.

- [26] B. Koopmans, M. van Kampen, J. T. Kohlhepp, and W. J. M. de Jonge, “Ultrafast magneto-optics in nickel: Magnetism or optics?,” *Phys. Rev. Lett.*, vol. 85, pp. 844–847, Jul 2000.
- [27] T. Ogasawara, K. Ohgushi, Y. Tomioka, K. S. Takahashi, H. Okamoto, M. Kawasaki, and Y. Tokura, “General features of photoinduced spin dynamics in ferromagnetic and ferrimagnetic compounds,” *Phys. Rev. Lett.*, vol. 94, p. 087202, Mar 2005.
- [28] M. van Kampen, C. Jozsa, J. T. Kohlhepp, P. LeClair, L. Lagae, W. J. M. de Jonge, and B. Koopmans, “All-optical probe of coherent spin waves,” *Phys. Rev. Lett.*, vol. 88, p. 227201, May 2002.
- [29] A. Kirilyuk, A. V. Kimel, and T. Rasing, “Ultrafast optical manipulation of magnetic order,” *Rev. Mod. Phys.*, vol. 82, pp. 2731–2784, Sep 2010.
- [30] Y. Fan, X. Ma, F. Fang, J. Zhu, Q. Li, T. P. Ma, Y. Z. Wu, Z. H. Chen, H. B. Zhao, and G. Lüpke, “Photoinduced spin angular momentum transfer into an antiferromagnetic insulator,” *Phys. Rev. B*, vol. 89, p. 094428, Mar 2014.
- [31] A. Kirilyuk, A. Kimel, F. Hansteen, T. Rasing, and R. V. Pisarev, “Ultrafast all-optical control of the magnetization in magnetic dielectrics,” *Low Temperature Physics*, vol. 32, no. 8, pp. 748–767, 2006.
- [32] C. D. Stanciu, F. Hansteen, A. V. Kimel, A. Kirilyuk, A. Tsukamoto, A. Itoh, and T. Rasing, “All-optical magnetic recording with circularly polarized light,” *Phys. Rev. Lett.*, vol. 99, p. 047601, Jul 2007.
- [33] I. Radu, K. Vahaplar, C. Stamm, T. Kachel, N. Pontius, H. A. Dürr, T. A. Ostler, J. Barker, R. F. L. Evans, R. W. Chantrell, A. Tsukamoto, A. Itoh, A. Kirilyuk, T. Rasing, and A. V. Kimel, “Transient ferromagnetic-like state mediating ultrafast reversal of antiferromagnetically coupled spins,” *Nature*, vol. 472, no. 7342, pp. 205–208, 2011.
- [34] R. Hertel, “Microscopic theory of the inverse Faraday effect,” *arXiv*, p. 0509060, 2005.

- [35] T. A. Ostler, J. Barker, R. F. L. Evans, R. W. Chantrell, U. Atxitia, O. Chubykalo-Fesenko, S. El Moussaoui, L. Le Guyader, E. Mengotti, L. J. Heyderman, F. Nolting, A. Tsukamoto, A. Itoh, D. Afanasiev, B. A. Ivanov, A. M. Kalashnikova, K. Vahaplar, J. Mentink, A. Kirilyuk, T. Rasing, and A. V. Kimel, “Ultrafast heating as a sufficient stimulus for magnetization reversal in a ferrimagnet,” *Nature Communications*, vol. 3, no. 1, p. 666, 2012.
- [36] S. Mangin, M. Gottwald, C.-H. Lambert, D. Steil, V. Uhlíř, L. Pang, M. Hehn, S. Abrand, M. Cinchetti, G. Malinowski, Y. Fainman, M. Aeschlimann, and E. E. Fullerton, “Engineered materials for all-optical helicity-dependent magnetic switching,” *Nature Materials*, vol. 13, no. 3, pp. 286–292, 2014.
- [37] C.-H. Lambert, S. Mangin, B. S. D. C. S. Varaprasad, Y. K. Takahashi, M. Hehn, M. Cinchetti, G. Malinowski, K. Hono, Y. Fainman, M. Aeschlimann, and E. E. Fullerton, “All-optical control of ferromagnetic thin films and nanostructures,” *Science*, vol. 345, no. 6202, pp. 1337–1340, 2014.
- [38] K. T. Yamada, A. V. Kimel, K. H. Prabhakara, S. Ruta, T. Li, F. Ando, S. Semin, T. Ono, A. Kirilyuk, and T. Rasing, “Efficient all-optical helicity dependent switching of spins in a Pt/Co/Pt film by a dual-pulse excitation,” *arXiv*, p. 1903.01941, 2021.
- [39] C. Wang and Y. Liu, “Ultrafast optical manipulation of magnetic order in ferromagnetic materials,” *Nano Convergence*, vol. 7, no. 1, p. 35, 2020.
- [40] A. H. MacDonald and M. Tsoi, “Antiferromagnetic metal spintronics,” *Phil. Trans. R. Soc. A.*, vol. 369, pp. 3098–3114, 2011.
- [41] V. Baltz, A. Manchon, M. Tsoi, T. Moriyama, T. Ono, and Y. Tserkovnyak, “Antiferromagnetic spintronics,” *Rev. Mod. Phys.*, vol. 90, p. 015005, Feb 2018.
- [42] C. Tzschaschel, K. Otani, R. Iida, T. Shimura, H. Ueda, S. Günther, M. Fiebig, and T. Satoh, “Ultrafast optical excitation of coherent magnons in antiferromagnetic NiO,” *Phys. Rev. B*, vol. 95, p. 174407, May 2017.

- [43] V. Barthem, C. Colin, H. Mayaffre, M.-H. Julien, and D. Givord, “Revealing the properties of Mn_2Au for antiferromagnetic spintronics,” *Nature Communications*, vol. 4, no. 1, pp. 1–7, 2013.
- [44] S. Y. Bodnar, M. Filianina, S. Bommanaboyena, T. Forrest, F. Maccherozzi, A. Sapozhnik, Y. Skourski, M. Kläui, and M. Jourdan, “Imaging of current induced néel vector switching in antiferromagnetic Mn_2Au ,” *Physical Review B*, vol. 99, no. 14, p. 140409, 2019.
- [45] M. Jourdan, H. Bräuning, A. Sapozhnik, H. Elmers, H. Zabel, and M. Kläui, “Epitaxial Mn_2Au thin films for antiferromagnetic spintronics,” *Journal of Physics D: Applied Physics*, vol. 48, no. 38, p. 385001, 2015.
- [46] S. Bommanaboyena, T. Bergfeldt, R. Heller, M. Kläui, and M. Jourdan, “High quality epitaxial Mn_2Au (001) thin films grown by molecular beam epitaxy,” *Journal of Applied Physics*, vol. 127, no. 24, p. 243901, 2020.
- [47] S. Bodnar, *Manipulation of Néel Vector in Antiferromagnetic Mn_2Au by Electric Current and Magnetic Field Pulses*. PhD thesis, Johannes Gutenberg-Universität Mainz, 2020.
- [48] A. A. Sapozhnik, R. Abrudan, Y. Skourski, M. Jourdan, H. Zabel, M. Kläui, and H.-J. Elmers, “Manipulation of antiferromagnetic domain distribution in Mn_2Au by ultrahigh magnetic fields and by strain,” *physica status solidi (RRL) - Rapid Research Letters*, vol. 11, no. 4, p. 1600438, 2017.
- [49] H.-J. Elmers, S. Chernov, S. D’Souza, S. Bommanaboyena, S. Y. Bodnar, K. Medjanik, S. Babenkov, O. Fedchenko, D. Vasilyev, S. Agustsson, *et al.*, “Néel vector induced manipulation of valence states in the collinear antiferromagnet Mn_2Au ,” *ACS nano*, vol. 14, no. 12, pp. 17554–17564, 2020.
- [50] A. S. Borovik-Romanov, A. A. Kreines, A. A. Pankov, and T. M. A., “Magnetic birefringence of light in antiferromagnetic transition-metal fluorides,” *Sov. Phys.-JETP*, vol. 64,

- pp. 1762–1775, May 1973.
- [51] B. B. Krichevtsov and R. V. Pisarev, “Anisotropy of magnetic linear dichroism in cubic magnetic substances,” *Sov. Phys.-JETP*, vol. 84, pp. 865–877, March 1983.
- [52] V. Grigorev, M. Filianina, S. Y. Bodnar, S. Sobolev, N. Bhattacharjee, S. Bommanaboyena, Y. Lytvynenko, Y. Skourski, D. Fuchs, M. Kläui, M. Jourdan, and J. Demsar, “Optical readout of the Néel vector in the metallic antiferromagnet Mn_2Au ,” *Phys. Rev. Applied*, vol. 16, p. 014037, Jul 2021.
- [53] W. M. Yim and R. J. Paff, “Thermal expansion of AlN, sapphire, and silicon,” *Journal of Applied Physics*, vol. 45, no. 3, pp. 1456–1457, 1974.
- [54] C. Roder, S. Einfeldt, S. Figge, T. Paskova, D. Hommel, P. P. Paskov, B. Monemar, U. Behn, B. A. Haskell, P. T. Fini, and S. Nakamura, “Stress and wafer bending of a-plane GaN layers on r-plane sapphire substrates,” *Journal of Applied Physics*, vol. 100, no. 10, p. 103511, 2006.
- [55] S. Bommanaboyena, D. Backes, L. Veiga, S. Dhesi, Y. Niu, B. Sarpi, T. Denneulin, A. Kovacs, T. Mashoff, O. Gomonay, *et al.*, “Readout of a antiferromagnetic spintronics systems by strong exchange coupling of Mn_2Au and Permalloy,” *arXiv*, p. 2106.02333, 2021.
- [56] L. Nadvorník, M. Borchert, L. Brandt, R. Schlitz, K. A. de Mare, K. Vÿbornÿ, I. Mertig, G. Jakob, M. Kläui, S. T. Goennenwein, *et al.*, “Broadband terahertz probes of anisotropic magnetoresistance disentangle extrinsic and intrinsic contributions,” *Phys. Rev. X*, vol. 11, p. 021030, May 2021.
- [57] G. De Stasio, L. Perfetti, B. Gilbert, O. Fauchoux, M. Capozzi, P. Perfetti, G. Margaritondo, and B. P. Tonner, “MEPHISTO spectromicroscope reaches 20 nm lateral resolution,” *Review of Scientific Instruments*, vol. 70, pp. 1740–1742, 1999.
- [58] R. Moubah, M. Elzo, S. El Moussaoui, D. Colson, N. Jaouen, R. Belkhou, and M. Viret, “Direct imaging of both ferroelectric and antiferromagnetic domains in multiferroic

- bifeo₃ single crystal using x-ray photoemission electron microscopy,” *Applied Physics Letters*, vol. 100, no. 4, p. 042406, 2012.
- [59] J. Wu, D. Carlton, J. S. Park, Y. Meng, E. Arenholz, A. Doran, A. T. Young, A. Scholl, C. Hwang, H. W. Zhao, J. Bokor, and Z. Q. Qiu, “Direct observation of imprinted antiferromagnetic vortex states in coo/fe/ag(001) discs,” *Nature Physics*, vol. 7, no. 4, pp. 303–306, 2011.
- [60] J. Bartolomé, F. Bartolomé, A. I. Figueroa, O. Bunău, I. K. Schuller, T. Gredig, F. Wilhelm, A. Rogalev, P. Krüger, and C. R. Natoli, “Quadrupolar xmc d at the fe *k*-edge in fe phthalocyanine film on au: Insight into the magnetic ground state,” *Phys. Rev. B*, vol. 91, p. 220401, Jun 2015.
- [61] S. P. Chenakin, R. Prada Silvy, and N. Kruse, “Effect of x-rays on the surface chemical state of al₂o₃, v₂o₅, and aluminovanadate oxide,” *The Journal of Physical Chemistry B*, vol. 109, no. 30, pp. 14611–14618, 2005. PMID: 16852843.
- [62] C. Chauvet, F. Polack, M. G. Silly, B. Lagarde, M. Thomasset, S. Kubsky, J. P. Duval, P. Risterucci, B. Pilette, I. Yao, N. Bergéard, and F. Sirotti, “Carbon contamination of soft X-ray beamlines: dramatic anti-reflection coating effects observed in the 1keV photon energy region,” *Journal of Synchrotron Radiation*, vol. 18, pp. 761–764, 2011.
- [63] X. Xu, S. Xu, L. Jin, and E. Song, “Characteristic analysis of otsu threshold and its applications,” *Pattern Recognition Letters*, vol. 32, no. 7, pp. 956–961, 2011.
- [64] H. S. Carslaw and J. C. Jaeger, *Conduction of heat in solids*. Clarendon press, 1992.
- [65] D. Mihailovic and J. Demsar, *Time-Resolved Optical Studies of Quasiparticle Dynamics in High-Temperature Superconductors: Experiments and Theory*, ch. 16, pp. 230–244. American Chemical Society, 1999.
- [66] S. Burghartz and B. Schulz, “Thermophysical properties of sapphire, AlN and MgAl₂O₄ down to 70 K,” *Journal of nuclear materials*, vol. 212, pp. 1065–1068, 1994.

-
- [67] M. Obergfell and J. Demsar, “Tracking the time evolution of the electron distribution function in copper by femtosecond broadband optical spectroscopy,” *Physical review letters*, vol. 124, no. 3, p. 037401, 2020.
- [68] M. Meinert, D. Graulich, and T. Matalla-Wagner, “Electrical switching of antiferromagnetic Mn_2Au and the role of thermal activation,” *Phys. Rev. Applied*, vol. 9, p. 064040, Jun 2018.
- [69] N. I. Zheludev, P. J. Bennett, H. Loh, S. V. Popov, I. R. Shatwell, Y. P. Svirko, V. E. Gusev, V. F. Kamalov, and E. V. Slobodchikov, “Cubic optical nonlinearity of free electrons in bulk gold,” *Opt. Lett.*, vol. 20, pp. 1368–1370, Jun 1995.
- [70] R. Wilks and R. J. Hicken, “Transient optical polarization response of aluminium at an interband transition,” *Journal of Physics: Condensed Matter*, vol. 16, pp. 4607–4617, jun 2004.

List of Figures

1.1	Schematic of an optical pump-probe setup.	9
1.2	Detection scheme of a pump-probe setup.	12
1.3	Timeline of the pump-probe experiment	13
1.4	Transient reflectivity example.	16
1.5	Spin configurations of crystalline magnetic materials.	19
1.6	Spontaneous magnetisation as a function of temperature.	23
1.7	Illustration of the non-equilibrium dynamics of the Fe and Gd magnetisation leading to all-optical switching.	25
1.8	The structure of Mn_2Au showing the spin orientations.	28
2.1	Geometry of the observation of the MO effects.	34
2.2	Three configurations in which the magneto-optical Kerr or Faraday effects. . . .	36
2.3	The layout and the images of samples used in the dichroism experiment.	41
2.4	Schematic of the experimental setup for MLD measurement and the time evolu- tion of the light intensity on the photodiode.	43
2.5	Results of reflectivity anisotropy studies on magnetically ordered Mn_2Au	47
2.6	Schematic of the sample layout in dichroism measurements for the two different orientations of the sample with respect to the laser beam directions.	49
3.1	Sketch of a synchrotron light source.	55

3.2	Sketch of the photoexcitation process leading to the generation of the secondary electrons in PEEM.	56
3.3	Schematic illustration of the mechanism of the XMCD effect.	58
3.4	XMCD- and XMLD-PEEM images of Mn_2Au	61
3.5	X-ray absorption spectrum and the XMCD contrast vs the X-ray energy.	62
3.6	Degradation of the XMCD contrast.	64
3.7	XMLD contrast of the imaged areas and the corresponding processed binary images.	67
3.8	Dependence of the degree of polarization on the excitation fluence and strain.	68
3.9	XMLD contrast variation along the sample irradiated at different strain conditions.	69
3.10	Simulated temporal evolution of temperature	72
3.11	Schematic of the free energy landscape under strain and the light-induced switching in Mn_2Au	73
3.12	Domain wall dynamics following irradiation with optical pulses.	77
4.1	Detection scheme of the pump-induced polarization rotation.	82
4.2	Pump-induced polarization rotation of Mn_2Au	84
4.3	Comparison of the pump-induced polarization rotation and transient reflectivity.	85
4.4	Timeline of the proposed pump-probe experiment based on the periodic application of mechanical strain frequency-locked to the laser.	87
4.5	Eigen-modes of the sapphire substrate.	88
4.6	Prototype electro-mechanical device for the periodic strain generation.	89

Curriculum Vitae

PERSONAL INFORMATION

Name: Vladimir Grigorev

Address: Walpodenstrasse 16, Mainz 55116

Mobile: +49 1762 8919794

Email: vgrigore@uni-mainz.de

Born: February 4, 1992—Saint-Petersburg, USSR

Nationality: Soviet

EDUCATION

09.2016 - now. **PhD candidate** in Physics, Johannes Gutenberg University Mainz, Germany

Title of thesis: *Optical read-out and manipulation of the Néel vector in the metallic collinear antiferromagnet Mn_2Au*

09.2013 - 06.2015. **MSc** in Physics, Peter the Great St.Petersburg Polytechnic University, Russia

Title of thesis: *Quantum magnetism of silicon nanosandwiches*

09.2009 - 06.2013. **BSc** in Physics, Peter the Great St.Petersburg Polytechnic University,
Russia

Title of thesis: *Development of the experimental setup for the detection of singlet oxygen*

09.2005 - 06.2009. **High School**

School: N°207, Saint-Petersburg, Russia

TEACHING

- Tutor, Solid state physics (WiSe 17/18)
- Tutor, Solid state physics (SoSe 18)
- Tutor, Solid state physics (WiSe 19/20)

Publications list

1. **V. Grigorev**, M. Filianina, Y. Lytvynenko, S. Sobolev, A. R. Pokharel, A. Sapozhnik, A. Kleibert, S. Yu. Bodnar, P. Grigorev, M. Kläui, H.-J. Elmers, M. Jourdan, J. Demsar. Manipulation of a Collinear Metallic Antiferromagnet with Femtosecond Optical Pulses and External Strain. *in preparation* (2021).
2. **V. Grigorev**, A. Mejas, A. R. Pokharel, T. Dong, A. A. Haghighirad, R. Heid, Y. Yao, M. Merz, M. L. Tacon, J. Demsar. Collective Modes in BaNi_2As_2 Probed by Time-Resolved Spectroscopy. *arXiv:2102.09926* (2021). (under review).
3. **V. Grigorev**, M. Filianina, S. Yu. Bodnar, S. Sobolev, N. Bhattacharjee, S. Bommanaboyena, Y. Lytvynenko, Yurii Skourski, D. Fuchs, M. Kläui, M. Jourdan, J. Demsar. Optical Readout of the Néel Vector in the Metallic Antiferromagnet Mn_2Au . *Phys. Rev. Applied* **16**, 014037 (2021).
4. D. Dominko, D. Starešinić, K. Biljaković, M. Đekić, A. S. Fetić, K. Hrvat, M. Lozančić, J. Demsar, **V. Grigorev**, T. P. Potočnik, M. Spreitzer. Single Crystal-Like Thin Films of Blue Bronze *Thin Solid Films* **731**, 138745 (2021).
5. N.T. Bagraev, **V. Yu. Grigoryev**, L.E. Klyachkin, A.M. Malyarenko, V.A. Mashkov, V.V. Romanov, N.I. Rul. High-Temperature Quantum Kinetic Effect in Silicon Nanosandwiches. *Low temperature physics* **43**, 110-119 (2017).